Electrical and Material Properties of Strained Silicon/Relaxed Silicon Germanium Heterostructures for Single-Electron Quantum Dot Applications

Chiao-Ti Huang

A Dissertation
Presented to the Faculty
of Princeton University
in Candidacy for the Degree
of Doctor of Philosophy

Recommended for Acceptance
by the Department of
Electrical Engineering
Adviser: Professor James C. Sturm

June 2015

© Copyright by Chiao-Ti Huang, 2015.

All rights reserved.

Abstract

A single-electron quantum dot device is an ideal environment to demonstrate the concept of a spin-based quantum bit, a promising candidate to realize a quantum computer. Two-dimensional electron gases (2DEGs) in silicon/silicon germanium heterostructures have been considered as a potential platform to fabricate single-electron quantum dots for spin manipulations because silicon has an inherently longer spin coherence time. Then two different types of silicon 2DEGs, modulation-doped 2DEG and enhancement-mode undoped 2DEG, are discussed. The efforts to improve both 2DEGs into a better material system for quantum computing application are the main focus of this thesis.

A severe leakage issue of the Schottky gating on a modulation-doped 2DEG is resolved by successful suppression of phosphorus surface segregation. A high breakdown voltage is thus achieved in a Schottky gated modulation-doped 2DEG without significant gate leakage current. Implant isolation as an alternative for lateral electrical isolation in a modulation-doped 2DEG at 4.2 K is also successfully demonstrated. It preserves surface planarization and prevents the leakage issues through the corners of etched mesas. The best implant conditions for effective isolation and better thermal stability are examined and determined. The quality of these doped 2DEGs is verified to be unaffected by the implant isolation process.

The transport property of an enhancement-mode 2DEG is significant for a spin-based quantum bit. Various mobility-limiting factors in our undoped 2DEGs grown by RTCVD are identified. Efforts to alleviate these scattering mechanisms lead to mobility as high as 400,000 cm^2/Vs and the critical density as low as 3.2×10^{10} cm^{-2} at 4.2 K. A tunable screening effect on remote charges at silicon/oxide interface is found to greatly improve the transport properties of thin-cap enhancement-mode 2DEGs, which compensates the detrimental influences from the remote charges at the interface, and thus remains the capability for a sharp electron patterning from

the top gates. In addition, theoretical and experimental work on the effect of the regrowth interface in undoped 2DEGs is demonstrated as well.

Acknowledgements

This has been really a long journey. Luckily, I have finally reached the destination of my doctoral life. I wouldn′t be able to make it without assistances from many people. First, I would like to thank Princeton University and Department of Electrical Engineering for providing such an exciting opportunity and comfortable environment for me to pursue my Ph.D. degree. I always remember how excited I was when I received admission with full financial support from Princeton University, just as the world was slammed by the financial crisis in 2009. When I was an undergraduate, I aimed to do my doctoral research in the U.S. and live here with my wife, Chi-Hua. Thanks to Princeton University, I had a chance to achieve my dream.

My adviser, Professor James C. Sturm, is undoubtedly the first person I would like to say thank you to. I am deeply indebted to Prof. Sturm for his stimulating insights and inspiring advises that have guided me through the long journey of my Ph.D.. His perpetual enthusiasm and unwavering supports have always enlightened me, especially when I felt perplexed and lost direction in the past six years. I would also like to thank Professor Barry Rand and Professor Stephen Chou for their precious advice and opinions on my thesis. Furthermore, I would like to thank Professor Jason Petta, Professor Mansour Shayegan and Prof. Stephen Lyon for their guidance in the field of low-dimensional physics in semiconductors and novel quantum computing. A special thanks goes to Professor Daniel Tsui for his continuous support and warm encouragement on my doctoral research.

This work could not be completed without assistance from our collaborators. I would like to express my gratitude to Professor Leonid P. Rokhinson and his students at Purdue University for their helps on low-temperature measurements, Dr. Wei Pan and Dr. Tzu-Ming Lu at Sandia National Laboratories for their useful advice on my experimental results. I also would like to thank HRL Laboratories and researchers there for their support on our wafer growth, and Amberwave Systems Inc. for provid-

ing us high quality relaxed SiGe buffer substrates. Here at Princeton, I am obliged to Professor Mansour Shayegan and his student Hao Deng for their prompt helps on magneto-resistance measurements, and Professor Jason Petta and his student Ke Wang and post-doc Dr. Christopher M. Payette for their stimulating discussions on spin-based quantum dot devices.

I am also thankful to all the members I′ve met in Sturm group. I am so excited to be one of the certificated RTCVD heroes with Keith Chung, Sushobhan Avasthi and Jiun-Yun Li. In particular, I am grateful to Jiun-Yun for his guidance on both research and life. Without his help, it would have been a very painful process for me to get my life started in the U.S.. I also want to say thank you to Sturm group members more senior than me: Bahman Hekmatshoar, Yifei Huang, Kevin Loutherback, Noah Jafferis and Ting Liu for their assistance and advice, and to Sturm group members junior than me: Ken Nagamatsu, Warren Rieutort-Louis, Josue Sanz-Robinson, Janam Jhaveri, Yasmin Afsar, Yu Chen, Alexander Berg, and Levent Aygun for their warm company. In particular, a special thanks must go to Janam Jhaveri for his time on proofreading my thesis. Finally, I would like to say thank you to the group members in my year: Bhadri Visweswaran, Amy Wu and Joseph DSilva. I will never forget the happiness and sadness we have shared since we stepped into the Princeton campus together six years ago. Hey Bhadri! Thank you so much for your support on the CVD maintenance since Jiun-Yun left. I really appreciate it!

I am obliged to all PRISM staff for their unwavering support. I would like to thank Dr. George Watson (Pat), Dr. Mikhail Gaevski, Dr. Conrad Silvestre, Dr. Yong Sun, Dr. Sen Liu, Bert Harrop and Joe Palmer for providing us such a good cleanroom to finish our graduate work. I would also like to thank Dr. Nan Yao and Gerald Poirier for their assistances on material characterizations at IAC. In addition, I am grateful to Sheila Gunning, Kim Hegelbach and Carolyn Arnesen for their helps on plenty of complicated administrative processes.

Taiwanese friends from Princeton Association of Taiwanese Students (PATS) gave us a big warm welcome when we first stepped into the U.S.. A big thanks goes to Yen-Ting Chiu, Kung-Ching Liao, Ya-Chin Chiou, Sophia Liao, Wen-Yi Wu, Yu-Wei Chen, Hao-Ting Wu, Carole-Jean Wu, Yu-Yuan Chen, Brandon Chen, Yue-Kai Huang, Vicky Cheng, Amelia Huang, Kaleb Huang, Ting-Jung Lin, Yin Wang, Tzu-Ming Lu, Jun-Wei Chuah, Michelle Wong, Christine Chuah, Jiun-Yun Li, Amy Dai, Irene Li, Leah Li, Chia-Chun Lin, Yao-Chao Tu, Yu-Cheng Tsai, Huai-An Chin, Jen-Tang Lu and Yao-Wen Yeh. Your warm company made our Princeton life joyful and colorful. The memories with you guys at Princeton are always invaluable gifts for us. A special thanks must go to Huai-An Chin for his supports on the RTCVD maintenance in the last two years.

Finally, I would like to express my deepest gratitude to my family. Since I was a child, my parents always supported every decision I made without any complaints. Their perpetual love and care undoubtedly gave me great courage to overcome so much hard time in the past six years. Without your spiritually and financially assistance, I wouldn′t have been able to finish my Ph.D.. In addition, I would also like to thank my sister and brother-in-law for taking care of our parents when I was at a foreign place 8,000 miles away from home for so long. I am also obliged to my 2-year-old daughter, Bera. The happiness and surprises she brought to us made me understand that this world is indeed so colorful and meaningful. (Of course, her naughtiness also forced her parents to learn their limit of how little sleep they could endure.) Last but not least, I would like to attribute all my success and accomplishments to my beloved, Chi-Hua. She always gave me the warmest hug when I was in difficult times. I am the luckiest man in the world, to have her love.

To my beloved wife, Chi-Hua

Contents

Abstract . . . iii

Acknowledgements . . . v

List of Figures . . . xv

1 Introduction 1

1.1 Motivation . . . 1

1.2 Thesis Outline . . . 3

2 Two Dimensional Electron Gases in Si/SiGe Heterostructures 7

2.1 Introduction . . . 7

2.1.1 Introduction to a 2DEG . . . 7

2.1.2 Introduction to the RTCVD at Princeton University . . . 9

2.2 Characteristics of Silicon 2DEGs . . . 13

2.2.1 Strain-Induced Band Offset in Si/SiGe Heterostructures . . . 13

2.2.2 SiGe Virtual Substrate . . . 15

2.2.3 Types of Strained Silicon 2DEGs . . . 16

2.3 Modulation-Doped Strained Silicon 2DEG . . . 16

2.3.1 Introduction . . . 16

2.3.2 Layer Structure and Epitaxial Growth of a Doped 2DEG . . . 17

2.3.3 A Quantum Device on a Doped 2DEG . . . 19

2.4 Enhancement-Mode Undoped Strained Silicon 2DEG . . . 21

2.4.1 Introduction 21
2.4.2 Layer Structure and Epitaxial Growth of an Undoped 2DEG . 22
2.4.3 A Quantum Device on an Undoped 2DEG 23

3 High Breakdown Voltage Schottky Gating of Doped Silicon 2DEGs 25

3.1 Introduction 25
3.2 Suppression of Phosphorus Surface Segregation 26
3.3 Device Fabrication 27
3.4 Gate Leakage Test at 4.2 K 28
3.5 Depletion of Doped 2DEGs 29
3.6 Quantum Point Contact Test 30
3.7 Summary 34

4 Implant Isolation of Silicon 2DEGs at 4.2 K 36

4.1 Introduction 36
4.2 Sample Growth and Test Device Fabrication 37
4.3 Implant Conditions 39
4.4 Ultra High Sheet Resistance at 4.2 K 41
4.5 Thermal Stability 41
4.6 2DEG Quality Check 44
4.7 Summary 44

5 Enhancement-Mode Undoped Silicon 2DEGs 46

5.1 Motivation 46
5.2 Models for Mobility Limitation 47
5.2.1 Scattering from Background Charged Impurities 48
5.2.2 Scattering from Remote Charged Impurities 49
5.2.3 Scattering from Si/SiGe Interface Roughness 51
5.2.4 Other Possible Scattering Mechanisms 52

5.3 Measurement of Enhancement-Mode Undoped Silicon 2DEGs 53
5.3.1 Device Fabrication and Measurement Setup 53
5.3.2 Parallel Capacitor Plate Model 55
5.4 Transport Property of Undoped Silicon 2DEGs 57
5.4.1 A Brief View of Various Scattering Mechanisms in Our 2DEGs 57
5.4.2 Metal-Insulator Transition and 2D Critical Density 59
5.4.3 Experimental Observation of Metal-Insulator Transition 60
5.4.4 Failure of the MIT Model 62
5.5 Background Scattering Alleviation 64
5.5.1 High Background Impurity Level in Old Samples 64
5.5.2 Efforts to Alleviate Background Scattering 64
5.6 Effects of Remote Scattering 67
5.6.1 Effects of SiGe Cap Thickness 67
5.6.2 Treatments on Oxide/Semiconductor Interface 70
5.6.3 Remote Scattering from the Regrowth Interface 73
5.7 Effects of Growth Temperature 74
5.7.1 Effects of Growth Temperature 74
5.7.2 Surface Roughness versus Interface Roughness 75
5.7.3 Effects of Si/SiGe Interface Roughness 78
5.7.4 Effects of Si/SiGe Interlayer Mixing 79
5.8 Effects of Threading Dislocations 80
5.8.1 Defect Etching 81
5.8.2 Effects of Threading Dislocations on Transport Properties . . 82
5.8.3 Effects of Hall Bar Size 86
5.9 Summary 88

6 Tunable Screening Effect in Undoped 2DEGs 90

6.1 Introduction 90

6.1.1 Motivation 90
6.1.2 Device Fabrication 91
6.2 Four-Stage Behavior of 2D Electron Density 92
6.2.1 Observation of a Density Collapse 92
6.2.2 Non-Equilibrium in Stage II 94
6.2.3 Switching from Stage II to Stage III 95
6.2.4 Support by a Simulation 98
6.3 Tunable Screening Effect in Thin-Cap 2DEGs 99
6.3.1 Improved Transport Property 99
6.3.2 Effect of Surface Electron Density 100
6.3.3 Parallel Conduction in Stage IV 101
6.3.4 Magneto-Resistance Transport Property at 0.3 K 103
6.3.5 Negligible Screening Effect in Thick-Cap 2DEGs 106
6.4 Reverse V_G Scanning in Stage III 108
6.5 Summary 111

7 The Role of the Regrowth Interface on Undoped 2DEG Properties 113

7.1 Introduction 113
7.2 Fermi Level Pinning 114
7.2.1 Contamination at the Regrowth Interface 114
7.2.2 Fermi Level Pinning 115
7.2.3 Comparison of Simulations and Experimental Data 117
7.3 Effects of Regrowth Interface on 2DEG Properties: Thickness of SiGe Buffer 120
7.4 Effects of Baking Power at the Regrowth Interface 123
7.5 Summary 125

8 Conclusions **127**

8.1 Conclusions 127

8.2 Future Work 130

8.2.1 Unknown Mobility-Limiting Factors 130

8.2.2 Isotopically-Enriched Undoped 2DEGs for a Longer Spin Coherence Time 131

A Publications and Presentations **133**

A.1 Journal Articles and Conference Papers 133

A.2 Conference Presentations 134

B Fabrication of Undoped Silicon 2DEGs **136**

B.1 Growth of Undoped Silicon 2DEGs 136

B.1.1 Baking Before Growth on Si and SiGe Substrates 136

B.1.2 Wet Cleaning for Growth Substrates 137

B.1.3 Baking and Carrier Wafer Coating 138

B.1.4 100-mm Carrier Wafer for SiGe Buffer Pieces 138

B.1.5 Standard Layer Structure of an Undoped 2DEG and Its Growth Recipe 139

B.1.6 A Typical SIMS for a High-Mobility Undoped 2DEG 140

B.2 Processes for Enhancement-Mode Undoped 2DEGs 141

B.2.1 Full Processes 141

B.2.2 ALD Chamber Cleaning and Deposition Recipes 142

C Non-Standard Wafer Growth **144**

C.1 Growth on a Thin SiGe Buffer (400 μm) 144

C.1.1 Option 1: 125-mm Carrier Wafer 145

C.1.2 Option 2: 100-mm Carrier Wafer 147

C.1.3 Option 3: 75-mm Quartz Wafer Stand 153

C.2 Growth on a Thick SiGe Buffer (680 μm) 154
C.2.1 Dicing an 150-mm SiGe Buffer into a 100-mm Wafer 154
C.2.2 Growth Temperature Calibration for a Thick SiGe Buffer . . . 154
C.2.3 Growth Uniformity and Mobility Results 156

Bibliography **159**

List of Figures

2.1 The schematic of rapid thermal chemical vapor deposition (RTCVD) at Princeton University. (Image courtesy of P. V. Schwartz) 10

2.2 Original published data of normalized transmission versus temperature for 1.3-μm and 1.55-μm lasers for lightly doped n-type (513 μm) and p-type (493 μm) silicon wafers. 11

2.3 The data of average lamp power versus temperature calibrated by normalized transmission of two infrared lasers with the extrapolation for temperatures >750 ^{o}C. In addition, the lamp powers dropped 6% after a new SCR unit was installed. The common reactor baking power and SiGe buffer baking power used before and after the SCR replacement are both labeled. 12

2.4 (a) The valley splitting in strained silicon results in a quantum well at the strained Si layer between two relaxed SiGe layers. (b) Electrons tend to accumulate in out-of-plane valleys due to their lower energies. 14

2.5 (a) A layer structure and (b) a band diagram of a modulation-doped strained silicon 2DEG. Some of electrons from the intentionally doped layer accumulate in the strained silicon quantum well and form a 2DEG. 18

2.6 (a) A layer structure of a modulation-doped 2DEG with Schottky splitting gates. A 2DEG can be patterned by the Schottky gates with negative biases. (b) A three dimensional view for a typical quantum dot device fabricated on a modulation-doped 2DEG. 20
2.7 (a) A layer structure and (b) a band diagram of a typical enhancement-mode undoped strained silicon 2DEG. Electrons are capacitively induced in the strained silicon channel by the metal gate with positive biases. (The metal gate is not shown here, and the oxide is partially shown for brevity) 23
2.8 (a) The layer structure of an enhancement-mode undoped 2DEG with depletion gates inserted between an oxide and a surface silicon cap. Electrons in the strained silicon channel can be patterned by these depletion gates. (b) A three dimensional view of a quantum dot device fabricated on an enhancement-mode 2DEG. 24

3.1 The schematic of atomic layer structures near the surface during the epitaxial growth for a doped 2DEG. (Image courtesy of Jiun-Yun Li) 27
3.2 A SIMS profile for the sample with a cap layer grown at 575 °C. The phosphorus bump in the Si 2DEG is a SIMS artifact. 28
3.3 The phosphorus segregation can be greatly suppressed by lowering cap layer growth temperature from 575 °C to 525 °C. The phosphorus surface concentration is reduced as low as 2×10^{16} cm^{-3}. The P peak at surface is a typical artifact resulted from the surface effect in a SIMS measurement. 29
3.4 Schottky gate leakage test at 4.2 K. The inset shows the cross section of a test device. 30

3.5 Depletion test at 4.2 K of the sample with a cap layer grown at 525 °C. Both drain and gate leakage currents are shown in log scale in the inset. 31
3.6 Successful QPC test at 4.2 K without any leakage. A wide transient region is observed. The inset shows the schematic of the QPC test structure. 32
3.7 A SEM image of a typical QPC test device. 33
3.8 The channel between G_0 and G_1 remains on at -2 V but the channel between G_0 and G_5 can be fully shut off. 34

4.1 The layer structure of a test sample. The layers above the horizontal dotted line were grown by RTCVD. To pattern the 2DEG, only one of implant isolation or conventional mesa isolation by RIE is used on a single sample, but both are illustrated in this figure for brevity. . . . 38
4.2 (a) The schematic of a test device (not to scale). It consists of 1 Hall bar structure, 1 set of connected contacts and 1 set of isolated contacts. The cross session of the set of isolated alloy contacts indicated by the white dot line is shown in (b). 39
4.3 Simulation of implanted species and resulting vacancy distribution in a 2DEG structure by the Stopping and Range of Ions in Matters (SRIM) software. Two-step implantation (1×10^{14} cm^{-2} @ 30 keV+1×10^{14} cm^{-2} @ 60 keV) with implanted species (a) Ar^+ and (b) Si^+ is used in this simulation. The target is assumed to be implanted at 0 K. 40

4.4 Isochronal (1 hour) annealing behavior of sheet resistances of 2DEG samples at 4.2 K implanted with (a) Ar^+ and (b) Si^+ with three various doses, 5×10^{11} cm^{-2}, 1×10^{13} cm^{-2} and 1×10^{14} cm^{-2} at 30 keV and 60 keV. Also shown are the range of sheet resistance of the starting 2DEGs, and the experimental instrumental limitation. The estimated error of sheet resistance is ±18% for (a) and 27% for (b). 42

4.5 Comparison of 2DEG quality after implant isolation or RIE process by the ratio of the mobility at 4.2 K measured from an implant-isolation-defined Hall bar to a RIE-defined Hall bar for a given implant and anneal. The absolute mobility values at 4.2 K with a unit of 10^3 cm^2/Vs are shown in parentheses with the mobility for implant isolation before the mobility for mesa isolation. The estimated error of mobility measurement is ±5%. 45

5.1 The schematic of background charged impurities in an undoped silicon 2DEG. 49

5.2 The schematic of remote charged impurities at the oxide/silicon interface in an undoped silicon 2DEG. 51

5.3 The schematic of Si/SiGe interface roughness in an undoped silicon 2DEG. 52

5.4 The layer structure of a typical undoped enhancement-mode strained silicon 2DEG. 54

5.5 The top view of a standard Hall bar geometry used in this study. The magenta regions are Cr/Au metal stacks deposited in the same evaporation. The Cr/Au metal contacts are deposited directly on the silicon surface (etched holes of the aluminum oxide). 55

5.6 A typical linear V_G dependence of 2D electron density in an undoped enhancement-mode silicon 2DEG. The inset shows the channel turn-on with increasing gate voltages. 56
5.7 A schematic of two equivalent capacitors in series between metal gate and a conducting 2DEG in strained silicon channel. 57
5.8 Typical Hall measurement data measured from 2DEGs grown in our RTCVD with theoretical fitting curves of three main possible mobility-limiting mechanisms. 58
5.9 The schematic of potential fluctuation caused by remote charges at the silicon/oxide interface in an undoped 2DEG. 60
5.10 (a) A 2DEG conducts as a metal in the channel when the electron density is high (b) A 2DEG acts as an insulator because electrons are localized in the valleys of fluctuations when the electron density is too low. 61
5.11 The modified mobility model by a MIT model (green curve) fit the data of the sample with a 27-nm SiGe cap, especially in the low density regime. 62
5.12 A discrepancy between data points of the sample with a 55-nm SiGe cap and the modified model by the MIT model. The modified mobility model is the green line, while the original model is in black. 63
5.13 The SIMS profile of a typical undoped 2DEG grown in our RTCVD before a new gas supply system was introduced. Clear high concentrations of both phosphorus and boron were observed. 65
5.14 The schematic of the new gas supply panel and the gas supply assembly. Phosphine is separately transported from other process gases until a half meter away from the reactor entry to avoid mixture and contamination. 66

5.15 Extremely low concentrations of both phosphorus and boron in grown layers after a new gas panel and a gas supply assembly were installed. Both doping levels hit the detection limits of the high-precision SIMS analysis. 67
5.16 Mobility curves from samples with various SiGe cap thicknesses. Mobility is enhanced with a thicker SiGe cap, but saturate at 400,000 cm^2/Vs. 69
5.17 The highest mobility and lowest 2D electron density extracted from samples with various SiGe cap layers. The critical density gets lower in the sample with thicker SiGe cap thickness due to weaker potential fluctuations. 70
5.18 Mobility curves measured from samples with an aluminum oxide deposited at three different temperatures: 150 °C, 225 °C and 300 °C . 72
5.19 Mobility curves from samples annealed at different temperatures (450 °C, 600 °C and 750 °C) after ALO deposition. 73
5.20 The shifts in threshold voltages imply that charges are trapped at the interface after annealing. 74
5.21 Mobility curves from samples whose strained silicon layers were grown at different temperatures. 76
5.22 An AFM image and its calculated RMS roughness on a complete undoped silicon 2DEG. 77
5.23 An AFM image and its calculated RMS roughness from a reference sample whose layer structure only consists of the relaxed SiGe buffer and the strained silicon QW (channel). 77
5.24 Mobility curves labeled by individual growth temperature and its RMS surface roughness. 79

5.25 Extracted highest mobility and lowest 2D density versus surface roughness. 80
5.26 Images acquired by Normaski Microscopy after samples were dipped into modified Schimmel solutions.(a) Plenty of dot-like threading dislocations are distributed all over the sample whose $T_{Si,Cap}$ and $T_{Si,QW}$ were 575 °C and 700 °C respectively.(b) Much fewer etch pits are seen in the sample whose silicon layers were both grown at 625 °C. 83
5.27 The EPD measured from images by Normaski microscopy versus silicon growth temperature. 84
5.28 The highest mobility and lowest 2D density versus etch pit density from five different samples. 85
5.29 The geometries of (a) a standard Hall bar with a 300-μm spacing between R_{xx} probes (denoted as a 300-μm Hall bar) and (b) a small Hall bar with a 10-μm spacing between R_{xx} probes (denoted as a 10-μm Hall bar). 87
5.30 The comparison between mobility measured from a standard Hall bar and two small Hall bars fabricated in the sample from the same growth run. 88

6.1 The four-stage behavior in Hall electron density observed in all three samples (Data here are from the sample with a 14-nm SiGe cap layer). The dashed line shows the theoretical maximum n_{2D} from the self-consistent Schrodinger-Poisson (SCSP) simulation. 93
6.2 (a)With a small gate bias, electrons accumulate in the buried QW first. (b) Even with a large gate bias, no electrons populate the surface QW due to a high critical density for metal-insulator transition (MIT) in that layer. 95

6.3 The comparison of buried electron density (n_{buried}, red) and surface electron density ($n_{surface}$, blue) with increasing gate voltages in both thermal equilibrium with the contacts between two 2DEGs and with the surface channel not in equilibrium. A sudden collapse in n_{buried} as the gate voltage increases and the corresponding increase in $n_{surface}$ bring the system back to thermal equilibrium. 96

6.4 (a) no electrons are induced in the surface due to a high critical density of MIT for the surface QW. (b) At a higher gate voltage, electron tunneling from the buried QW towards the surface raises the density above the metal insulator transition point, leading to a current flowing from the contacts into the surface layer (c). (d) By Gauss′s law, the buried electron density must be reduced as the surface density increases at a fixed gate voltage. The system is then switched from non-equilibrium to thermal equilibrium. 97

6.5 Electrons exist at both the surface and the buried QW, with the same Fermi level in both layers. Now the system is in thermal equilibrium. 98

6.6 The dependence of Hall mobility on Hall electron density measured at 4.2 K for all three samples with different stages labeled. The gate voltage steps for data points at stage II and stage III/IV are 0.03-0.15 V / 0.1-2 V, respectively for all three samples. The measurement sequence is indicated by dashed lines (from stage II to stage III). . . . 100

6.7 (a) The reduction in minimum n_{2D} due to the screening effect by the surface electron layer. (b) The increasing surface electron density screens the scattering from remote charges and thus enhances the buried electron mobility. 101

6.8 Surface electron mobility (calculated based on the parallel conduction model) versus the surface electron density (calculated in Sec. 6.3.2). The right Y axis shows the conductance ratio of the surface QW to the buried QW. 102
6.9 The four-stage behavior in density of the sample with a 20-nm SiGe cap measured by Hall measurement at 4.2 K (red). The sample was then dipped to 0.3 K for magneto-resistance transport measurement. Two representative gate biases used at 0.3 K were highlighted in blue. 104
6.10 The magneto-resistance transport measurements at 0.3 K were shown versus magnetic field up to 15 T at (a) 4 V (stage II) and (b) 9 V (stage III). 105
6.11 (a) R_{xx} versus the inverse of magnetic field from the sample with a 20-nm SiGe cap at 9 V in the range of 0.5 T to 2.5 T. (b) The Fourier transform of the curve in (a) shows three peaks. The ratio of frequencies show the different degeneracies, but they all represent the same conducting channel and a single electron density of 2.92×10^{11} cm^{-2}. . 106
6.12 An identical four-stage behavior in density was also observed in samples with thicker SiGe caps (90 nm in this case). 107
6.13 Mobility data of the 2DEG sample with a thick SiGe cap (90 nm). No significant screening effect was observed. 108

6.14 The modulation of electron density under two scanning directions of gate voltages. Electrons are first accumulated in the QW as the gate voltages ramp up at stage II (solid symbols, step 1) until a collapse occurs. The density then drops to a fixed value with further increasing biases (open symbols, step 2). Finally, the density remains constant as the gate voltages ramp down, followed by a linear decrease when the gate voltage crosses the boundary of two stages (open symbols, step 3). (This reference sample has a 75-nm SiGe cap layer and a 145-nm SiGe buffer) 110

6.15 The transport property of a typical undoped 2DEG with a thick SiGe cap under a regular voltage ramp-up at stage II (solid symbols) and a voltage ramp-down at stage III (open symbols). 111

7.1 A typical SIMS of an undoped 2DEG shows very high densities of oxygen and carbon at the regrowth interface. The integral 2D densities of oxygen and carbon are 6×10^{13} cm^{-2} and 4×10^{14} cm^{-2}, respectively. A typical baking power for SiGe relaxed buffers is 20% for 5 minutes, which is roughly equal to 850 °C. 115

7.2 Band diagrams of an undoped 2DEG under a 0.2 V bias with the Fermi level pinned at four different positions: 0.045 eV below E_C (green), 0.25 eV below E_C (purple), mid-gap (brown) and 0.045 eV above E_V (orange).116

7.3 The theoretical maximum n_{2D} in equilibrium (with different biases) by the simulation with different pinning conditions. The inset shows the layer structure used in the simulation. (The band gap of $Si_{0.72}Ge_{0.28}$ is set as 1.04 eV) 117

7.4 The experimental maximum n_{2D} at stage III, from samples whose buffer layers are between 150 nm and 190 nm, versus corresponding SiGe cap thickness. Simulations with a fixed buffer thickness (190 nm) and various E_F pining conditions are shown in green (E_C-E_F =0.045 eV), purple (E_C-E_F=0.25 eV) and brown (E_F at midgap) solid lines and an orange dash line (E_F-E_V =0.045 eV). 118

7.5 The experimental maximum of n_{2D} at stage III from samples whose SiGe cap layers are between 20 nm and 180 nm versus corresponding SiGe buffer layer thickness. The simulations were done with a fixed buffer thickness (190 nm). The simulation curve with the pinning position (E_C-E_F =0.045 eV) in green fits the data best. 119

7.6 Transport properties of samples with various SiGe buffer layer thicknesses. Solid and open symbols represent data measured in stage II (scan up) and stage III (scan down), respectively. 121

7.7 Highest mobility and critical densities (the lowest n_{2D}) at both stage II (scan up) and stage III (scan down, as shown in Fig. 6.14) extracted from samples with various thicknesses of SiGe buffer layers. The blue solid and blue open symbols are the lowest n_{2D} at stage II and stage III, respectively. 122

7.8 Mobility curves from samples with various baking powers. Solid and open symbols represent data measured in stage II (scan up) and stage III (scan down), respectively. 124

7.9 Highest mobility and critical densities at both stage II (scan up) and stage III (scan down) extracted from samples with various baking powers. The lowest n_{2D} at stage II and stage III are blue solid and blue open symbols, respectively. 125

B.1 A typical SIMS measured on dirty epi-layers grown on a silicon substrate. 137

B.2 (a) The top view and (b) the cross section along the red line of a standard 100-mm carrier wafer. 139
B.3 A typical SIMS of an undoped 2DEG with group record high mobility. 140
B.4 A mask image that describes the four photolithography steps for enhancement-mode undoped 2DEG fabrication. 142

C.1 The picture of a 125-mm carrier held by a 125-mm quartz wafer stand with a 75-mm wafer on it. 145
C.2 The picture of 75-mm SiGe buffer carried by a 125-mm carrier wafer after a test growth. The color rings labeled by yellow lines represent the thickness nonuniformity. 146
C.3 The schematic of a 75-mm SiGe buffer and a silicon temperature control piece held by a 125-mm carrier wafer. The pieces sent out for SIMSs are highlighted. 147
C.4 The thickness comparison between pieces cut from different locations on the 75-mm SiGe buffer held by a 125-mm carrier wafer. 147
C.5 The schematic of a 75-mm wafer on a 100-mm carrier wafer. The 75-mm is used to calibrate growth temperatures. 148
C.6 The normalized transmission of two infrared lasers calculated based on Eq. C.1 for different wafer thicknesses. 149
C.7 The SIMS analyses for two separate pieces cut from a 75-mm SiGe buffer carried by a 100-mm carrier wafer. The peaks in the silicon channel could be artifacts. 150
C.8 The thickness non-uniformity of epitaxial layers grown on a 75-mm SiGe buffer carried by a 100-mm carrier wafer. 151
C.9 The mobility data measured at 4.2 K from center pieces and pieces near the edge. The center piece shows a group record high mobility. . 152

C.10 The thickness percentages of epi-layers grown on a 75-mm silicon substrate carried by a 100-mm carrier wafer. 153
C.11 The picture of a diced 100-mm SiGe buffer from a 150-mm SiGe wafer. The ring along the edge of the diced wafer is the etched pattern from the quartz ring of Samco 800 etcher, showing the quartz ring perfectly covered the edge of the diced wafer during the etching. 155
C.12 The pieces cut for SIMS analyses from a diced 100-mm SiGe buffer after a standard undoped 2DEG growth. 156
C.13 The SIMS analyses for the pieces with different distances from the wafer center of a diced 100-mm SiGe buffer. 157
C.14 The thickness non-uniformity of epi-layers grown on a diced 100-mm SiGe buffer. 157
C.15 The mobility measured from pieces with different distances from the wafer center of a diced 100-mm SiGe buffer. The highest mobility at 4.2 K is 200,000 cm^2/Vs. 158

Chapter 1

Introduction

1.1 Motivation

Since the concept of a transistor was first demonstrated in 1947 by John Bardeen, Walter Brattain and William Shockley [1], and the first commercial silicon-based transistor was presented in 1954 by Texas Instruments [2], silicon has dominated our life for over a half century. The electronic products made from silicon are ubiquitous, from advanced medical instruments to consumer electronics, and from private data storage centers to public communication systems. More and more advanced applications such as smart phones and the internet of things (IOT) that either have or will have huge impacts on our current life style are all enabled by a small silicon chip that consists of billions of silicon transistors. Over the past four decades, semiconductor industries have followed the famous Moore′s law which describes that the number of transistors in an integrated circuit (IC) chip doubles approximately every two years. The denser transistors in an IC chip leads to higher computation performance and lower power consumption. Today, an Intel 15-core Xeon IvyBridge-EX central processing unit (CPU) possesses over 4.3 billion transistors [3]. The scaling of the size of a single transistor has been the rule of thumb in silicon industry to allow more tran-

sistors to be packed into a small IC chip. For example, the semiconductor technology node has progressed from the scale of 100 μm in the early 1970s to today′s 14 nm, which translates to a near 10,000 times reduction in a transistor dimension and 10^8 in area.

Unfortunately, a notorious short channel effect plagues scaled transistors. The gate of a transistor loses its effective control of the channel switching as a transistor shrinks in size. A novel device, the fin field-effect transistor (FinFET), with metal gates covering three sides of a protruding channel currently predominates most state-of-the-art semiconductor microprocessors because of its superior gate control capability [4]. Nevertheless, the soaring capital investment in both research and development (R&D) along with exponentially increased technical difficulties for next-generation technology such as the 10-nm node or the 7-nm node may foresee the end of scaling of the conventional silicon transistor.

Many alternatives have been proposed in past decades as a potential candidate for next-generation computation. Among them, the concept of quantum computing drew many scientists′ attention when it was first proposed in the early 1980s. Peter Shor at AT&T Bell Laboratories then developed the first quantum algorithm in 1994 and set a guideline for future research towards the realization of quantum computation [5]. Quantum computing itself provides us a promising way to implement fundamental computation at a near atomic level. More importantly, it exploits the advantages of quantum superposition and quantum entanglement between two basic states, enabling a novel concept of quantum bit (Qubit) that can store much more information than a conventional bit, like a metal-oxide-semiconductor field-effect-transistor (MOSFET). Possible methods to implement quantum computing include superconducting devices [6], linear optics [7], and charge-based semiconductor quantum dots (QD) [8]. In the late 1990s, Daniel Loss and David DiVincenzo proposed to utilize the intrinsic spin of an electron in a semiconductor quantum dot as a basic

unit for novel logic computation [9]. The abundant knowledge about electron spin in semiconductors and high compatibility with the facilities in today′s silicon industries greatly increase feasibility of spin-based quantum computation. This novel spin-based quantum bit in a semiconductor motivated all the work done in this thesis.

There is still a long way for quantum computing technology to become mature. The low operation temperature could also limit its future applications for commercial products. Notwithstanding these issues, the theoretically-predicted computation speed that quantum computing may have to offer will keep exciting researchers throughout the world. We can expect that the uncountable efforts scientists put in the quantum computing field will not stop until our lives are deeply and unconsciously influenced by it someday in the future.

1.2 Thesis Outline

This thesis starts with a brief introduction to the two-dimensional electron gas (2DEG) realized in Si/SiGe heterostructures in Ch. 2. The benefits of the Si-based material system for single-electron quantum dot devices as a spin-based quantum bit are elaborated. Band engineering by means of strain and relaxation in Si/SiGe layers is introduced as well as the growth of such Si/SiGe heterostructures in our RTCVD system. The advantages and disadvantages of modulation-doped and enhancement-mode undoped strained silicon 2DEGs in terms of compatibility for quantum dot applications are respectively proposed. The focus is then shifted to improving drawbacks of both 2DEGs, making a silicon 2DEG a better platform for quantum computing applications.

Phosphorus surface segregation from the intentional doping layer in a modulation-doped 2DEG causes an undesirably high phosphorus concentration in cap layers. Its resultant detrimental gate leakage current and low breakdown voltage always leave a

question mark on the possibility of a modulation-doped 2DEG as a candidate for a single-electron quantum dot device. In Ch. 3, we identify the phosphorus segregation mechanism in relaxed SiGe layers during epitaxial growth. A lower growth temperature is experimentally proven to effectively preserve the hydrogen coverage on a surface layer to be grown and thus block the surface segregation paths of phosphorus atoms in a sub-surface layer. A two order of magnitude reduction in surface phosphorus concentration enables a successful depletion test of Schottky splitting gates on top of a modulation-doped 2DEG without any significant gate leakage. A quantum point contact device as a charge sensor is then fabricated to choose the best distance between a sensor and a dot, which paves the road towards a quantum dot device.

The conventional etching isolation on a modulation-doped 2DEG has been proved as an effective way to isolate a mesa with size of around 30 μm^2, on to which small Schottky splitting gates could be deposited. However, the corner-induced gate leakage and conformability issue of either thin oxide layers or metal gates to cover step edges limit its usefulness. Reliable lateral electrical isolation which preserves surface planarization can be achieved by ion implantation (Ch. 4). The low operation temperature (4.2 K or below) and the low thermal budget of a quantum dot device fabrication make implant isolation feasible in silicon-based materials. Appropriate implant recipes are chosen for an effective isolation that is resistant to post-implant annealing up to 550 °C in both the doping layer and strained silicon channel. The 2DEG qualities in terms of electron mobility of implanted samples are assured to remain as good as those of intact samples.

In Ch. 5, we discuss the importance of electron mobility and critical electron density in an enhancement-mode undoped 2DEG. Both are viewed as essential parameters that show the cleanliness of a 2DEG system and its adequacy for a delicate quantum dot device. Efforts toward a high electron mobility or low critical density have been initiated with a careful identification of possible scattering mechanisms

in our 2DEG system. Efforts to alleviate these mobility-limiting factors, such as a decisive modification of the gas panel of our CVD system to reduce background phosphorus concentration, have led to mobility enhancement and critical density reduction. The significances of growth temperature and the layer thickness of a Si/SiGe heterostructure in the transport properties are specifically emphasized here with a detailed systematic investigation.

An inevitable compromise between sharp electron confinement from top depletion gates versus high mobility and low density comes from the SiGe cap thickness. The transport properties of a 2DEG could get severely deteriorated if the distance between the electron channel and oxide/silicon interface gets shortened in order to sharpen electrical potentials from gates for 2DEG patterning. In Ch. 6, a screening effect on remote scattering sites at the interface enabled by a newly-formed surface electron layer is unveiled in a series of enhancement-mode undoped strained silicon 2DEGs. The introduction of a surface electron layer with ultra low mobility is initiated by a tunneling of electrons from the channel towards the interface, followed by a positive feedback process that pulls the 2DEG system from non-equilibrium back to thermal equilibrium. The surface electrons act as a shield to screen out the detrimental interface charges, leading to a great improvement in transport properties of enhancement-mode undoped 2DEGs especially with thin SiGe caps.

In Ch. 7, the importance of the regrowth interface (bottom interface) of undoped silicon 2DEGs is discussed. High carbon and oxygen concentrations at this interface could lead to the pinning of the Fermi level. The most likely pinning position of the Fermi level is identified to be near the conduction band minimum, by means of the comparison of simulation results and experimental data. With varying the SiGe buffer thickness (vary the distance between the regrowth interface and the silicon channel) and the baking power for the regrowth surface (vary the quality of the regrowth

interface), the effect of the regrowth interface on transport properties of undoped 2DEGs is examined as well.

Finally, several future work relevant to this work are discussed in Ch. 8 after a brief conclusion for this thesis.

Chapter 2

Two Dimensional Electron Gases in Si/SiGe Heterostructures

2.1 Introduction

2.1.1 Introduction to a 2DEG

A two-dimensional electron gas (2DEG) in a semiconductor material system, as its name suggests, describes an ultra-thin electron layer existing in a semiconductor with energy confinement in one dimension. Because of its unique low-dimensional nature, a 2DEG system enables many avenues for fundamental research in semiconductor physics. The most common 2DEG in semiconductor technology is the surface electron layer in an n-type metal-oxide-semiconductor field effect transistor (MOSFET) under the strong inversion condition. A high positive voltage expels most of majority carriers (holes) away from the oxide/silicon interface and bends the conduction band (E_c) down to populate electrons to form a 2DEG at the surface. On the other hand, a 2DEG located in a quantum well (QW) that could be realized in semiconductor heterostructures, such as AlGaAs and GaAs or strained Si/SiGe, is verified to have much better transport properties because such a 2DEG is separated away from the

oxide/silicon interface or GaAs surfaces which are full of charged sites. Many different types of transistors have been explored in the past decades based on high-mobility 2DEGs in semiconductor heterostructures. For instance, a modulation-doped field effect transistor (MODFET) was fabricated on Si/SiGe heterostructures [10], while high electron mobility transistor (HEMT) was realized in III-V materials [11].

A decade ago, the superior transport properties of 2DEGs in semiconductor heterostructures drew physicists′ attentions as a potential platform to implement the quantum bit concept. Researchers in the quantum computing field intend to confine a single electron in a semiconductor quantum dot. The spin direction of such a single electron could represent information, and due to the superposition and entanglement of the electron spins, this spin-based quantum bit (or qubit) can store much more information than a conventional bit. Since a 2DEG in semiconductor material systems has already confined electrons in the out-of-plane direction, methods to isolate a 2DEG laterally, such as etching isolation or Schottky top gates, enable us to fabricate a quantum dot and possibly confine a single electron in it for the following spin manipulation.

The research on a spin-based qubit in a semiconductor quantum dot was first initiated in III-V 2DEGs. The higher mobility due to its low electron mass and the defect-free films due to lattice-matched heterostructures in GaAs/AlGaAs are attractive for isolating electrons with fewer scattering sources. However, the inherently strong interaction between electrons and nuclei, also known as hyperfine coupling, in this material system is detrimental to the spin coherence time (or dephasing time, T_2^*) [12, 13]. For example, a very short dephasing time $T_2^* \sim 7$ ns in III-V materials was observed [14]. Recently, a 2DEG in the Si/SiGe heterostructure became the most popular material system to fabricate a spin-based quantum dot, as the naturally abundant isotopic ^{28}Si has zero hyperfine coupling. A much longer dephasing time (for instance, ~360 ns in [15]) is thus allowed in the Si-based material system,

facilitating the spin manipulation process. Therefore, in this thesis, we mainly focus on the silicon-based 2DEG system for quantum computing applications. Research on two different types of silicon 2DEGs (modulation-doped 2DEGs and enhancement-mode 2DEGs) are both discussed. In contrast to the spin physics, we emphasize the epitaxial growth and characterization of Si/SiGe heterostructures. Also, we investigate the 2DEG transport properties under various process treatments, and analyze how transport properties can be improved and optimized to fit the requirement for spin-based qubit applications.

2.1.2 Introduction to the RTCVD at Princeton University

All Si/SiGe heterostructures used in this thesis were grown using the rapid thermal chemical vapor deposition (RTCVD) system at Princeton University. As its name suggests, this CVD system possesses the capability to vary temperature between 500 °C to 1000 °C within seconds. The growth reactor RTCVD is a 150-mm quartz tube surrounded by a reflection assembly, and heated by 12 parallel 6-kW tungsten lamps underneath it (Fig. 2.1). A 100-mm wafer is carried by a quartz wafer holder and transferred into the reactor through a load-lock chamber, which is separated from the main growth chamber by a gate valve to avoid contamination from air during the loading process. Available process gases carried by ultra pure hydrogen (99.9999%) in our system include silicon precursors: silane (SiH_4), disilane (Si_2H_8), dichlorosilane (DCS); germanium precursor germane (GeH_4); n-type and p-type dopant precursors: phosphine (PH_3) and diborane (B_2H_6). Their flow rates are controlled by metal-sealed mass flow controllers (MFCs). Each gas is individually guided by an injection valve to either the reactor for epitaxy or to a waste line where a burn box operated at 850 °C burns out excess gases.

The temperature of the wafer in the reactor is controlled by a feedback system. Two infrared lasers with 1.3-μm and 1.55-μm separately modulated by function gen-

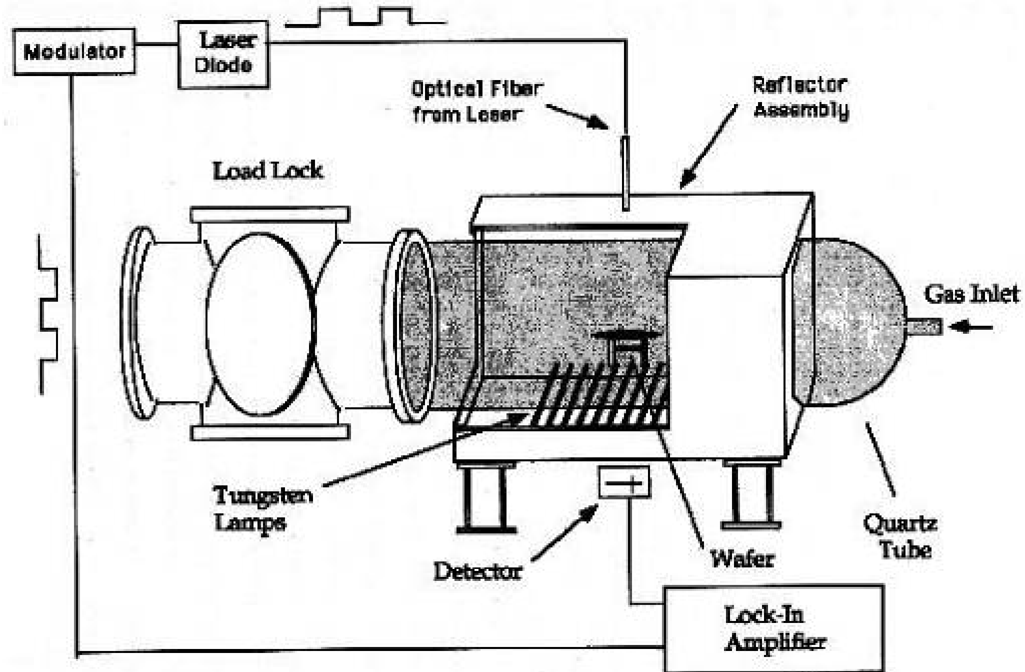

Figure 2.1: The schematic of rapid thermal chemical vapor deposition (RTCVD) at Princeton University. (Image courtesy of P. V. Schwartz [16])

erators, emit from a fiber on the top of the reactor towards the wafer in it. The transmission through the wafer of the 1.3-μm and 1.55-μm lasers, measured by a photodetector and a lock-in amplifier, are very sensitive to a specific range of temperature: 500 °C-625 °C and 675 °C-750 °C, respectively. The ratio of transmission at a target temperature to that at room temperature is called normalized transmission, and depends on the absorption coefficient and the wafer thickness. The absorption of these two infrared lasers in silicon consists of two different processes: band to band absorption and free carrier absorption [17, 18, 19]. For a lightly-doped silicon substrate, it was found that the dominant mechanism for 1.3-μm photons is band to band absorption, which gets stronger with an increasing temperature due to bandgap narrowing. In contrast, 1.55-μm photons are mainly absorbed by free carrier absorption, which is enhanced by a higher temperature due to the increasing free carrier

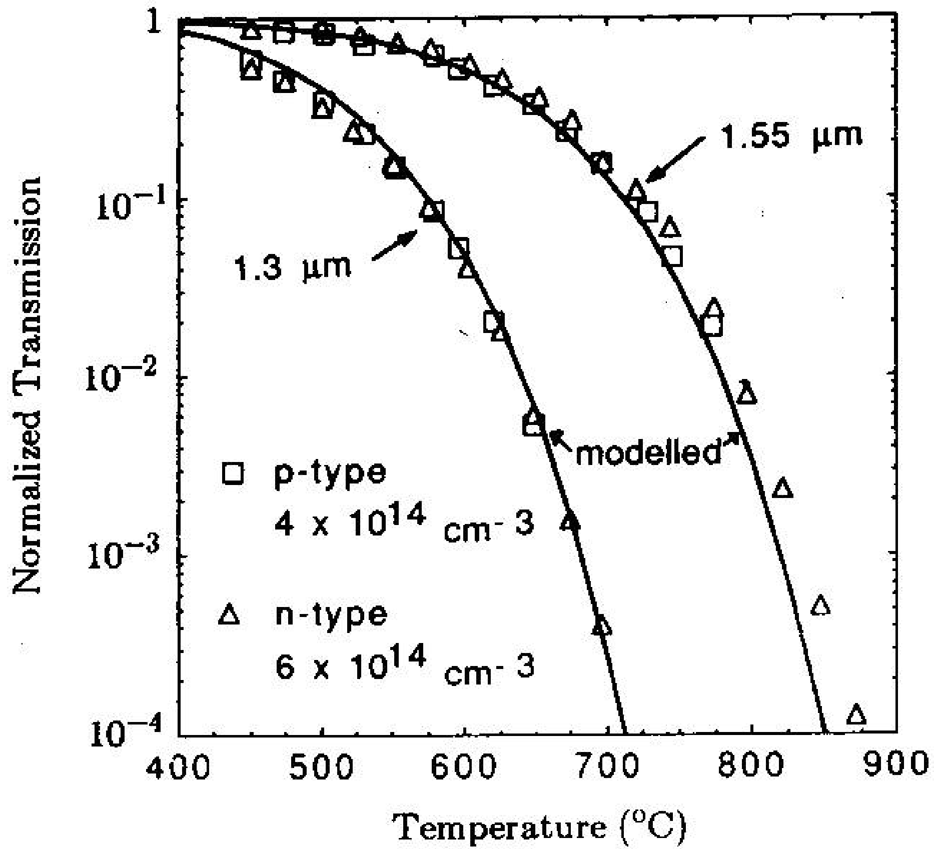

Figure 2.2: [17] Original published data of normalized transmission versus temperature for 1.3-μm and 1.55-μm lasers for lightly doped n-type (513 μm) and p-type (493 μm) silicon wafers.

concentrations. The normalized transmission data published in [17] are shown in Fig. 2.2.

A control PC calculates an instantaneous normalized transmission and feeds it back to the lamp power, to keep this normalized transmission equal to that corresponding to the target temperature. The controllable temperature range (500 °C-750 °C) is right the range we commonly use for Si or SiGe epitaxy. Beyond this range, a constant lamp power is used to replace the precise temperature reading for higher temperature baking (>750 °C), and an estimated temperature for any baking power could be roughly extracted based on those regular growth temperatures. The data

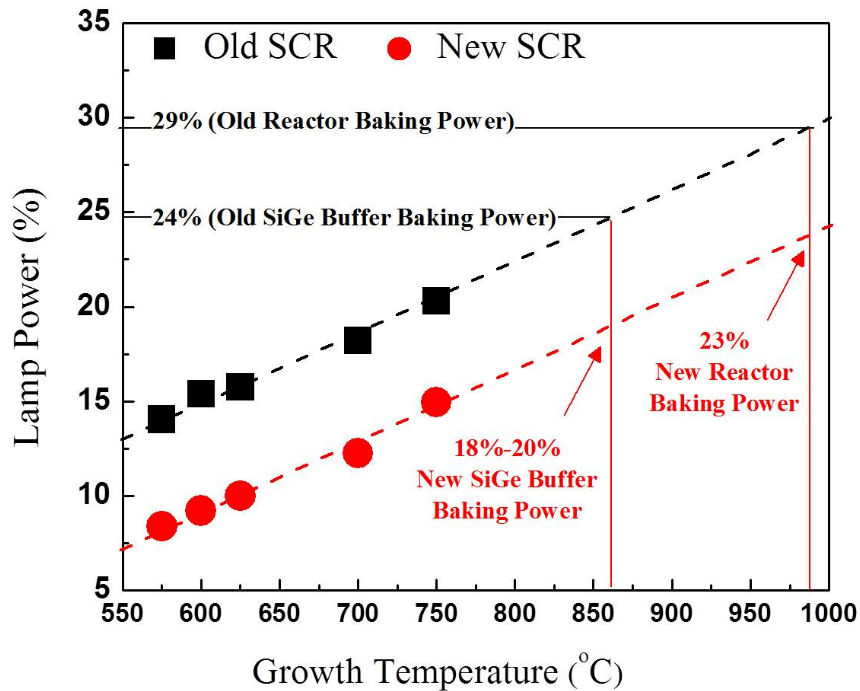

Figure 2.3: The data of average lamp power versus temperature calibrated by normalized transmission of two infrared lasers with the extrapolation for temperatures >750 °C. In addition, the lamp powers dropped 6% after a new SCR unit was installed. The common reactor baking power and SiGe buffer baking power used before and after the SCR replacement are both labeled.

of average experimental lamp powers versus corresponding temperatures calibrated by two infrared lasers are shown in Fig. 2.3 with the extrapolations for temperatures higher than 750 °C. Note that the replacement of the silicon control rectifier (SCR) power controller of RTCVD on December 2013 resulted in a 6% drop in lamp powers for all measurable temperatures.

2.2 Characteristics of Silicon 2DEGs

2.2.1 Strain-Induced Band Offset in Si/SiGe Heterostructures

To prevent scattering from the oxide/silicon interfaces or bare sample surfaces, a 2DEG buried underneath the sample surface is preferable for the manipulation of electron spin. A quantum well for electrons in a Si/SiGe heterostructure is attractive to hold a 2DEG because we can easily bury this 2D electron layer as deep as we want to alleviate the influence from the sample surfaces. It has been well-known that the strains in either silicon or SiGe layer shift the energy position of the conduction band minimum or the valence band maximum, and lead to the splitting of valley degeneracy [20]. For example, a biaxial compressively strained SiGe layer between relaxed Si layers gives us a band offset in the valence band, resulting in a quantum well in strained SiGe layer for holes, while the band offset at the conduction band minimum is so small that no electrons are confined in the SiGe layer. In this type of Si/SiGe heterostructure, holes created by absorption of a laser accumulate in the quantum well and recombine with electrons moving in the conduction band. The ratio of non-radiative and radiative recombination (photoluminescence, PL) strongly depends on the impurity concentration (carbon or oxygen) and defects in epi-layers. Thus the PL measurement in such Si/SiGe heterostructures has been used as a qualitative measure for the quality of epitaxial films [21].

A conduction band (E_c) offset can be achieved when a silicon layer is biaxial tensile strained on a relaxed SiGe layer (Fig. 2.4a) [22]. This biaxial tensile strain shifts the average energy level of the conduction band minima in silicon, and also splits its 6 fold degeneracy into two groups: Four in-plane valleys (Δ_4) are lifted up, while two out-of-plane valleys (Δ_2) are lowered. A quantum well for electrons thus forms in a strained silicon layer that is sandwiched between two relaxed SiGe layers despite Si

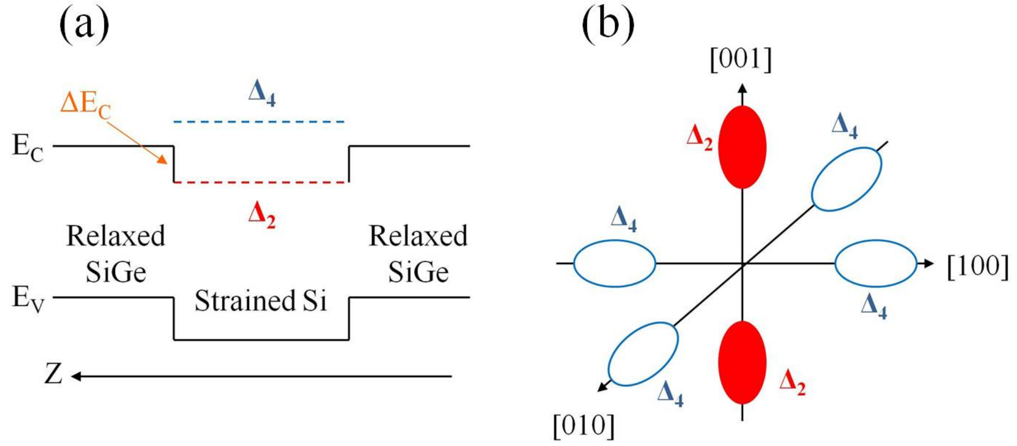

Figure 2.4: (a) The valley splitting in strained silicon results in a quantum well at the strained Si layer between two relaxed SiGe layers. (b) Electrons tend to accumulate in out-of-plane valleys due to their lower energies.

normally having a larger bandgap than SiGe. The Ge fraction in relaxed SiGe layer determines the strength of the strain in the silicon layer, and thus affects the energy separation between Δ_4 and Δ_2. Therefore, the conduction band offset between a relaxed SiGe layer (regular six-fold degenerate E_c) and a tensile strained silicon layer (lowered Δ_2) could be estimated based on the equation: [20]

$$\Delta E_c = E_g(\mathrm{sSi}) + \Delta E_v - E_g(\mathrm{SiGe}) = -0.35y - 0.35y^2 + 0.12y^3 \tag{2.1}$$

where E_g is the band gap of the two materials, while y is Ge fraction of the relaxed SiGe layers. Since electrons tend to accumulate in Δ_2 because of its lower energy level, the effective in-plane electron mass is thus reduced from 0.26 m_0 down to 0.19 m_0, equal to the transverse effective mass of a relaxed silicon layer with 6-fold E_c degeneracy (Fig. 2.4b). This lower electron mass together with the mitigated inter-valley scattering due to the valley splitting both enhance the mobility for electrons in the strained silicon QW.

2.2.2 SiGe Virtual Substrate

It is always a challenging issue to have a high quality relaxed SiGe substrate to introduce tensile strain in pseudomorphic silicon films. A SiGe layer could be relaxed if it is intentionally grown on top of a silicon substrate with considerable thickness due to severe lattice mismatch. However, a high density of threading dislocations may nucleate and distribute all over the SiGe film to relieve the strain caused by lattice mismatch, greatly degrading SiGe film quality. To improve the quality of a relaxed SiGe layer, the concept of graded SiGe buffer was introduced by Currie et. al. in 1998 [23]. On top of a regular silicon substrate, a fairly thick (few microns) SiGe layer is epitaxially grown with a gradual increase in Ge fraction. A typical ramping rate for Ge fraction is 10%/μm. The graded SiGe buffer introduces the lattice mismatch in a slow manner, thus preventing detrimental accumulation of threading dislocation defects. In addition, these initial threading dislocations at the Si/SiGe interface help relieve the strain from 0% Ge to a target fraction. Further nucleation for more threading dislocation defects to relieve strain thus becomes unnecessary. Subsequently, another thick SiGe layer (on the order of a micron) with constant Ge fraction (which is the target Ge fraction) is grown to cap the graded SiGe buffer layer. This buffer layer with constant Ge fraction effectively buries existing threading dislocations in the graded layer, and also blocks their possible propagation towards the surface, leading to an extremely low threading dislocation density at the final SiGe surface.

This kind of high quality SiGe substrate consisting of a bottom silicon substrate, a graded SiGe buffer and a relaxed SiGe buffer with a constant Ge fraction is the so-called SiGe virtual substrate. In this study, all Si/SiGe heterostructures were grown on commercial SiGe virtual substrates from Amberwave Inc. In more detail, the virtual substrate used in this study comprises a p-type (100) silicon substrate, a ~3-μm SiGe graded buffer up to 28% Ge, and a ~1-μm relaxed SiGe buffer with 28%

Ge. To remove the inevitable cross-hatch patterns, a signature shown on the surface of a typical relaxed SiGe buffer caused by the accumulation of dislocation defects, a chemical mechanical planarization (CMP) service was done by Axus Technology. A layer thinner than 500 nm was then removed, and the surface RMS roughness was improved from 7.4 nm down to 0.2 nm.

2.2.3 Types of Strained Silicon 2DEGs

Thanks to the quantum well for electrons in strained Si/SiGe heterostructures, electrons can be confined as a two-dimensional electron gas (2DEG). More importantly, this 2DEG is buried away from the surface of the heterostructure by a relaxed SiGe cap layer with an adjustable thickness. Based on the way that electrons are supplied into the quantum well, two types of silicon 2DEGs are discussed: modulation-doped 2DEGs (electrons are supplied from a n^+ doping layer) and enhancement-mode 2DEGs (electrons are induced by a gate). Details for both types of 2DEGs are presented in Sec. 2.3 and Sec. 2.4 respectively.

2.3 Modulation-Doped Strained Silicon 2DEG

2.3.1 Introduction

The modulation-doped 2DEG was first realized in III-V material systems [24]. To exploit high mobility in GaAs system [25], a modulation-doped GaAs/AlGaAs 2DEG is gated to form a high-electron-mobility transistor (HEMT). The electrons in the channel are supplied by an intentionally doped layer few nanometers away from the GaAs channel. By tuning the distance between the channel and the doping layer (or as we call it, a spacer), an electron density in this modulation-doped structure is determined. The top gate then acts as a switch to either deplete electrons to shut off the channel or leave electrons there to keep the channel on.

Since the discovery of the conduction band offset in strained Si/SiGe material system, a layer of phosphorus-doped SiGe was introduced in the relaxed SiGe cap to mimic the modulation-doped 2DEG structure in III-V system. In the early 1990s, scientists invested much effort to investigate modulation-doped strained silicon 2DEG [26, 27, 28]. Exploratory research was focused on n-type modulation-doped strained silicon 2DEGs because of its potential to make a modulation-doped field effect transistor (MODFET), which has higher electron mobility than a regular bulk MOSFET. In addition, higher electron density could be obtained by optimizing the doping concentration and the spacer thickness, providing another knob that can tune up the drive current in a transistor. As a result, intensive research in the mid-1990s enhanced the low-temperature (<4 K) electron mobility in modulation-doped strained silicon 2DEG from 19,000 cm^2/Vs up to 500,000 cm^2/Vs [29, 30]. Even though the MODFET lost its significance eventually in the late 1990s because of the costly SiGe substrate and the inevitable defects in relaxed SiGe layers, that research has established a solid knowledge foundation for its new application as a platform to implement quantum computing and spin manipulation in the early 2000s.

In this thesis, work related to modulaton-doped strained silicon 2DEG is elaborated in Ch. 3 and Ch. 4. Details about its layer structure and the concept of a single-electron quantum dot device will be introduced in the next two sub-sections.

2.3.2 Layer Structure and Epitaxial Growth of a Doped 2DEG

A typical layer structure of a modulation-doped strained silicon 2DEG is illustrated in Fig. 2.5a. All 2DEG samples used in this thesis were grown by our RTCVD on top of commercial SiGe virtual substrates with Ge fraction ~ 28%. Layer structures of 2DEGs used in this thesis may vary for different purposes, but a standard layer structure and growth recipe will be addressed here for reference. Carried by a 3 lpm

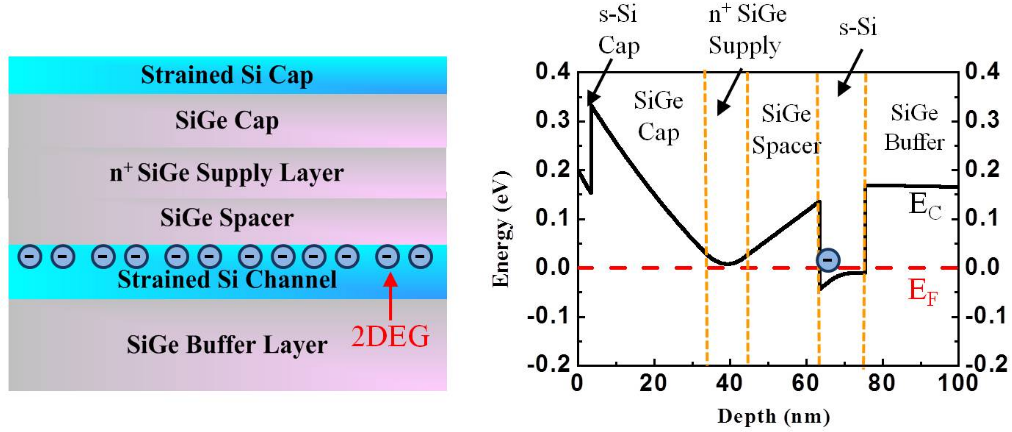

Figure 2.5: (a) A layer structure and (b) a band diagram of a modulation-doped strained silicon 2DEG. Some of electrons from the intentionally doped layer accumulate in the strained silicon quantum well and form a 2DEG.

ultra-clean hydrogen flow, silane (10% in argon) and germane (0.8% in hydrogen) were injected together into the growth reactor for SiGe epitaxial growth or silane was injected alone for Si epitaxial growth. The flow rates of precursors could be tuned to grow SiGe layers with various Ge fractions. Standard Si and SiGe growth temperatures were 625 °C and 575 °C, respectively, at a fixed pressure ~ 6 torr. Doped layers were realized by injecting phosphine (100 ppm in hydrogen) along with silane and germane.

A relaxed $Si_{0.72}Ge_{0.28}$ buffer layer (~150 nm) was first grown on top of a virtual substrate. The purpose of this buffer layer is to separate the next strained silicon layer as an active electron channel away from the regrowth interface, which may have detrimental defects. A 10-12 nm strained silicon layer was then grown, with a thickness thinner than the critical thickness to keep this layer fully strained [31]. Next, a thin SiGe spacer with various thicknesses (10-30 nm) was grown to separate the channel from the following doping layer. A 10-nm phosphorus-doped SiGe layer was introduced with high phosphorus concentration ($>10^{18}$ cm^{-3}) as an electron supply layer. Subsequently, a 20-40 nm relaxed SiGe cap layer was grown without intentional

doping, in which the phosphorus concentration is able to ramp down to avoid high phosphorus concentration at the surface that may potentially cause severe leakage in Schottky gates. Finally, a thin strained silicon layer (~3-4 nm) was grown to cap the SiGe surface.

The band diagram of a modulation-doped 2DEG is shown in Fig. 2.5b. The theoretical electron density allowed in a given modulation-doped 2DEG structure could be calculated based on electrostatics [32]. In practice, an electron density is tuned experimentally by the SiGe spacer thickness and phosphorus doping concentration. For example, a lower electron density could be achieved with a thicker SiGe spacer and a lighter phosphorus doping.

2.3.3 A Quantum Device on a Doped 2DEG

Modulation-doped 2DEGs were the first candidate for QD fabrication in Si/SiGe material system. Several approaches to make a quantum dot device on modulation-doped 2DEG have been demonstrated in the past two decades. Klein et. al. isolated a quantum dot device by etching other conducting paths away [33]. The etching depth must be deeper than the depth where the strained silicon channel is buried for an effective lateral isolation. However, the drawback from the etching is obvious: The defects on the etched sidewalls may deplete the electrons in the channel, especially in such fine features on the order of tens of nanometers, and block the electrical conduction. In addition, an extremely well-controlled anisotropic etching process is necessary for etching-defined QD devices. Any significant undercuts could lead to the severe damage of such devices.

Another alternative, the Schottky split-gate technique, has been widely adopted by several groups to make QD devices instead [34, 35]. Different from etching isolation, the splitting Schottky gates electrically isolates a 2DEG. A series of delicate metal gates are directly deposited on a modulation-doped 2DEG. With proper nega-

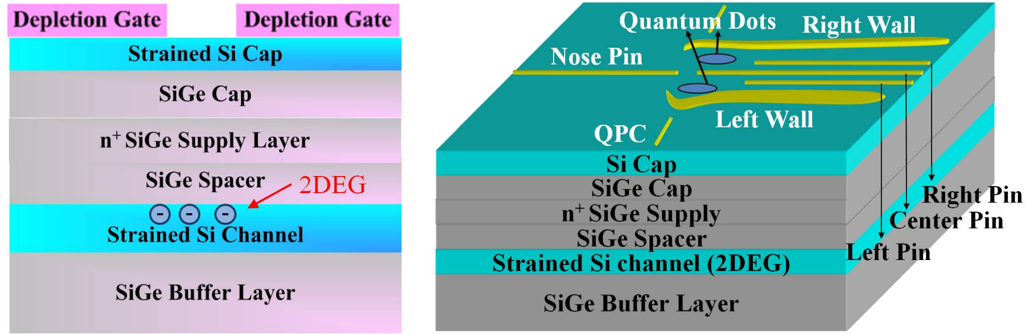

Figure 2.6: (a) A layer structure of a modulation-doped 2DEG with Schottky splitting gates. A 2DEG can be patterned by the Schottky gates with negative biases. (b) A three dimensional view for a typical quantum dot device fabricated on a modulation-doped 2DEG. (This is the model of a real device in [36, 37])

tive biases, electrical fields from these gates deplete electrons in the strained silicon channel, and pattern them into a QD device (Fig. 2.6a). Due to the simplicity of this process, more functional gates are allowed as either tunneling barrier controls or charge sensors (Fig. 2.6b). These Schottky gates on n-type Si/SiGe heterostructures are usually made with high workfunction metals, such as palladium (Pd) or platinum (Pt) to maximize the Schottky barrier and reduce gate leakage. However, in practice, Schottky gated QD devices may suffer from a high gate leakage. This gate leakage may result from the high phosphorus concentration at the surface due to phosphorus surface segregation or other non-idealities. A high surface electrical field caused by a high phosphorus level leads to tunneling through the Schottky barrier from the metal gate to the semiconductor. The work about suppression of phosphorus surface segregation will be discussed in Ch. 3, and a large improvement in breakdown voltage of such Schottky gating on a modulation-doped 2DEG will also be demonstrated.

2.4 Enhancement-Mode Undoped Strained Silicon 2DEG

2.4.1 Introduction

Although most researchers′ efforts have been put on modulation-doped 2DEGs in early development of single-electron quantum devices, people started to realize the potential drawbacks of modulation-doped 2DEGs. First, the gate leakage problem degrades the depletion capability and stability of Schottky split gates. Second, it is very challenging to tune the electron density at a relatively low level (~10^{11} cm^{-2}), which is desirable to deplete a 2DEG into a single electron. Finally, it was found that ionized phosphorus in the doping layer can cause serious potential fluctuations to the electrons in the strained silicon channel. The interference from ionized charges could degrade electron mobility and its spin coherence time.

An enhancement-mode 2DEG was first demonstrated in III-V material system [38]. Then, it was copied to the strained Si/SiGe material system very soon [39]. Since the Si/SiGe heterostructure here is nominally undoped, a gate stack is deposited on top of it to capacitively induce electrons into the strained silicon channel, making it resemble a MOSFET. The benefit of an enhancement-mode undoped 2DEG is clear: the absence of ionized charges could transform this 2DEG into a cleaner system for spin manipulation. In addition, the capability to tune electron density at a low level by simple bias adjustment provides another freedom for layer structure and QD device design.

2.4.2 Layer Structure and Epitaxial Growth of an Undoped 2DEG

Fig. 2.7a shows a layer structure of an enhancement-mode undoped strained silicon 2DEG, which is very similar to that of modulation-doped 2DEGs except for the absence of the intentional doping layer. In our experiments, four Si/SiGe layers were all grown on a commercial SiGe virtual substrate. A 150-nm SiGe layer was first grown, followed by a ~10-nm strained silicon channel. A relaxed SiGe cap layer was then grown on the channel with various thicknesses. The varied SiGe thicknesses represent different distances between the electrons in the strained silicon channel and ionized charged impurities at the oxide/silicon interface, which allows us to observe the effect from interface charges on 2DEG quality, especially the electron mobility and 2D density. Last, the whole heterostructure was capped by a thin strained silicon cap with ~3-4 nm thickness. The gas precursors, growth temperatures, growth flow rates and growth pressures for standard enhancement-mode undoped strained silicon 2DEGs are all the same as those of modulation-doped 2DEG described in Sec. 2.3.2. A ~90-nm aluminum oxide was then deposited on an as-grown undoped 2DEG by atomic layer deposition (ALD) as an insulator. A Cr/Au stack was finally thermally evaporated onto the insulator as a gate for electron induction.

With a sufficient positive voltage on the metal gate, the quantum well in the strained silicon channel is lowered below the Fermi level (E_F). Electrons from the lateral ohmic contacts flow into the strained silicon QW and form a 2DEG (Fig. 2.7b). The SiGe cap layer separates the 2DEG away from the scattering of interface charges, potentially enabling high electron mobility. Here we note that, ideally, the thickness of strained silicon surface cap should always be kept very thin to avoid its ground state from touching the Fermi level earlier than that of strained silicon channel, because any 2DEG induced in the surface QW has a poor quality due to its proximity to interface charges, similar to the 2DEG in a bulk silicon MOSFET.

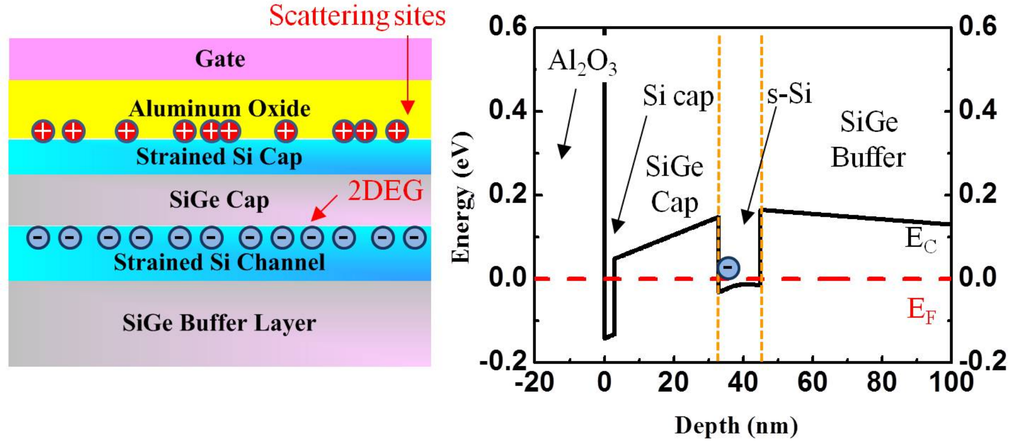

Figure 2.7: (a) A layer structure and (b) a band diagram of a typical enhancement-mode undoped strained silicon 2DEG. Electrons are capacitively induced in the strained silicon channel by the metal gate with positive biases. (The metal gate is not shown here, and the oxide is partially shown for brevity)

2.4.3 A Quantum Device on an Undoped 2DEG

A similar Schottky split-gate technique was utilized to deplete electrons and pattern a 2DEG into a QD device on an enhancement-mode undoped 2DEG. The main difference comes from the process complexity. Since an enhancement-mode 2DEG has an insulator and a metal gate on top of the Si/SiGe heterostructures, these depletion gates are inserted between the oxide and the Si cap layer to enable 2DEG effective patterning (Fig. 2.8a and 2.8b). (We note here that recently a very thin aluminum oxide ~3 nm is deposited underneath the depletion gates to prevent possible leakages [15]). From the viewpoint of process flow, the fine splitting gates must be deposited before oxide and metal (here we call it as a universal gate) deposition, which could lead to a risk to contaminate the oxide deposition chamber. In addition, the oxide thickness must be thick enough to prevent any leakage between the universal gate and the depletion gates. Its thickness is essential to avoid leakages from contacts (not shown here) to the universal gate as well.

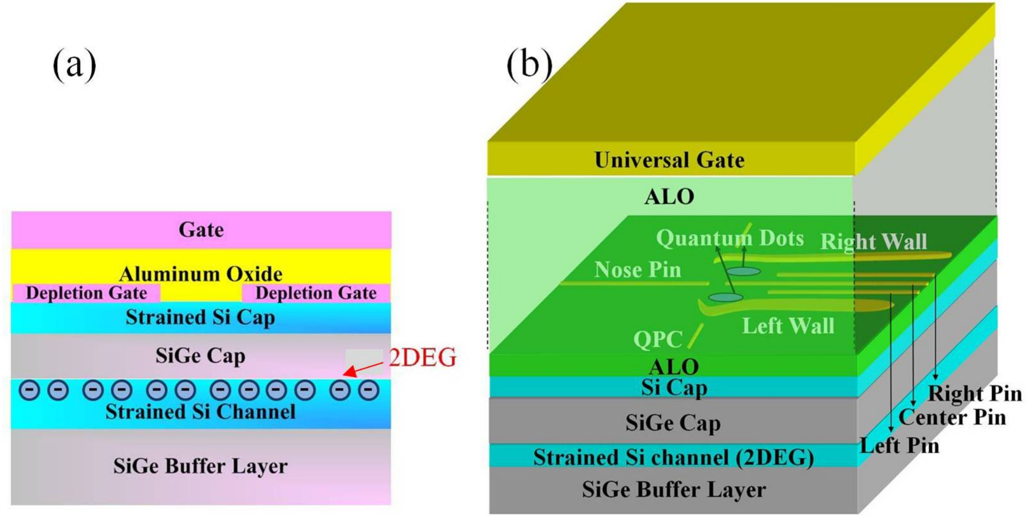

Figure 2.8: (a) The layer structure of an enhancement-mode undoped 2DEG with depletion gates inserted between an oxide and a surface silicon cap. Electrons in the strained silicon channel can be patterned by these depletion gates. (b) A three dimensional view of a quantum dot device fabricated on an enhancement-mode 2DEG [15, 36, 37].

The absence of any intentional doping atoms leads to extremely low Schottky gate leakage for the splitting gates. However, its depletion capability is now limited by the SiGe cap thickness, which is also the distance between a 2DEG and charged impurities at the interface. A thinner SiGe thickness is preferred because the electrical potential from the depletion gates to the strained silicon channel is sharper. A precise electron confinement is thus possible in the nanometer scale. However, Coulomb forces between charged impurities and electrons in the channel become stronger with a decreasing SiGe cap thickness. Electron mobility could be significantly degraded due to the scattering from those charges. The compromise between these two issues comprises the backbones of Ch. 5, Ch. 6 and Ch. 7. More details about enhancement-mode undoped strained silicon 2DEG will be discussed in those three chapters.

Chapter 3

High Breakdown Voltage Schottky Gating of Doped Silicon 2DEGs

3.1 Introduction

A Schottky split-gate technique on a Si/SiGe modulation-doped two-dimensional electron gas (2DEG) with negative biases has become a common way to define lateral quantum dot arrays as we described in Ch. 2 [34]. A negative bias on the gate should fully deplete the 2DEG to pattern it into quantum dots. However, the well-known surface segregation of phosphorus from the doped electron supply layer into the following SiGe/Si capping layers during growth can cause a high electric field at the sample surface when a reverse bias is applied. This high field leads to the tunneling of electrons from the metal to the semiconductor, resulting in undesirable gate leakage, which degrades the reliability of the split gate technique.

In this section, we demonstrate a large reduction in gate leakage by suppression of phosphorus surface segregation during sample growth. In collaboration with Jiun-Yun Li, we successfully reduced the surface phosphorus level down to $2{\times}10^{16}$ cm^{-3} by lowering the growth temperature of the SiGe cap layer [40]. A much higher breakdown

voltage (-7 V) was achieved in the sample with such a low surface phosphorus level, compared to -2 V from the sample with a high surface phosphorus concentration (1×10^{18} cm^{-3}). This great improvement in breakdown voltage thus provides a wide window to deplete a 2DEG fully, or shut off the channel, without significant gate leakage.

3.2 Suppression of Phosphorus Surface Segregation

The surface segregation of phosphorus is not a new issue in silicon epitaxial growth. It was found that, during growth, phosphorus atoms preferentially jump from the subsurface layer to surface sites because surface sites have lower energy [41]. In the growth of a modulation-doped silicon 2DEG, phosphorus atoms from the intentionally doped layer keep switching crystalline sites with surface host atoms (Si or Ge), leading to a high concentration at the sample surface (Fig. 3.1). For example, growing cap layers at 575 °C in RTCVD results in extensive phosphorus surface segregation, giving a phosphorus surface concentration after a nominally undoped SiGe cap layer thickness of 20 nm about 1×10^{18} cm^{-3} (Fig. 3.2).

In the CVD growth process, hydrogen is commonly used as a carrier gas. It covers the growth surface layer by forming Si-H or Ge-H bonds [42, 43], which could break easily under high temperature growth. Li et al. [40] reported that the hydrogen coverage on the growth surface may change the relative energy of surface and subsurface atoms, making phosphorus less energetically favored at the surface. To keep the hydrogen surface coverage high, the growth temperature for layers grown after n-SiGe supply layer is intentionally lowered (<575 °C). This high hydrogen coverage ratio successfully suppresses the segregation of phosphorus atoms towards the surface sites, leaving a relatively low P concentration at the sample surface. For example,

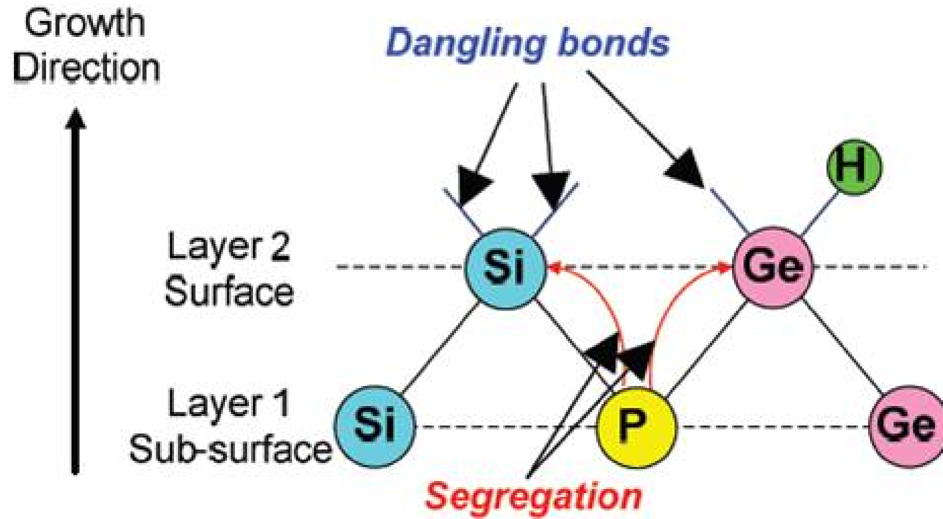

Figure 3.1: The schematic of atomic layer structures near the surface during the epitaxial growth for a doped 2DEG. (Image courtesy of Jiun-Yun Li [44])

the sample with its SiGe cap layer grown at 525 °C (50 °C lower than the sample shown in Fig. 3.2) shows a surface P level at 2×10^{16} cm^{-3} (Fig. 3.3), which is almost two orders of magnitude lower than the case shown in Fig. 3.2.

3.3 Device Fabrication

Prior to putting complicated split gates on a modulation-doped 2DEG to make a quantum device, a simple Hall bar with a Schottky gate across it was first made to check gate leakage current and test depletion capability of the gate. This set of devices was made both on samples with high (Fig. 3.2) and low (Fig. 3.3) surface P levels for comparison. After epitaxial growth by rapid thermal chemical vapor deposition (RTCVD), 2DEGs were then etched as Hall bars and AuSb was deposited as contacts followed by 450 °C annealing for 10 minutes. Pd was finally deposited across the Hall bar to form a Schottky gate. A simple schematic of a device cross section is shown

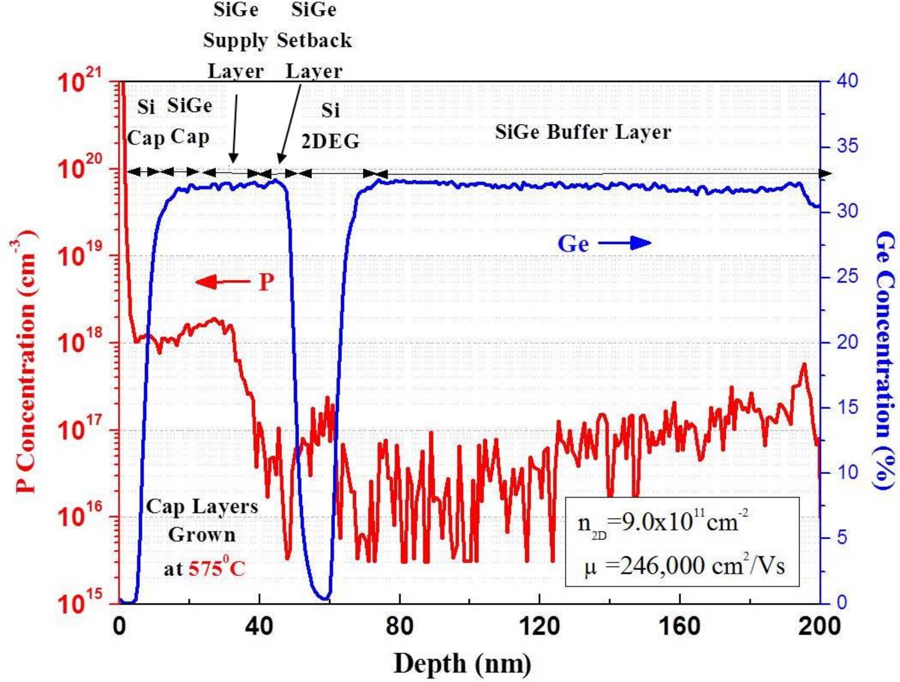

Figure 3.2: A SIMS profile for the sample with a cap layer grown at 575 °C. The phosphorus bump in the Si 2DEG is a SIMS artifact.

in the inset of Fig. 3.4. The mobility of 2DEG samples used in this study is above 200,000 cm^2/Vs and 2D electron densities are in the range of 5~9×10^{11} cm^{-2}.

3.4 Gate Leakage Test at 4.2 K

Negative biases applied on splitting Schottky gates of a doped 2DEG deplete electrons in the channel to pattern them. However, before we test the depletion capability of Schottky gates, we need to assure that the gate leakage current (reverse current in the Schottky diode) is negligible at least in a wide enough range of negative biases at 4.2 K. In the case of the sample with the cap layer grown at 575 °C (blue circles in Fig. 3.4), a high electrical field near the surface due to high surface P concentration results in considerable gate leakage at a very small negative bias (~ -1 V) and its breakdown voltage is smaller than -2 V. In contrast, a very high breakdown voltage

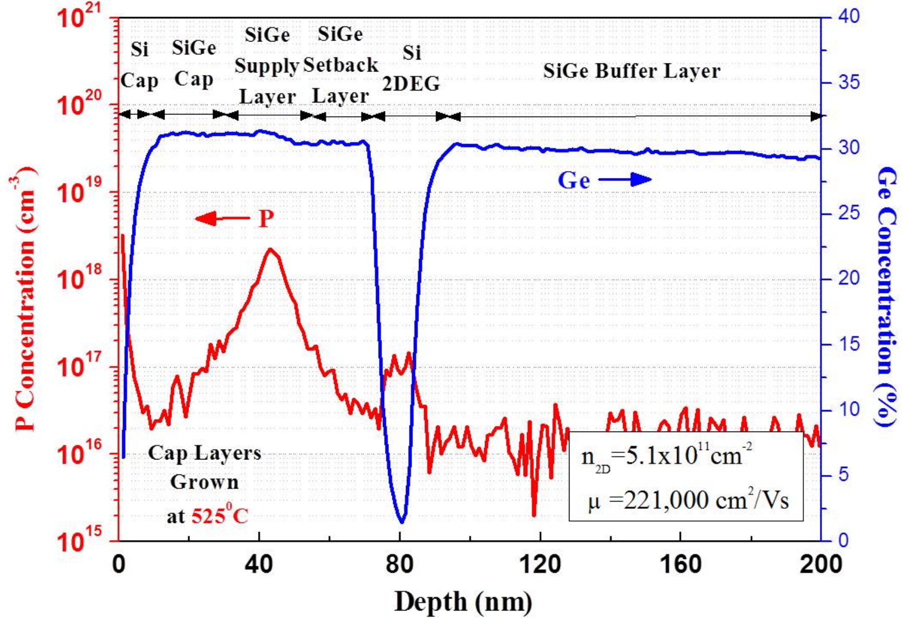

Figure 3.3: The phosphorus segregation can be greatly suppressed by lowering cap layer growth temperature from 575 °C to 525 °C [40]. The phosphorus surface concentration is reduced as low as 2×10^{16} cm^{-3}. The P peak at surface is a typical artifact resulted from the surface effect in a SIMS measurement.

(~ -7 V) was achieved in the sample with the cap layers grown at 525 °C (red squares in Fig. 3.4). A wide range of negative biases without significant gate leakage enabled us to examine the depletion capability of this Pd Schottky gate next.

3.5 Depletion of Doped 2DEGs

A depletion test was then done in the sample with the SiGe cap layer grown at 525 °C. With a small voltage (~1 mV) between source and drain, a current flowed in the channel at zero gate bias. To test the efficiency of the Pd Schottky gate, we gradually increased the negative bias applied on the Schottky gate deposited across the channel. When the bias was less than -0.5 V, the drain current was still on and its level is around 130 nA, while the gate leakage current was 0.1 nA, which is the

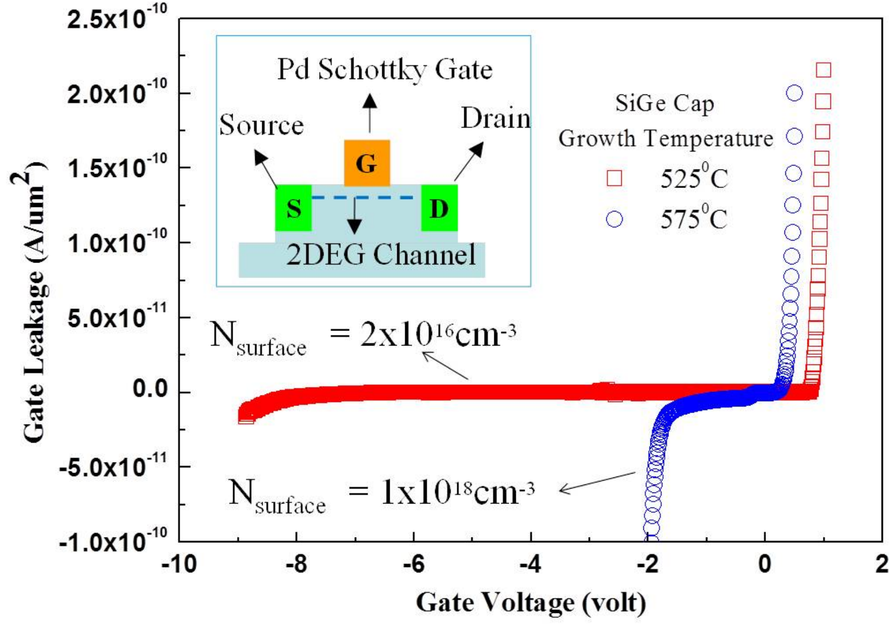

Figure 3.4: Schottky gate leakage test at 4.2 K. The inset shows the cross section of a test device.

detection limit of this measurement (Fig. 3.5). When the bias was increased over -0.5V, the channel was shut off sharply. The drain current plummeted down to ~0.1 nA, the same level as the gate leakage current (the detection limit). No significant gate leakage was detected up to -2 V, which is consistent with the results from previous gate leakage test in the same sample.

3.6 Quantum Point Contact Test

A quantum point contact (QPC) is commonly integrated into quantum-dot devices as a charge sensor (Fig. 2.6). In contrast to the measurement of the current through the dot, which might be destructive to fine features, the QPC technique measures the tiny conductance change through the channel between QPC and the outer gate of quantum dots. The conductance change of a QPC has been confirmed to be very sensitive to its

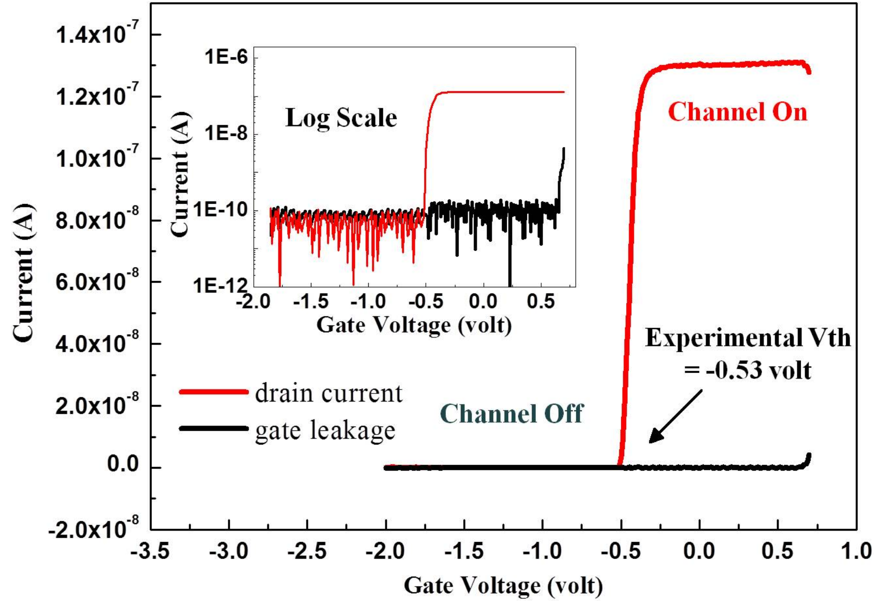

Figure 3.5: Depletion test at 4.2 K of the sample with a cap layer grown at 525 °C. Both drain and gate leakage currents are shown in log scale in the inset.

electrostatic environment nearby and effective for measuring the number of electrons in dots [45, 46, 47].

The conductance through a QPC is quantized due to the narrow channel width. People noticed that a QPC is very sensitive especially as its quantized conductance is being turned on, where a small change in gate voltage leads to a considerable shift of conductance. Therefore, to maximize the sensitivity of a QPC, the width of the channel (The distance between QPC and the outer gate of a quantum dot) becomes essential. If the channel width is too wide, gates may not be able to completely shut off the channel. On the other hands, if the width is too narrow, the channel could be shut off too sharply. This resulting narrow bias window increased the difficulty in QPC operation. In the following QPC test, we designed five different sets of gates with various spacing, 80, 130, 180, 230 and 280 nm (inset of Fig. 3.6). By measuring

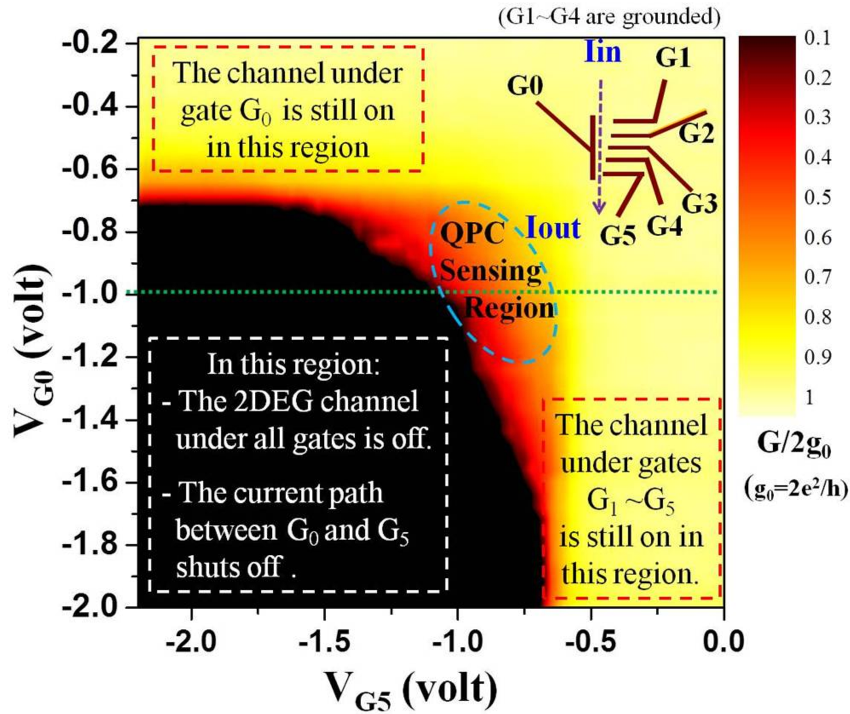

Figure 3.6: Successful QPC test at 4.2 K without any leakage. A wide transient region is observed. The inset shows the schematic of the QPC test structure.

the conductance through these five different sets of gates, the best gap width to sense remote charges from a nearby quantum dots can be determined [45] (Fig. 3.6).

A QPC device was fabricated on the sample with very low gate leakage across a wide range of negative biases (Fig. 3.7) This QPC device sat on an etched mesa (dark grey regions), which extended conducting 2DEG regions out to eight ohmic contacts at the end. The fine gates, defined by ebeam-lithography on the mesa, were connected by eight other photo-lithography-defined Pd (wide bright regions) contacts climbing over the mesa for subsequent electrical controls.

To observe the change in conductance through the channels with various widths, negative biases were applied on G_0 and one of G_1 to G_5 simultaneously with all other gates grounded. A typical QPC conductance measurement is shown in Fig. 3.6, where

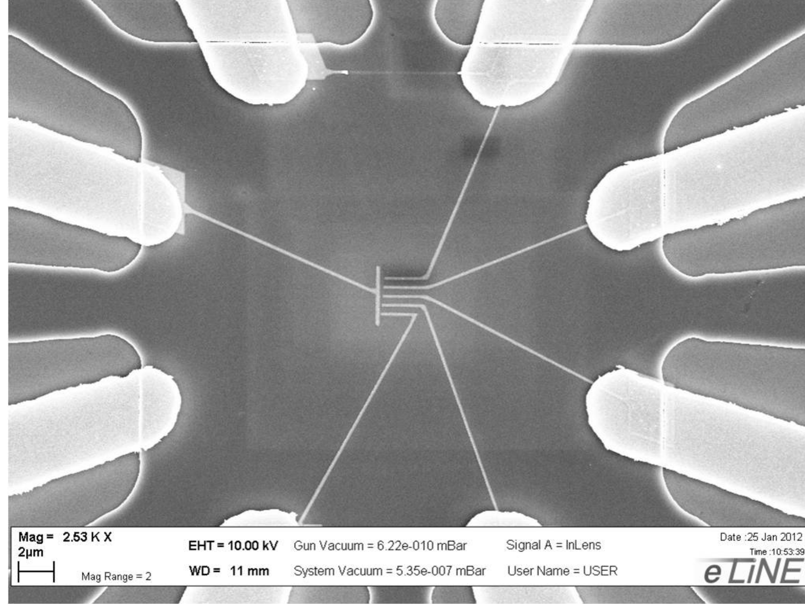

Figure 3.7: A SEM image of a typical QPC test device.

G_0 and G_5 were biased with G_1 to G_4 grounded. Note that darker color means lower conductance. In this case, the black regions on the left bottom (while the negative biases on G_0 and G_5 were both higher than -1 V) show no conduction either through the channel between two gates or under any gate. In contrast, once one of gates was biased below around -0.6 V, the channel is fully open and very high conduction (bright yellow regions) was observed.

However, as we mentioned above, QPC reaches its highest sensitivity when the conductance is half of the quantized conduction. That means two gates should be biased properly so that the conduction between them is in orange regions. In this case with G_5 (the channel width is 80 nm), the bias window for both gates is around 0.3 V (-0.7 V to -1 V), which is fairly wide. Here we fixed G_0 at -1 V and compared the conductance between G_0/G_1 and G_0/G_5 (Fig. 3.8). For the gap width ~280 nm (between G_0 and G_1), the current flowing in the gap could not be closed for any voltages. The high sensitivity was observed with the narrowest gap width ~80 nm

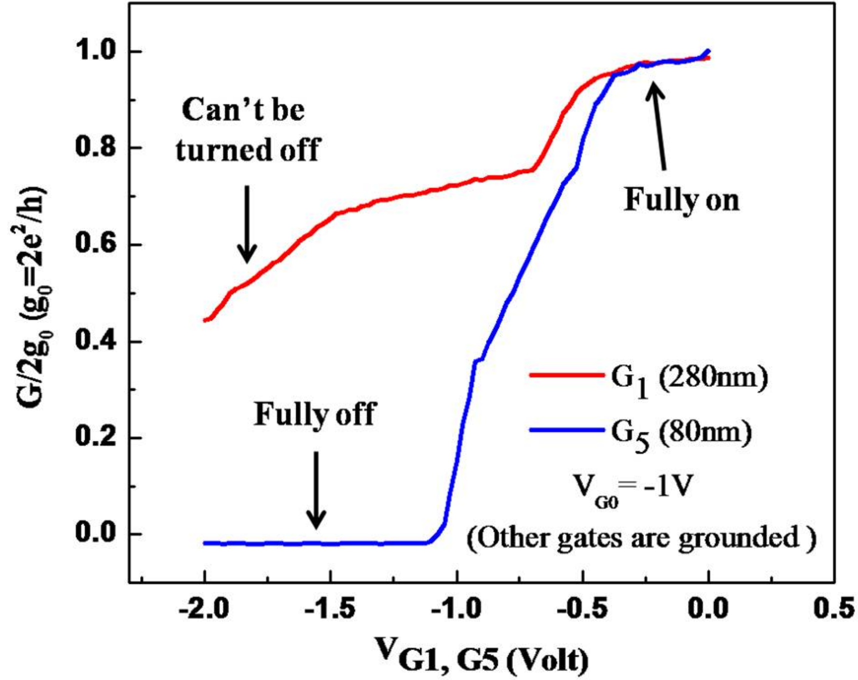

Figure 3.8: The channel between G_0 and G_1 remains on at -2 V but the channel between G_0 and G_5 can be fully shut off.

(between G_0 and G_5) where the current in the gap could be turned completely on and off within small gate voltages (Fig. 3.8).

3.7 Summary

In this chapter, we demonstrated suppression of phosphorus segregation by lowering growth temperature (525 °C) for the SiGe cap layer in a modulation-doped 2DEG. The resulting low surface P concentration reduced the electrical field at the surface under reverse bias, leading to a high breakdown voltage of Schottky gates. The wide range of negative biases without significant gate leakage enabled us to perform a successful depletion test where the Schottky gate shut off the 2DEG channel effectively. A QPC test device was then fabricated to determine the best channel width between

QPC and outer gate of a quantum dot to reach its highest sensitivity as a charge sensor.

Chapter 4

Implant Isolation of Silicon 2DEGs at 4.2 K

4.1 Introduction

As we discussed in Ch. 2, the state-of-the-art single-electron quantum-dot devices based on the Si/SiGe material system are typically fabricated in modulation-doped (depletion-mode) or undoped (enhancement-mode) 2-D electron gases (2DEGs) [15, 34, 48]. 2DEGs are usually electrically isolated by mesa etching. However, the mesa edges can cause problems for subsequent fabrication steps, such as the application of electron-beam resist for submicrometer gates to form quantum dots and thin metal step coverage. In addition, in enhancement-mode devices, high electrical fields in the gate insulator above the corner of the etched mesa may cause breakdown of the insulator or leakage currents.

Ion implantation for lateral electrical isolation (implant isolation) on III-V materials has been a well-known technique for several decades [49]. Ion bombardment creates deep defect levels, and these defects trap free electrons and pin the Fermi level near midgap, resulting in high resistivity. This process not only provides excellent

electrical isolation but also preserves the planarity of the surface. However, relatively few papers have focused on implant isolation in Si-based devices [50], because the resulting high-resistivity regions cannot sustain post-isolation high-temperature processes (>1000 °C) common in silicon technology. Furthermore, the resistivity of the intrinsic silicon (Fermi level at mid-gap) is ~2×10^5 Ω·cm at room temperature, which is not high enough for most applications. However, the processing of Si/SiGe-based quantum devices is often constrained to be below 600 °C to avoid Si/Ge interdiffusion [51], which could be low enough to avoid annealing of implant damage. Besides, the typical low operation temperature (4.2 K or less) of such quantum devices provides much less thermal energy for electrons to escape from implant-induced defects, so that resistivities much higher than those in silicon at room temperature should be possible.

In this chapter, we demonstrate implant isolation of modulation-doped Si 2DEG structures characterized at 4.2 K. Heavily-doped 2DEGs were used to examine the isolation capability as a worst case (high electron density of ~10^{12} cm^{-2}). The thermal stability was tested for different post-implant annealing temperatures up to 650 °C. The 2DEG quality (electron mobility) of samples processed with implant isolation was compared with ones with conventional mesa isolation by reactive ion etching (RIE). All the work of this chapter is summarized in [52].

4.2 Sample Growth and Test Device Fabrication

The layer structure of the modulation-doped Si 2DEGs used in this study is shown in Fig. 4.1. Their Hall mobility, electron density, and sheet resistance at 4.2 K are in the range of 80,000 to 150,000 cm^2/Vs, 0.8 to 1.6×10^{12} cm^{-2}, and 30 to 80 Ω/□, respectively. The structures were all grown on $Si_{0.72}Ge_{0.28}$ graded buffer substrates by rapid thermal chemical vapor deposition (RTCVD) between 575 °C and 625 °C. A

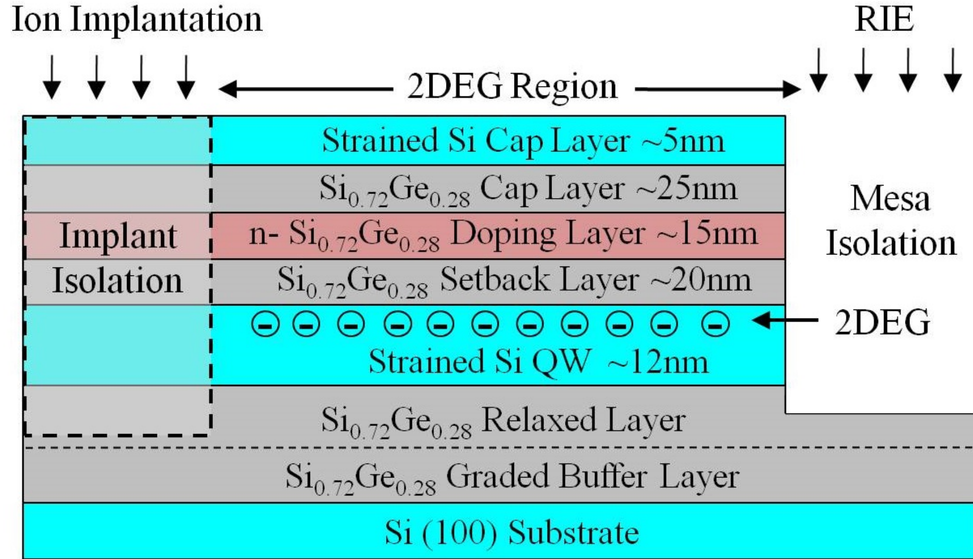

Figure 4.1: The layer structure of a test sample. The layers above the horizontal dotted line were grown by RTCVD. To pattern the 2DEG, only one of implant isolation or conventional mesa isolation by RIE is used on a single sample, but both are illustrated in this figure for brevity.

test device consists of a set of separated Ohmic contacts to test the implant isolation, a set of connected Ohmic contacts to measure original resistivity from a 2DEG, and a Hall bar structure (in a single 2DEG region) with Ohmic contacts to measure electron mobility and density (Fig. 4.2).

After 2DEG growth, a 400-nm screen silicon dioxide layer was first deposited by plasma-enhanced chemical vapor deposition (PECVD) at 250 °C. Ohmic contact regions to the 2DEG were then defined by photolithography and diluted HF wet etching of the oxide. 1% Sb-doped Au was thermally evaporated followed by lift-off. Annealing at 450 °C for 10 minutes to form Ohmic alloyed contacts was performed before the ion implantation except for samples later annealed at 550 °C or 650 °C, where the contacts were formed after 550 °C or 650 °C steps. The areas to be isolated were then defined by photolithography and diluted HF wet etching of the oxide.

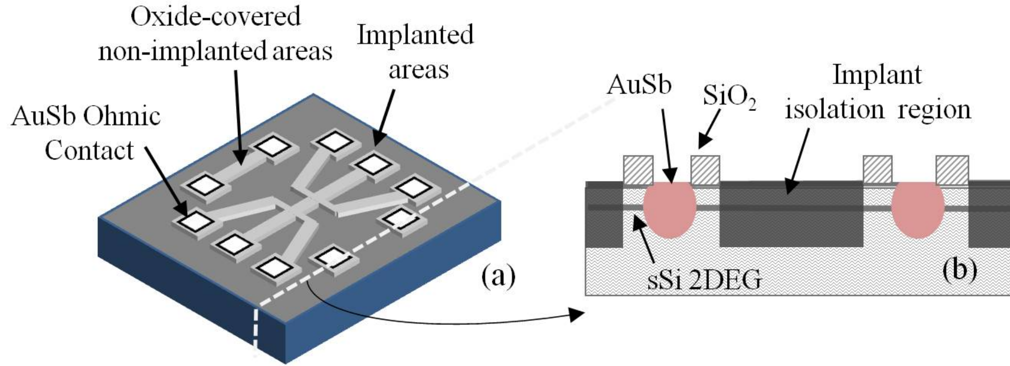

Figure 4.2: (a) The schematic of a test device (not to scale). It consists of 1 Hall bar structure, 1 set of connected contacts and 1 set of isolated contacts. The cross session of the set of isolated alloy contacts indicated by the white dot line is shown in (b).

4.3 Implant Conditions

Isolation tests were done by implanting separately argon (Ar^+) and silicon (Si^+) ions into different samples. Si and Ar were chosen due to their electrical neutrality in the Si/SiGe material system. Two implant energies were necessary in all regions because both the 2DEG channel and the doping layer (if doped above the metal-insulator transition level) [53] could conduct electricity at low temperature. A simulator, the Stopping and Range of Ions in Matters (SRIM) [54], was used to simulate the profile of implanted species and the resulting Si and Ge vacancies. This information helped us to choose two ion implantation energies: 30 keV and 60 keV, which created defects near the depth of the shallow doping layer (30 keV) and near the deeper strained Si 2DEG channel (60 keV), respectively (Fig. 4.3).

Silicon amorphized by a high dose implant (~5×10^{14} cm^{-2} for Si^+ into Si at 40 keV) [55] can be recrystallized by solid phase epitaxy (SPE) at a temperature as low as 500 °C, which would lead to poor thermal stability of the damage [56]. Further, SiGe alloys are even more easily amorphized by ion implantation than Si due to weaker bonding between Si and Ge atoms [57]. Therefore, doses well below 5×10^{14} cm^{-2} were used. Ar^+ or Si^+ was then implanted at room temperature with three

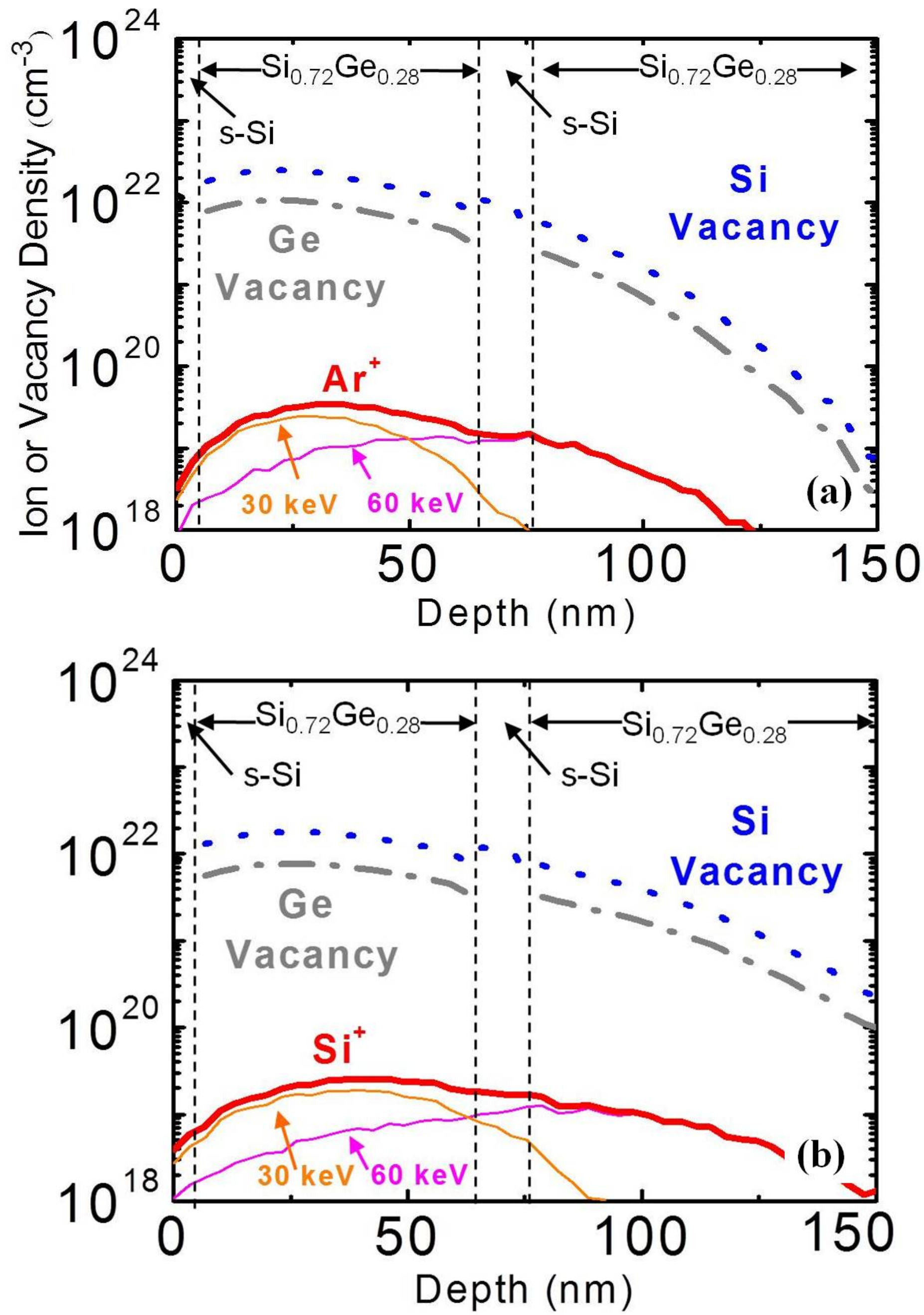

Figure 4.3: Simulation of implanted species and resulting vacancy distribution in a 2DEG structure by the Stopping and Range of Ions in Matters (SRIM) software [54]. Two-step implantation (1×10^{14} cm^{-2} @ 30 keV+1×10^{14} cm^{-2} @ 60 keV) with implanted species (a) Ar^{+} and (b) Si^{+} is used in this simulation. The target is assumed to be implanted at 0 K.

different test doses: 5×10^{11} cm^{-2} (denoted as low dose), 1×10^{13} cm^{-2} (medium dose) and 1×10^{14} cm^{-2} (high dose), and each dose was implanted at two energies, 30 keV and 60 keV.

In addition, Hall bars defined by conventional mesa isolation by RIE were also made for 2DEG quality comparison. Ohmic contacts were made on one $Si_{0.72}Ge_{0.28}$ graded buffer substrate separately without implant isolation to test its resistivity at 4.2 K for reference.

4.4 Ultra High Sheet Resistance at 4.2 K

The isolation capability at 4.2 K was examined by two-point measurements between two implant-isolated 2DEGs. The sheet resistances of isolated regions for all six implant conditions are all above 1×10^{12} $\Omega/\square$, which is ten orders of magnitude higher than the original 2DEG sheet resistances (Fig. 4.4). In some cases, the sheet resistance is as high as 1×10^{13} $\Omega/\square$, close to the instrumental limit. Since the sheet resistance of the $Si_{0.72}Ge_{0.28}$ graded buffer substrate at 4.2 K was also high (~5×10^{12} $\Omega/\square$), the remaining conduction might occur either in the SiGe graded buffer or in the implanted regions. In any case, it is clear that the implant isolation for all three doses is extremely effective.

4.5 Thermal Stability

Thermal stability issues could arise when we integrate the implant isolation technique into a device fabrication process, such as insulator deposition and contact annealing. Aluminum oxide deposited by atomic layer deposition (ALD) is a common insulator used on enhancement-mode Si 2DEG devices due to its high quality and low deposition temperature (≤ 300 °C) [58]. To test the thermal stability at the oxide deposition temperature, samples were annealed at 300 °C for 1 hour and their sheet resistances

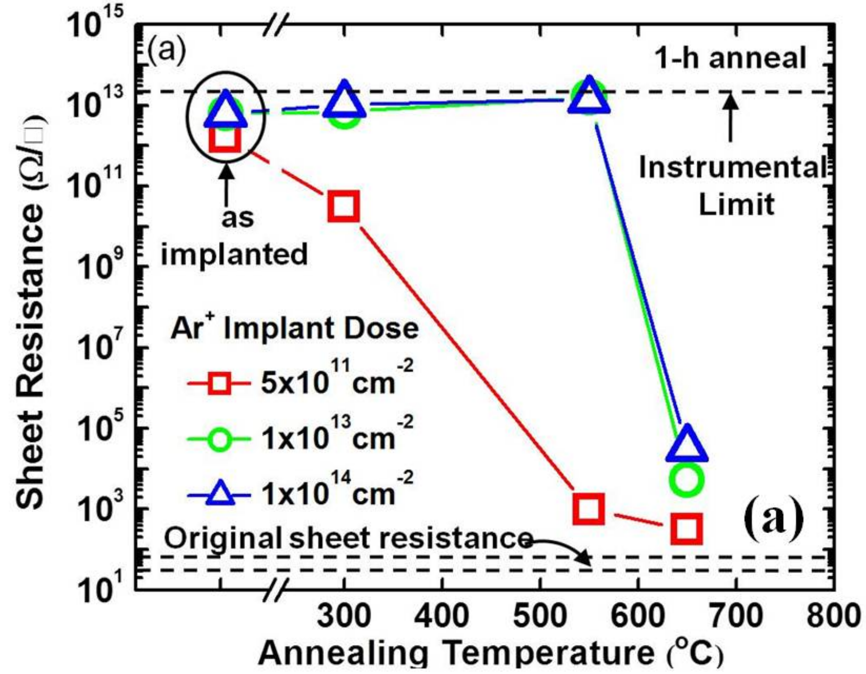

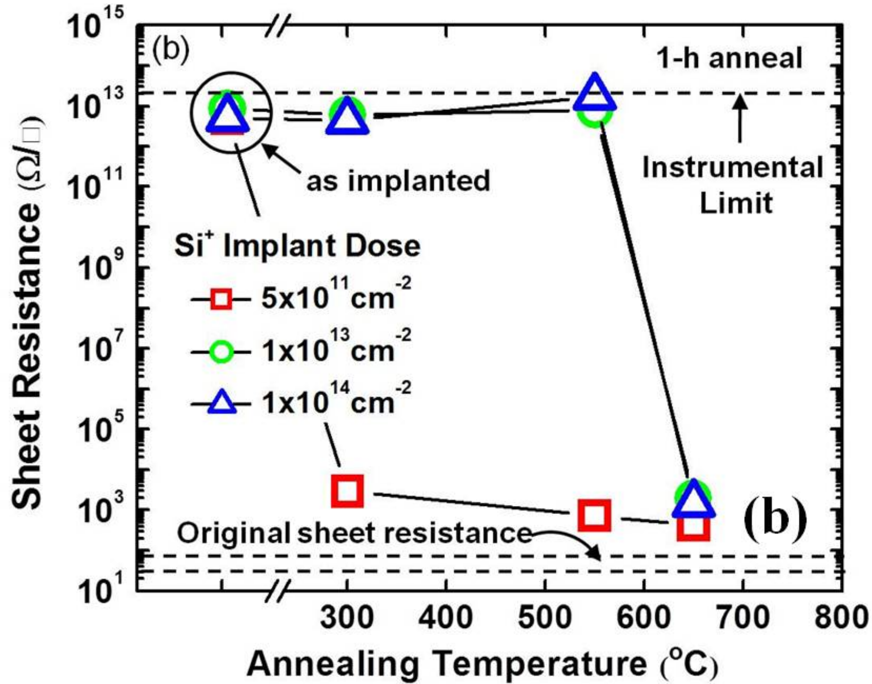

Figure 4.4: Isochronal (1 hour) annealing behavior of sheet resistances of 2DEG samples at 4.2 K implanted with (a) Ar^+ and (b) Si^+ with three various doses, 5×10^{11} cm^{-2}, 1×10^{13} cm^{-2} and 1×10^{14} cm^{-2} at 30 keV and 60 keV. Also shown are the range of sheet resistance of the starting 2DEGs, and the experimental instrumental limitation. The estimated error of sheet resistance is $\pm18\%$ for (a) and 27% for (b).

were measured at 4.2 K (Fig. 4.4). For samples implanted with medium and high dose, the sheet resistances stay high at ~1×10^{13} Ω/□ regardless of implant species, while for ones implanted with a low dose, the sheet resistances drop to 3×10^{10} Ω/□ and 3×10^{3} Ω/□ for Ar^{+} and Si^{+} implant respectively. Since implantation with the lowest dose (1×10^{11} cm^{-2}) produces the fewest defects (mostly point defects), the damage can easily be annealed and thus the sheet resistance decreases. In addition, the higher sheet resistance of low dose Ar^{+}-implanted sample than Si^{+}-implanted one after 300 °C annealing might be explained by a higher damage level caused by Ar^{+} due to its heavier atomic mass.

Antimony-doped gold is commonly used on both depletion-mode and enhancement-mode Si/SiGe devices to form Ohmic alloyed contacts after annealing [58]. However, in enhancement-mode devices, the necessity of an overlap between the accumulated electrons in the channel under the gate and contacts for the continuity of conduction makes the requirement of a flat contact surface crucial to prevent possible leakage. Because alloyed contacts have rough surfaces, contacts made by n-type ion implantation before the deposition of the gate insulator are preferred [15, 48]. For heavily-phosphorus-implanted contacts, the activation of implanted phosphorus occurs at relatively low temperature ($\geq$ 500 °C) by SPE [56]. Hence, the thermal stability of implant isolation samples was again tested after 550 °C annealing for 1 hour. Sheet resistances of the medium and high dose samples at 4.2 K are still as high as 1×10^{13} Ω/□ (Fig. 4.4). After further annealing at 650 °C for 1 hour, the sheet resistances of the medium and high dose samples at 4.2 K drop nine orders of magnitude. Therefore, if an annealing temperature for the contact over 550 °C is desired, it should be done before implant isolation.

4.6 2DEG Quality Check

Any possible degradation of the 2DEG quality due to spurious radiation during ion implantation was investigated based on Hall mobility measurements by standard low frequency lock-in techniques at 4.2 K. Fig. 4.5 shows the ratio of mobility measured from implant-isolation-defined Hall bars to RIE-defined ones (with absolute mobility values shown in parentheses) on the same CVD growth and annealing conditions. Implanted samples without annealing (open symbols) do not show any significant mobility degradation. Even with the highest dose used in this study (1×10^{14} cm^{-2}), the 2DEG quality remains unaffected. Mobility ratios of samples experiencing both implant isolation and 550 °C annealing are also shown in Fig. 4.5 (closed symbols). Except for one sample, the mobility ratios after 550 °C annealing are near 100%. We attribute the low mobility ratio for the medium dose Ar^+-implanted sample to a non-uniformity in the 2DEG growth between different wafer pieces used for the Hall bars.

4.7 Summary

Successful lateral electrical isolation of silicon two-dimensional electron gases (2DEGs) at liquid helium temperature (4.2 K) by ion implantation is demonstrated. The sheet resistance of the implanted regions can be achieved as high as 1×10^{13} $\Omega/\Box$ at 4.2 K. Thermal stability up to 550 °C makes the technique compatible with most subsequent processing steps to fabricate silicon quantum devices. It has also been confirmed that the 2DEG quality is not degraded by the ion implantation, based on a comparison of Hall mobility of implant-isolated samples with conventional reactive-ion-etching (RIE)-defined samples.

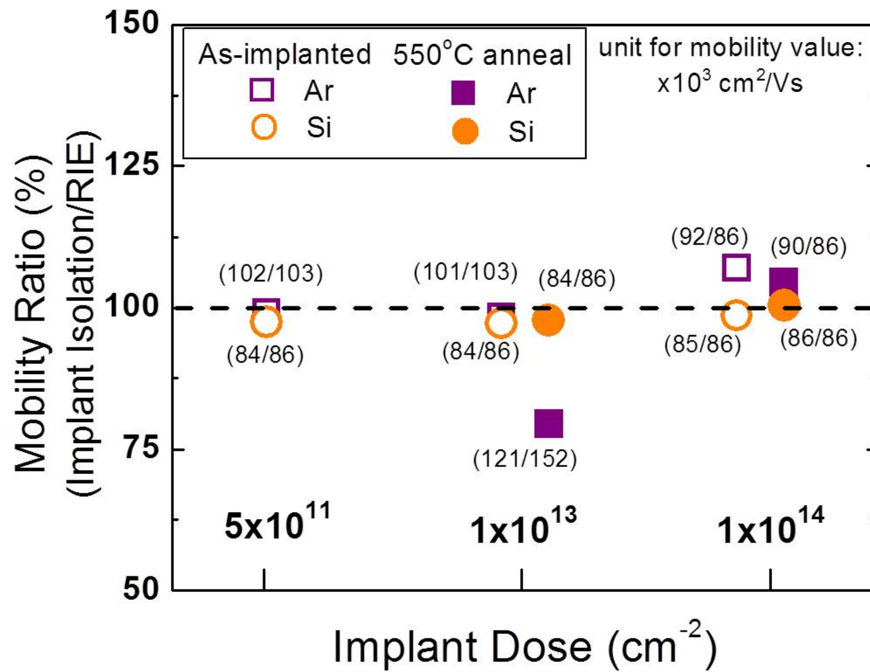

Figure 4.5: Comparison of 2DEG quality after implant isolation or RIE process by the ratio of the mobility at 4.2 K measured from an implant-isolation-defined Hall bar to a RIE-defined Hall bar for a given implant and anneal. The absolute mobility values at 4.2 K with a unit of 10^3 cm^2/Vs are shown in parentheses with the mobility for implant isolation before the mobility for mesa isolation. The estimated error of mobility measurement is $\pm5\%$.

Chapter 5

Enhancement-Mode Undoped Silicon 2DEGs

5.1 Motivation

The silicon-based material system is attractive for the implementation of single-electron quantum dot (QD) devices for quantum computing applications owing to the longer spin coherence time of electrons in silicon compared to that in III-V compounds [58, 59]. Current research interests are focused more on enhancement-mode quantum devices in undoped silicon two-dimensional electron gases (2DEGs) due to the absence of ionized dopants, which are possible sources of disorder and potential fluctuations in Si 2DEGs [39, 60, 61]. In an enhancement-mode structure, a strained-silicon quantum well (QW) which confines a 2DEG is buried below the surface to reduce the scattering from remote charges from the semiconductor surface. Weaker Coulomb forces due to both the absence of ionized dopants and a longer distance between surface charges and electrons lead to a cleaner 2DEG system where the interference to spin manipulation could be mitigated and electron mobility could be enhanced.

The laws of physics do not show a direct link between electron mobility and electron spin coherence time, but qualitatively speaking, the electron mobility does reflect the detrimental influence from charged impurities in a 2DEG system. In addition, the easier process steps for a Hall bar device and the faster low-temperature Hall measurements (which measures mobility) compared to spin relaxation experiments do provide a beneficial measure of the cleanliness of a strained silicon 2DEG system.

To confine a single electron in a quantum dot, a low minimum electron density in the 2DEG enables larger tolerances in both the size of a quantum dot device and the bias window for depletion gates. Furthermore, a 2D electron density is also an essential parameter to reflect a 2DEG quality because, theoretically, the lowest mobile electron density that is measurable at liquid helium temperature is strongly related to the density of remote charges at the oxide/silicon interface. To sum up, higher electron mobility and lower measurable electron density of an enhancement-mode strained silicon 2DEG qualitatively represent the good quality of a 2DEG system which may yield a longer spin coherence time. A Hall measurement at 4.2 K is a fast and easy measurement to obtain these properties.

5.2 Models for Mobility Limitation

To enhance electron mobility of undoped silicon 2DEG samples grown in our RTCVD, understanding the mobility-limiting mechanisms is the first step. Historically, much work was done to figure out the dominant scattering mechanisms on electron mobility in a MOSFET [62]. The silicon/silicon dioxide interface was identified as the key role that limits electron mobility, especially at high vertical electrical field, in addition to the phonon scattering at room temperature. Relevant scattering mechanisms for a 2DEG in GaAs/AlGaAs systems were also widely discussed in 1980s [63, 64, 65]. Thanks to these theoretical analyses along with plenty of experiments in the past

few decades, the most updated electron mobility record of a 2DEG in GaAs/AlGaAs material system has been improved to as high as near 40,000,000 cm^2/Vs at 0.3 K [66].

The discovery of electron confinement in strained silicon between two relaxed SiGe layers by Abstreiter et al. [22] in 1985 boosted the electron mobility record in Si/SiGe material system. In less than 10 years, the low-temperature electron mobility in a doped Si 2DEG was improved up to 500,000 cm^2/Vs, which was two orders of magnitude higher than before [30]. However, no systematic theoretical analysis on electron-limiting mechanisms in the Si/SiGe 2D electron system had been proposed until 1993. Monroe et al. [67] first analyzed possible scattering mechanisms that limit the mobility enhancement in the Si/SiGe system based on the previous discussions in silicon MOSFET and GaAs material systems. In the following section, we will use this literature to introduce the most dominant scattering mechanisms in detail.

5.2.1 Scattering from Background Charged Impurities

We can easily rule out phonon scattering because the operating temperature of quantum-dot devices based on silicon 2DEGs is commonly below 4.2 K (liquid helium temperature), where the phonon scattering is definitely negligible.

The first possible scattering mechanism limiting the electron mobility at 4.2 K in our samples could be scattering from background charged impurities in the 2DEG layer itself, which is usually denoted as background scattering [67]. The predicted electron mobility influenced by background scattering is:

$$\mu_{bs} = \frac{{g_v}^{\frac{3}{2}} {g_s}^{\frac{3}{2}} e {n_{2D}}^{\frac{1}{2}}}{4\pi^{\frac{1}{2}} \hbar N_b} \tag{5.1}$$

where g_v and g_s are valley degeneracy and spin degeneracy, respectively. N_b is the density of background charged impurities while μ_{bs} is the mobility limited by background scattering. Because of the high Fermi level in the 2DEG, donors may be

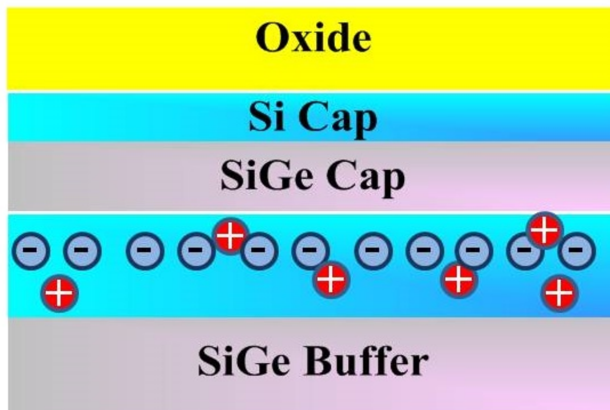

Figure 5.1: The schematic of background charged impurities in an undoped silicon 2DEG.

occupied and neutral. Neutral donors can also be strong scattering sites. For simplicity, when discussing and calculating background scattering in our modeling, we use Eq. 5.1 and set N_b to be the total number of background impurities, and ignore their charge states.

The background charged impurities are those impurities existing in the strained silicon channel where a 2DEG sits (Fig. 5.1). Due to their proximity to mobile electrons, the Coulomb forces from charged impurities can easily scatter electrons in the channel and thus deteriorate mobility. A higher density of background charged impurities leads to lower electron mobility. Furthermore, with electron density increasing, more electrons can screen each other from the scattering of background charged impurities. This so-called self-screening effect on background screening allows higher electron mobility at higher electron density, with a theoretical power law of 0.5.

5.2.2 Scattering from Remote Charged Impurities

Another major scattering mechanism is the scattering from remote charged impurities, usually denoted as remote scattering. In addition to charged impurities in the strained

silicon channel, charged impurities could be incorporated into grown layers during the growth, intentionally or unintentionally. For a doped silicon 2DEG, an intentional n-doped SiGe layer is designed to supply electrons into the strained silicon channel a few tens of nanometers away from the doping layer. This ionized impurity sheet with fairly high density (~10^{11} cm^{-2} or greater) results in strong Coulomb forces, scattering electrons in the channel strongly. For a conventional doped 2DEG in GaAs system with ultra-high mobility, remote scattering from the electron supply layer can be the dominant mobility-limiting mechanism [68].

In an undoped enhancement-mode silicon 2DEG, no intentionally doped layer exists anymore. Instead, charged impurities at the interface between the oxide and the strained silicon cap become the main sources of the remote scattering (Fig. 5.2). Although the predicted mobility model limited by remote scattering in [67] was proposed for a doped 2DEG sample, we could still apply it into an undoped 2DEG case due to the same nature of the scattering sources:

$$\mu_{rs} = \frac{16\pi^{\frac{1}{2}} g_v^{\frac{1}{2}} g_s^{\frac{1}{2}} e n_{2D}^{\frac{3}{2}} s^3}{\hbar N_r} \tag{5.2}$$

where N_r is the 2D density of remote charged impurities, and μ_{rs} is the mobility limited by remote scattering. s is the distance between silicon channel and the location of the remote charged impurity sheet. Since the SiGe cap thickness is usually much thicker than Si cap, the former usually represents s directly.

It is quite straightforward to understand from Eq. 5.2 that Coulomb forces from charged impurities could be reduced by making the SiGe cap thicker or the density of remote charged impurities lower. More detailed discussions about how to improve mobility limited by remote scattering in an undoped sample are in Sec. 5.6. Here we can also see the self-screening effect is described in this theoretical equation. The principle of self-screening on remote scattering is basically the same as the one on background scattering, but remote scattering has a higher power law, 1.5, meaning

Figure 5.2: The schematic of remote charged impurities at the oxide/silicon interface in an undoped silicon 2DEG.

that the theory predicts self-screening is more effective for remote scattering than background scattering.

5.2.3 Scattering from Si/SiGe Interface Roughness

The scattering from Si/SiO_2 interface roughness (denoted as interface roughness scattering) limits the electron mobility in a conventional silicon MOSFET in the high density regime. Despite very low interface charge densities in today′s advanced MOSFETs, the inherently different material nature between silicon and oxide causes roughness [69], reducing the mobility of electrons moving along this interface. Fortunately, electrons in an undoped silicon 2DEG are located in a buried silicon channel, hence the interface between silicon and oxide is not an issue anymore. Instead, they move along the interface between the strained silicon layer and the relaxed SiGe cap layer (Fig. 5.3). The Si/SiGe interface is expected to be superior to Si/SiO_2 interface in terms of the roughness not only because Si and SiGe have similar material properties, but Si and SiGe layers were epitaxially grown successively, without exposure out of the vacuum. The predicted mobility model limited by the scattering from interface roughness is as follows:

Figure 5.3: The schematic of Si/SiGe interface roughness in an undoped silicon 2DEG.

$$\mu_{irs} = \frac{e^5 {g_v}^3 {g_s}^3}{192\pi^4 \hbar (\epsilon\epsilon_0)^2 (\partial V/\partial z)^2 (\Lambda\Delta)^2 n_{2D}} \tag{5.3}$$

where Λ and Δ are characteristic length of the interface roughness and rms roughness, respectively. ∂V/∂z is a perturbation factor and μ_{irs} is the mobility limited by interface roughness scattering. In contrast to previous two scattering mechanisms, the mobility model limited by interface roughness scattering is reduced as 2D electron density increases. This is consistent with the experimental data from Si MOSFETs [70]. More electrons come in the channel from ohmic contacts as the higher positive gate voltage is applied, where a higher vertical electrical field confines electrons in the quantum well closer to the Si/SiGe interface, and thus enhances interface roughness scattering on mobility [71].

5.2.4 Other Possible Scattering Mechanisms

The strained silicon 2DEG system is much more complicated than a silicon MOSFET or GaAs 2DEG system because of the lattice mismatch of Si and Ge. In order to strain silicon to create the conduction band offset, relaxed SiGe layers are essential for a silicon 2DEG. Even state-of-the-art relaxed SiGe buffer layers contain various dislocation defects, including threading dislocations and misfit dislocations [23, 72,

73]. Therefore, the scattering from these dislocations may also influence electron mobility in a 2DEG system. Moreover, in practice, electrons in the strained silicon channel are not perfectly confined in the strained silicon channel due to finite barrier height. The tail of electron wave function may spread into the nearby relaxed SiGe layer, where alloy scattering from the random SiGe alloy could occur. By taking all scattering mechanisms into account, we can write the total theoretical mobility by Eq. 5.4.

$$\frac{1}{\mu_{total}} = \frac{1}{\mu_{bs}} + \frac{1}{\mu_{rs}} + \frac{1}{\mu_{irs}} + \cdots \tag{5.4}$$

In the following section, we will compare our experimental data with the total effect from the three different scattering mechanisms described here to see which mechanism dominates in 2DEG samples grown in our RTCVD.

5.3 Measurement of Enhancement-Mode Undoped Silicon 2DEGs

5.3.1 Device Fabrication and Measurement Setup

To study the electron transport properties of a strained silicon 2DEG at low temperature, an enhancement-mode Hall bar device is fabricated (Fig. 5.4) to measure mobility and 2D electron density at liquid helium temperature (4.2 K). First, a 200-nm silicon dioxide layer was deposited by plasma-enhanced chemical vapor deposition (PECVD) on the as-grown structure as an implant mask. The designated regions for Ohmic contacts were then defined by photolithography and wet etching of the silicon dioxide. A 3-step phosphorus implantation was conducted to assure the implanted species were deep enough to form contacts from the surface to the strained Si QW. Samples were then annealed at 600 °C for 1 hour to activate the implanted phos-

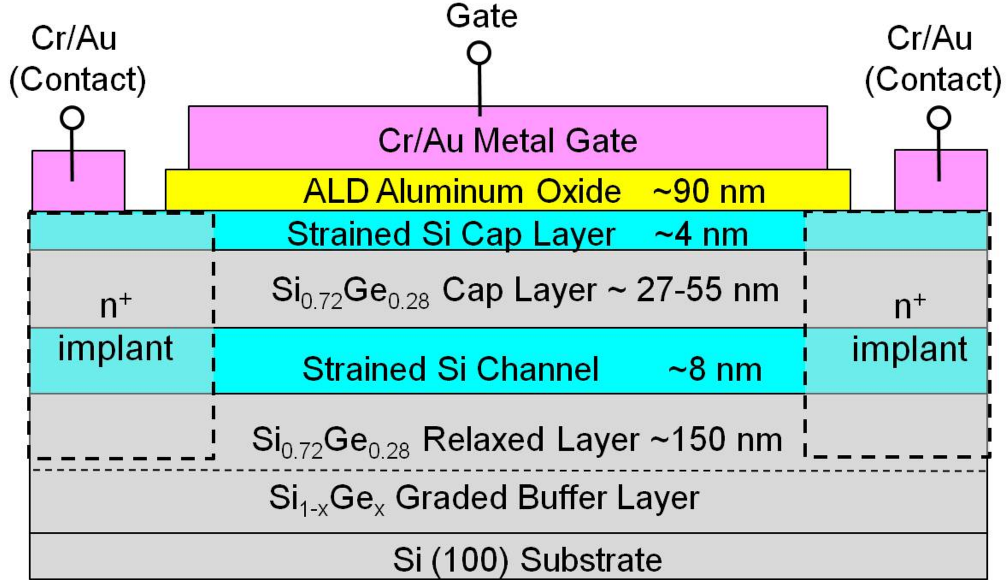

Figure 5.4: The layer structure of a typical undoped enhancement-mode strained silicon 2DEG.

phorus. Next, a 90-nm aluminum oxide was deposited by atomic layer deposition (ALD) at 300 °C as a gate insulator. Parts of the n^+ implanted regions were exposed by photolithography and wet etching of the aluminum oxide for metal deposition for contacts. After another photolithography step, a Hall-bar-shaped metal gate was finally formed by evaporating a 2-nm chrome and a 200-nm gold layer along with metal deposition on the exposed n^+ contact regions in the same evaporation.

We note that the metal gate must overlap with the n^+ contact regions to keep the continuity of conduction from the contacts to the 2DEG (Fig. 5.4). The process flow depicted above is standard for all samples discussed in this chapter unless otherwise noted. The top view of a standard enhancement-mode Hall bar device used in this study is shown in Fig. 5.5.

Hall measurements were then conducted at liquid helium temperature (4.2 K) with a magnetic field up to 2 T. The current source into the Hall bar is AC modulated with a low frequency (11 Hz) and a current level of 100 nA.

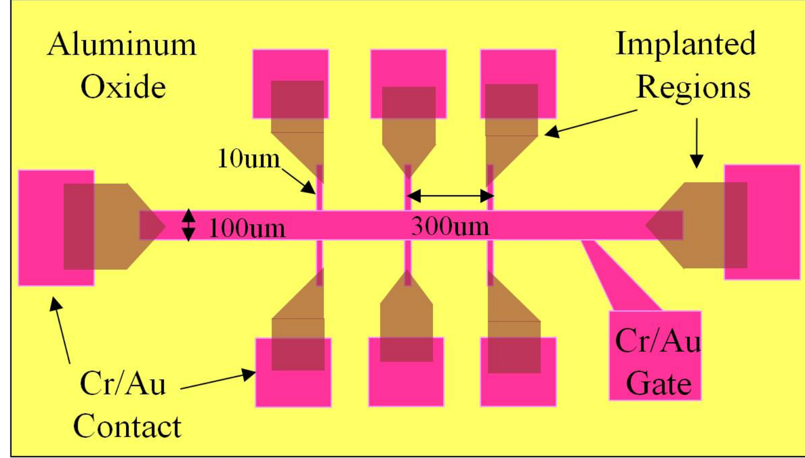

Figure 5.5: The top view of a standard Hall bar geometry used in this study. The magenta regions are Cr/Au metal stacks deposited in the same evaporation. The Cr/Au metal contacts are deposited directly on the silicon surface (etched holes of the aluminum oxide).

5.3.2 Parallel Capacitor Plate Model

When the gate voltage (V_G) is above the threshold voltage, electrons are capacitively induced to form a 2DEG, leading to the onset of channel conductance (The inset of Fig. 5.6). A typical gate voltage (V_G) dependence of the 2D electron density (n_{2D}) was thus obtained (Fig. 5.6). Since there are two strained silicon quantum wells (strained silicon cap and strained silicon channel) in a typical enhancemen-mode Si/SiGe 2DEG structure, a simple and quick parallel-capacitor-plate method is commonly used to identify the location of a gate-induced 2DEG instead of the time-consuming Shubnikov-de-Haas oscillation measurement [32]. Let′s assume this conducting 2DEG is in the strained silicon channel first. Thus between a metal gate and this conducting 2DEG, the oxide is equivalent to a capacitor (denoted as C_{ox}), which is in series with another capacitor from Si and SiGe cap layers (denoted as C_{sc}). Given the thickness of the aluminum oxide (with a relative dielectric constant of 9) , Si cap and SiGe cap shown in Fig 5.7, the equivalent theoretical capacitance calculated from this parallel capacitance plate model is 6.1×10^{-8} F/cm^2, which is very

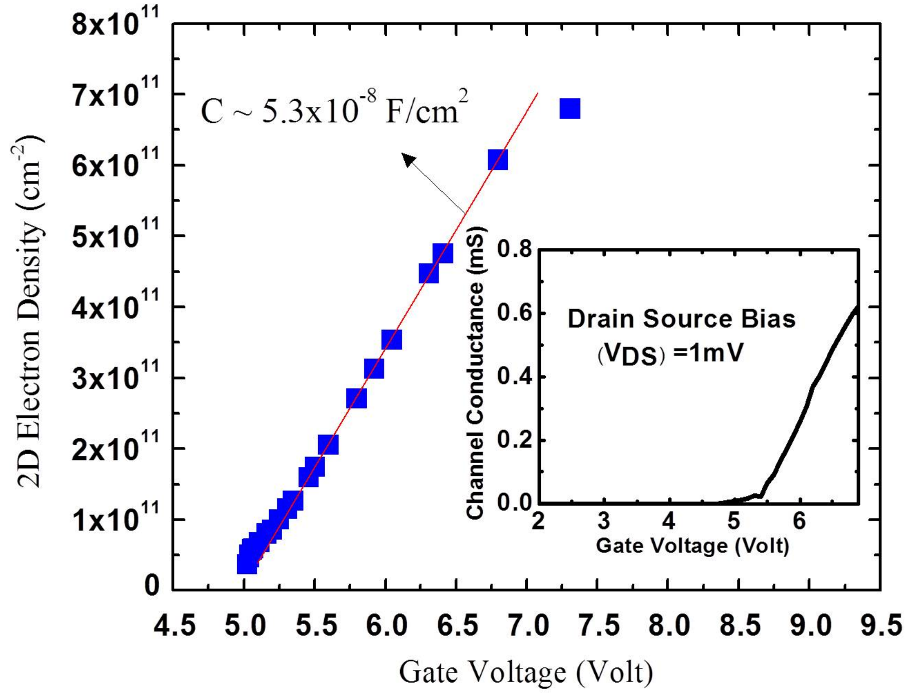

Figure 5.6: A typical linear V_G dependence of 2D electron density in an undoped enhancement-mode silicon 2DEG. The inset shows the channel turn-on with increasing gate voltages.

close to the experimental capacitance (5.3×10^{-8} F/cm^2) described by the slope of n_{2D} versus V_G in Fig. 5.6. This consistency strongly suggests that the electrons induced by the bias on metal gate are located in the strained silicon channel, not the silicon cap.

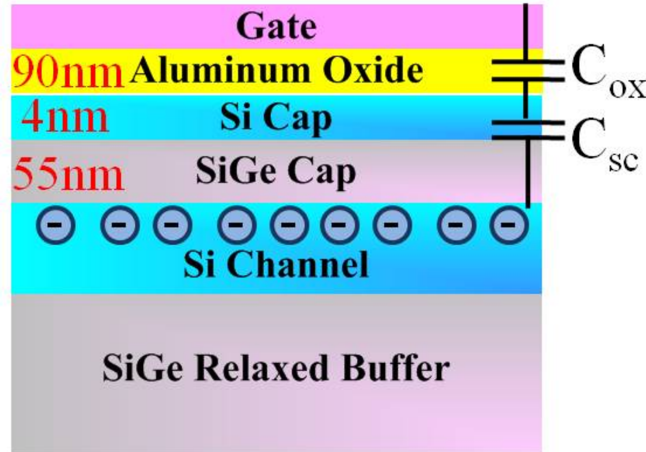

Figure 5.7: A schematic of two equivalent capacitors in series between metal gate and a conducting 2DEG in strained silicon channel.

5.4 Transport Property of Undoped Silicon 2DEGs

5.4.1 A Brief View of Various Scattering Mechanisms in Our 2DEGs

The Hall electron mobility measured from two typical undoped enhancement-mode silicon 2DEGs grown in our RTCVD system were plotted versus 2D electron density (Fig. 5.8). The layer structures for these two 2DEGs were the same except for the SiGe cap thickness. The highest μ of samples with a 55-nm (blue circles) and a 27-nm (orange triangles) SiGe cap are ~400,000 cm^2/Vs and ~200,000 cm^2/Vs, respectively. To identify the dominant limiting factors on mobility of 2DEGs grown in our RTCVD system, we placed theoretical model curves for the three main scattering mechanisms mentioned in Sec. 5.2 together with our data (Fig. 5.8). Several fitting parameters are chosen to optimize the fittings. The total scattering is also plotted in thick brown lines based on Eq. 5.4.

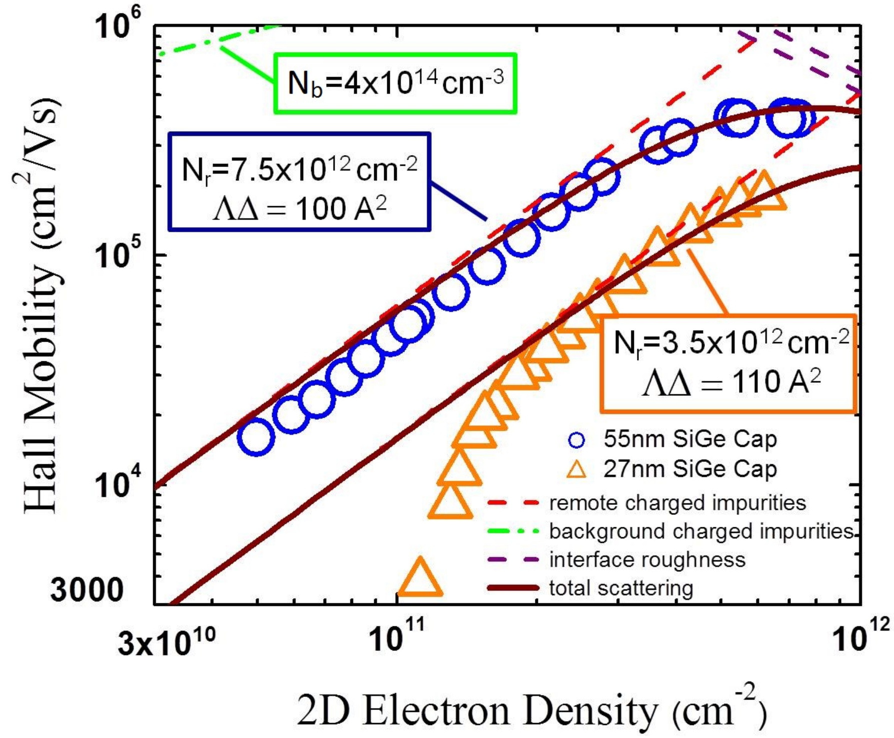

Figure 5.8: Typical Hall measurement data measured from 2DEGs grown in our RTCVD with theoretical fitting curves of three main possible mobility-limiting mechanisms.

Over a wide range of 2D electron density values, the dominant scattering mechanism was the scattering of remote charged impurities ($\sim n_{2D}^{1.5}$). The density of remote charges (N_r) chosen here are 7.5×10^{12} cm^{-2} and 3.5×10^{12} cm^{-2} for the samples with a 55-nm and a 27-nm SiGe cap respectively. Such high densities of interface charges are actually in the range of other experimental data for the interface of an aluminum oxide by ALD and silicon [74]. The scattering of background charged impurities with total impurity density, $N_b \sim 4\times10^{14}$ cm^{-3}, measured by secondary ion mass spectroscopy (SIMS), is not significant (See Sec. 5.5). In addition, at high density, interface roughness scattering may account for the saturation of the mobility. The product of the characteristic length of the interface roughness Λ and rms roughness Δ are 100 $\mathring{A}^2$ and 110 $\mathring{A}^2$ for the samples with a 55-nm and a 27-nm SiGe cap, respectively.

Except for the theoretical curve of background scattering, whose parameter, N_b, was from an experimental measurement, the fitting curves for remote scattering and interface roughness scattering were both based on optimizations of respective fitting parameters. More detailed experiments and quantitative analyses for individual scattering mechanism will be discussed in the following several sections.

5.4.2 Metal-Insulator Transition and 2D Critical Density

The importance of the 2D electron density of a 2DEG in quantum computing applications is no less than the electron mobility. As we mentioned in Sec. 5.1, a lower 2D electron density offers a wider window for the geometry design of a quantum dot, allowing a single electron to be obtained in a larger quantum dot and thus facilitating the process for sub-micron fine features. In Fig. 5.8, the lowest n_{2D} of samples with a 55-nm (circles) and a 27-nm (triangles) SiGe cap are 4.9×10^{10} cm^{-2} and 1.1×10^{11}cm^{-2} respectively, which are the record low density in the samples previously reported with comparable SiGe cap thicknesses [39, 75].

The lowest n_{2D} in a 2DEG is usually referred to critical 2D electron density, which is theoretically affected by potential fluctuations from charges at scattering sites [60, 61]. In an undoped 2DEG, the randomly distributed scattering sites at the oxide/silicon interface non-uniformly influence the potentials in the remote strained silicon channel, leaving a non-uniform conduction band minimum as shown in Fig. 5.9. If an electron density induced by gate voltage is high enough, a 2DEG conducts as a metal (Fig. 5.10a). On the other hand, below a critical electron density, a 2DEG does not conduct and act as an insulator, where electrons are localized in the valleys of potential fluctuations and can not escape them due to lack of thermal energy at liquid helium temperature (Fig. 5.10b). Therefore, the onset of the channel conduction is also called as Metal-Insulator Transition (MIT). The first measurable density point from Hall measurement is called critical 2D electron density.

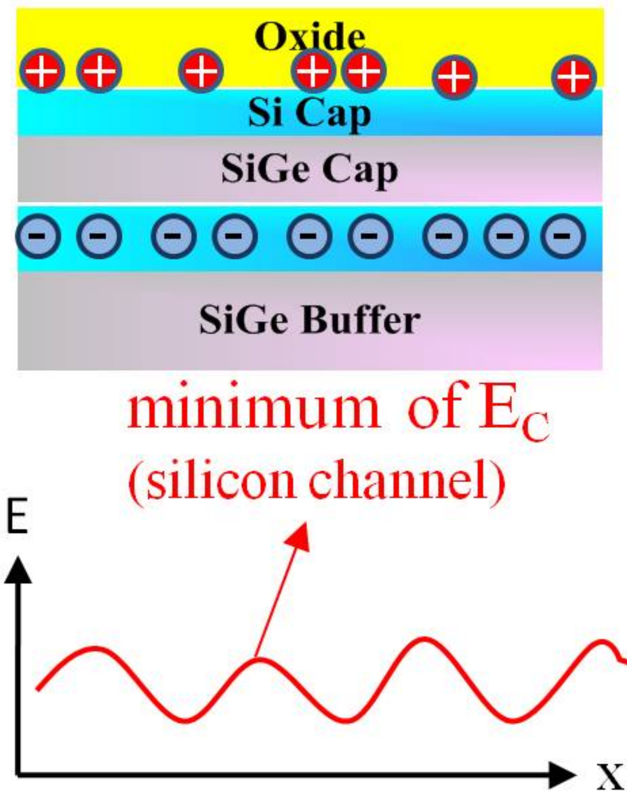

Figure 5.9: The schematic of potential fluctuation caused by remote charges at the silicon/oxide interface in an undoped 2DEG.

5.4.3 Experimental Observation of Metal-Insulator Transition

A typical metal-insulator transition can be very sharp in most of undoped 2DEGs. The channel may be turned on or off suddenly with a very small increment in gate voltage ~0.01 V. For example, for the sample with a 55-nm SiGe cap in Fig. 5.8, the channel is suddenly shut off from a fairly conducting status (mobility is >10,000 cm^2/Vs despite the density as low as 4.9×10^{10} cm^{-2}) to full insulation with only a 0.01 V gate voltage difference. However, instead of this sharp shut-off, a nonlinear decrease of μ was observed in the sample with a 27-nm SiGe cap in the low density regime [76] (Fig. 5.8). Similar behavior, a nonlinear drop in mobility in the low density regime,

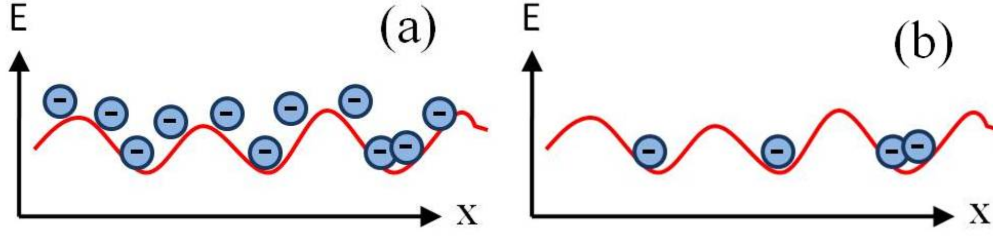

Figure 5.10: (a) A 2DEG conducts as a metal in the channel when the electron density is high (b) A 2DEG acts as an insulator because electrons are localized in the valleys of fluctuations when the electron density is too low.

was also reported in doped 2DEGs in the GaAs/AlGaAs material system [68]. This drop is possibly described by a metal-insulation-transition (MIT) model, assuming the sources of fluctuations are charged impurities at the aluminum oxide/Si interface (Fig. 5.11). The model used here includes a parameter A [77]:

$$A = \frac{N_r}{16\pi {n_{2D}}^2 s^2}, \; if \; 4k_F s >> 1 \tag{5.5}$$

where s is the SiGe cap thickness, N_r is the 2D density of remote charged impurities and k_F is the Fermi wavenumber. Therefore, the mobility limited by the scattering of remote charged impurities can be modified as

$$\mu_{rs}(n_{2D}) = \mu_{rs0}(n_{2D})(1 - A) \tag{5.6}$$

In the high density regime, A is much smaller than 1, meaning that μ_{rs} is close to μ_{rs0}. The mobility is not degraded because the electron density is high enough to screen the influence of potential fluctuations from remote charged impurities. However, once 2D density decreases (given a fixed N_{r} and s) and the parameter A approaches 1, μ_{rs} decreases sharply. The original model of the scattering from remote charged impurities is no longer applicable. When A is 1, the mobility drops to zero, and the metal-insulator transition occurs.

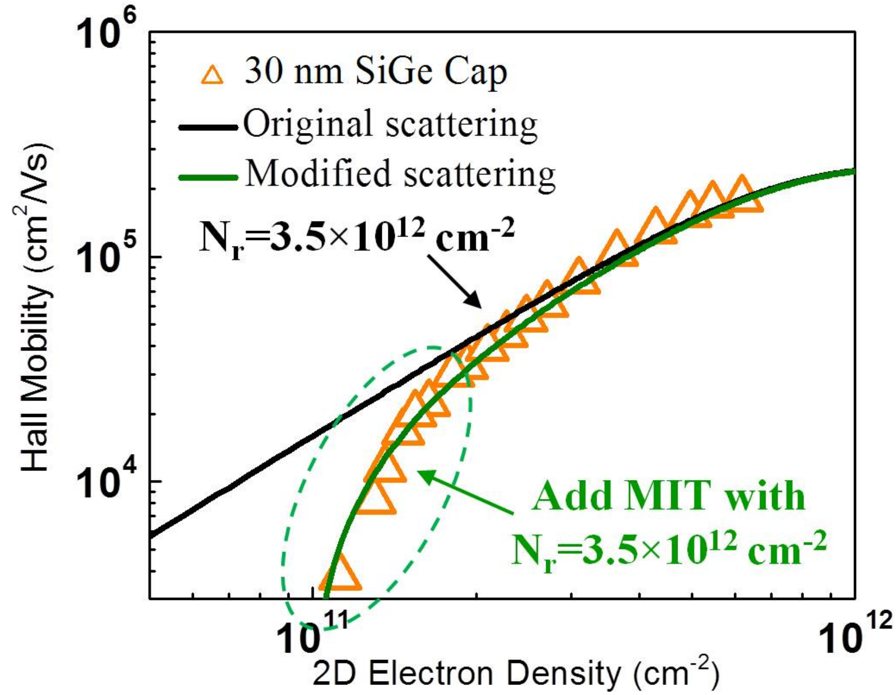

Figure 5.11: The modified mobility model by a MIT model (green curve) fit the data of the sample with a 27-nm SiGe cap, especially in the low density regime.

5.4.4 Failure of the MIT Model

The sharp decrease of μ in the sample with a 27-nm SiGe cap is well fitted by the MIT model, which indicates that the remote charged impurities at the aluminum oxide/silicon interface have a strong influence on the sample with such a thin cap layer. However, no similar phenomenon was observed in the sample with a 55-nm SiGe cap (Fig. 5.8). A trial to apply the MIT model mentioned in the previous subsection on this sample showed a great discrepancy in data and the modified mobility curve (green line in Fig. 5.12). The disagreement in data and the modified mobility model by the MIT model could be discussed from several aspects. First, the extracted density of remote charged impurities (N_r) based on the theoretical equation (Eq. 5.2) may not be accurate. For example, if the mobility curve shown here is limited by a certain

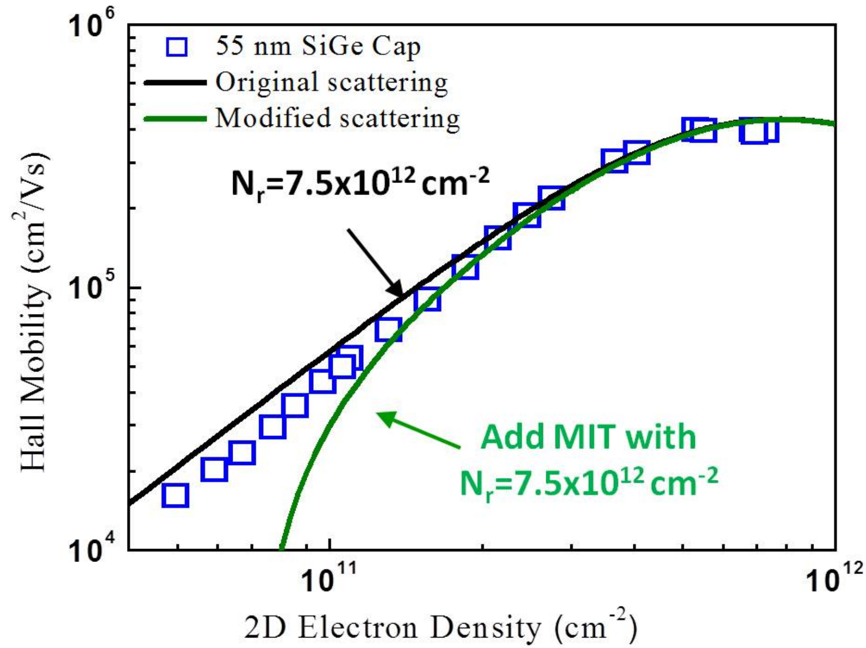

Figure 5.12: A discrepancy between data points of the sample with a 55-nm SiGe cap and the modified model by the MIT model. The modified mobility model is the green line, while the original model is in black.

unknown mechanism, not simply by remote scattering (despite that the slope of data is very close to 1.5), the extracted N_r (7.5×10^{12} cm^{-2}) is then doubtful. Second, it could be arbitrary to equate the density of remote charged impurities causing remote scattering that limits mobility to the one that results in potential fluctuation described in this MIT model. Moreover, we could not rule out the possibility that the theory of remote charge scattering is not perfect and complete for Si/SiGe 2DEGs as well as the MIT model. The primary foundations of both theories are still theoretical calculations and experimental data from GaAs/AlGaAs 2DEGs. Imperfection in crystal structures of SiGe alloys and strained silicon could easily raise the uncertainty and complexity in theoretical predictions.

5.5 Background Scattering Alleviation

5.5.1 High Background Impurity Level in Old Samples

We discussed how the scattering from background charged impurities limits the electron mobility of a 2DEG in Sec. 5.2.1. The density of background charged impurities is critical to determine where the mobility level would be expected if background scattering is dominant in a system. In our RTCVD system, extremely high doses of dopants, such as boron or phosphorus, have been used for decades. Remnant dopant atoms could attach along the inner walls of gas pipes, quartz reactor tubes or even quartz wafer holders. Once a newly-loaded wafer is baked at high temperature for cleaning, those buried atoms may evaporate out and incorporate into the newly-grown epitaxial layers, leading to a high background concentration of unexpected dopants. For example, a SIMS analysis clearly showed very high background concentration of both phosphorus ($>2\times10^{17}$ cm^{-3}) and boron ($>1\times10^{16}$ cm^{-3}) in an undoped 2DEG grown in our RTCVD system in the year 2010 (Fig. 5.13). If we put $N_b = 1\times10^{17}$ cm^{-3} into Eq. 5.1 with an electron density in a range of 10^{11} cm^{-2} to 10^{12} cm^{-2}, the predicted mobility is as low as 10,000 cm^2/Vs, which is about the same level as our old experimental data.

5.5.2 Efforts to Alleviate Background Scattering

To figure out a way to reduce the density of background charged impurities, the first step is to identify where those undesired dopant atoms exactly come from. A simple way is to load a new quartz wafer stand or replace the old quartz reactor tube with a brand new one, and grow a test structure for a SIMS analysis. Unfortunately, SIMS showed very high background doping levels in all the grown layers, especially phosphorus, given the source gases were expected to have very low impurity background levels. Thus it was concluded that those dopant atoms came into the reactor

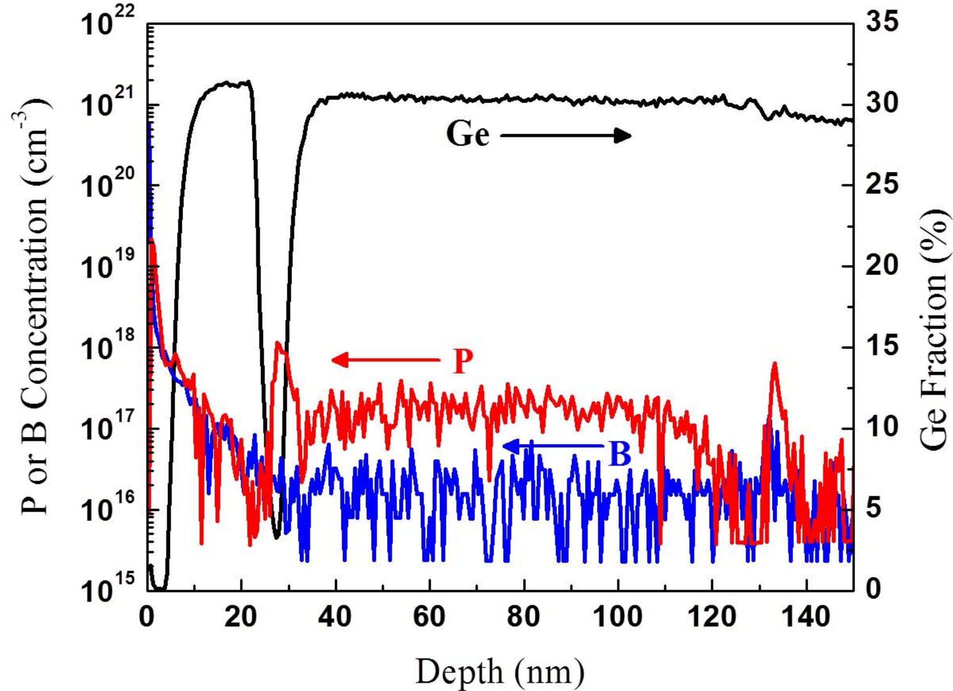

Figure 5.13: The SIMS profile of a typical undoped 2DEG grown in our RTCVD before a new gas supply system was introduced. Clear high concentrations of both phosphorus and boron were observed.

along with gases from pre-existing contamination in the old gas supply pipes, where the precursor of phosphorus, phosphine (PH_3), had been mixed with other precursor gases and hydrogen for decades.

To avoid phosphorus atoms from mixing into other process gases again, a new gas supply assembly was designed and a new gas supply panel was introduced in collaboration with Jiun-Yun Li as shown in Fig. 5.14. The pipe length from the new gas supply panel to reactor is about 5 meters long. We separated other process gases from phosphine so that they are sent to the gas supply assembly by two different pipes. In addition, the venting paths to process pumps were also separated. Based on this design, phosphine is only mixed with other process gases in the gas supply assembly, which is located at only a small distance (~50 cm) to the entry of the

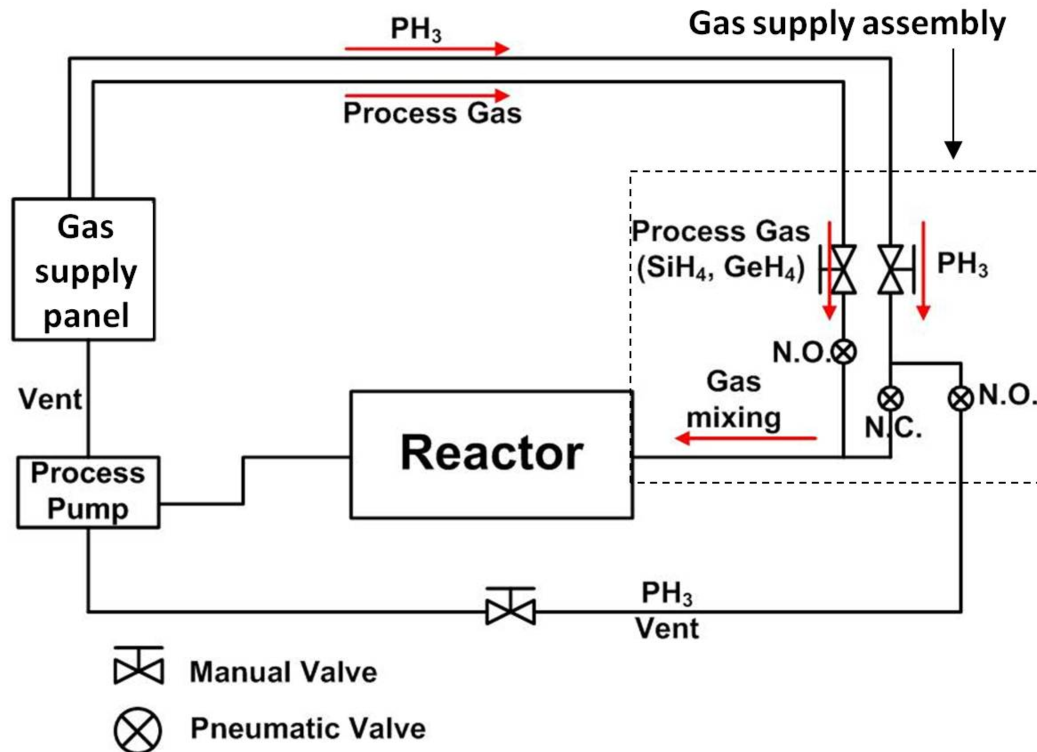

Figure 5.14: The schematic of the new gas supply panel and the gas supply assembly. Phosphine is separately transported from other process gases until a half meter away from the reactor entry to avoid mixture and contamination.

reactor, when the inject valve of phosphine is on. Plus, the gas supply assembly is replaceable, if a high phosphorus level reappears in grown layers.

An undoped silicon 2DEG sample was grown with the new gas supply panel and the gas supply assembly, and was sent to Evans Analysis Group (EAG) for high precision SIMS analysis for phosphorus and boron (Fig. 5.15). We noted that the Ge profile here is only for reference and is not precise because the measurements were specifically optimized for phsophorus or boron. Except for high concentrations at the surface caused by the typical surface effect of a SIMS measurement, phosphorus level plummeted to 1×10^{14} cm^{-3} while boron level was reduced to 5×10^{13} cm^{-3}, both hitting the detection limit and at least getting 1000 times lower than those levels observed in samples grown by the old gas panel. The predicted mobility by such low

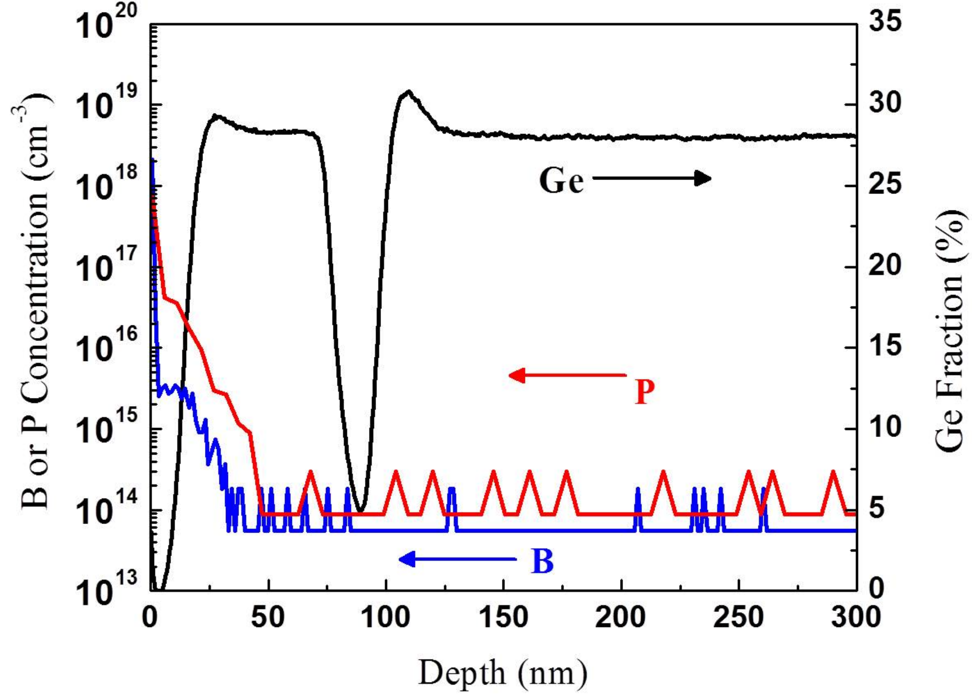

Figure 5.15: Extremely low concentrations of both phosphorus and boron in grown layers after a new gas panel and a gas supply assembly were installed. Both doping levels hit the detection limits of the high-precision SIMS analysis.

densities of background charged impurities by Eq. 5.1 is over 10,000,000 cm^2/Vs as the electron density is in the range of 10^{11} cm^{-2}. Such a high value is much higher than the mobility we measured over the whole range of 2D electron density, implying that the background scattering has become negligible in our system.

5.6 Effects of Remote Scattering

5.6.1 Effects of SiGe Cap Thickness

The scattering from remote charged impurities at the oxide/silicon interface in an undoped silicon 2DEG undoubtedly becomes the major mobility-limiting factor, when the background scattering is alleviated by reducing background doping concentra-

tions. The slope of mobility data in log-log scale in Fig. 5.8 are clearly close to 1.5, which is the theoretical characteristic of the remote scattering. With proper fitting parameters (density of remote charged impurity), the model curve fit a wide range of data (Fig. 5.8). However, the independent measurement of the exact density of interface charged impurities was difficutlt. Due to the complexity of multiple Si/SiGe heterostructure layers underneath the oxide, plus the limitations of C-V measurements at liquid helium temperature, no meaningful C-V data were obtained yet to allow us to quantitatively discuss the remote charge density and resulting remote scattering.

Nevertheless, a hint from experimental data still strongly supports our argument that remote scattering really plays a crucial role in our samples. A series of Hall measurement data from samples with various SiGe cap thicknesses (14, 20, 40, 80, 120, and 180 nm) were plotted together for comparison in Fig. 5.16. Note that all other growth and process recipes for this batch of samples remained the same. The highest mobility and lowest n_{2D} (critical density) for each sample versus SiGe cap thickness are shown in Fig. 5.17.

A trend that the mobility curves moved upwards and leftwards with thicker SiGe cap thickness is clearly observed, at least for samples with cap layer <80 nm. For example, the highest mobility of the 14-nm cap sample is about 40,000 cm^2/Vs, while that of the 80-nm cap sample is 380,000 cm^2/Vs, almost 10 times higher than the thinnest sample. Given the surface condition of as-grown wafers, surface cleaning processes and aluminum oxide deposition were controlled in the same conditions, we concluded that the improvement in mobility curves are mainly due to the increase in SiGe cap thickness. Physically, a longer distance between the charged impurities and the silicon channel mitigates Coulomb forces from the interface to the 2DEG, lifting the mobility limitation upwards. Therefore, it is straightforward to think that an extremely high mobility is possible if we continue to increase the thickness of SiGe

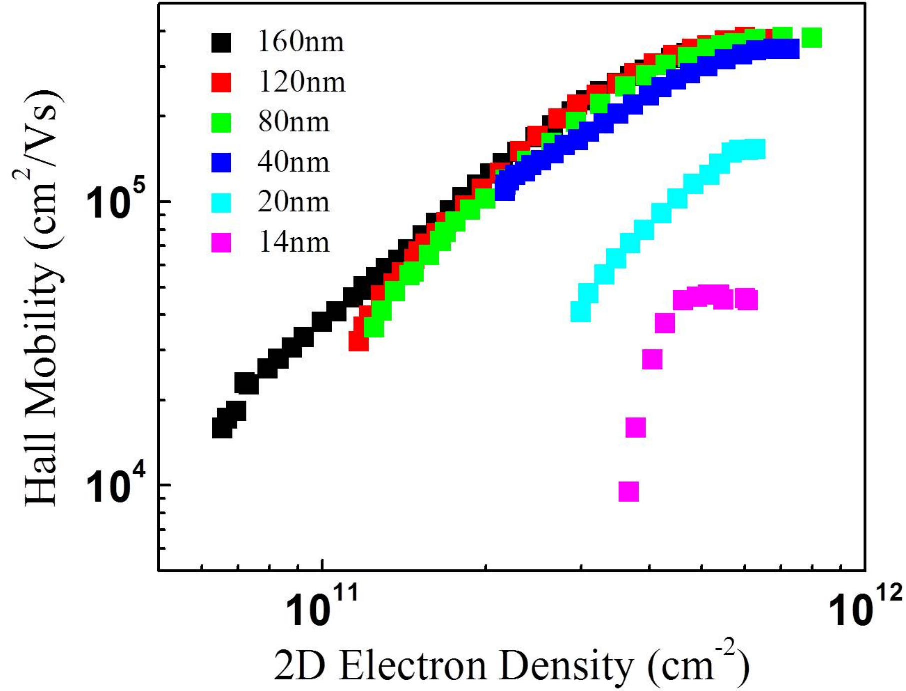

Figure 5.16: Mobility curves from samples with various SiGe cap thicknesses. Mobility is enhanced with a thicker SiGe cap, but saturate at 400,000 cm^2/Vs.

cap and bury the silicon channel as deep as possible. Such thinking was substantiated by the recent low-temperature mobility record of Si/SiGe undoped 2DEGs (about 2,000,000 cm^2/Vs [78]), which was measured from a sample with a 500+ nm thick SiGe cap layer. However, we noticed that there seems to be an unknown factor that limits the highest low-temperature mobility in our samples at around 400,000 cm^2/Vs (Fig. 5.16), regardless of thicker SiGe cap layers (>80 nm). More experiments and trials to figure out the limitations will be discussed in the following sections.

We also note that the critical density gets lower with thicker SiGe cap layers (Fig. 5.17). The possible explanation is that the potential fluctuation in the conduction band minimum of the strained silicon channel, caused by Coulomb forces from remote charged impurities at interface, is reduced by increasing the distance between the interface and the channel. Thus the localization of electrons induced in the chan-

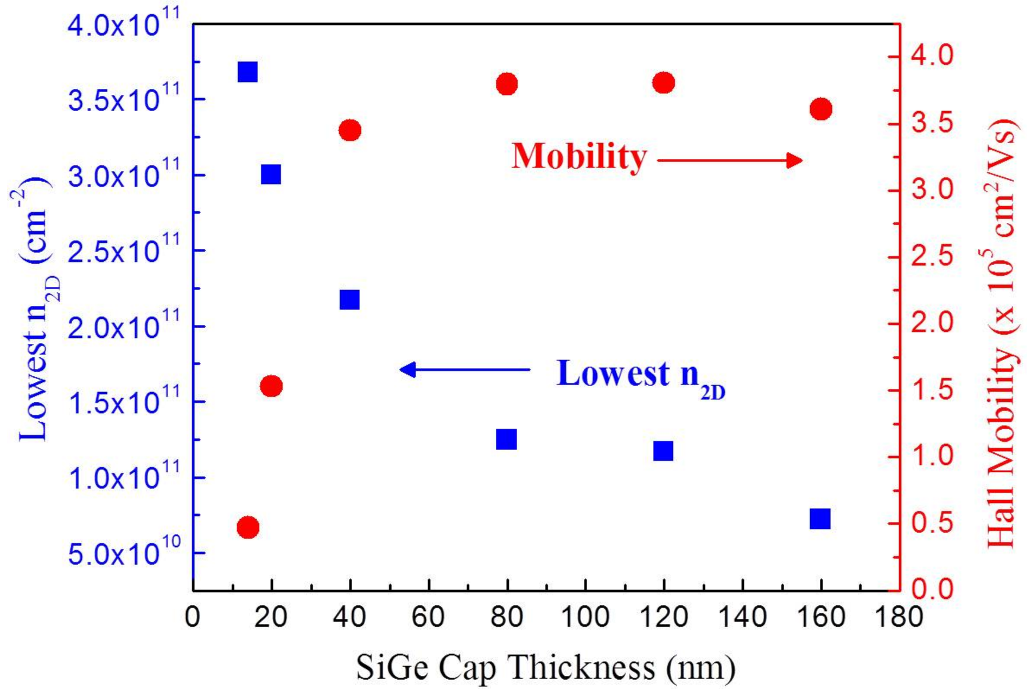

Figure 5.17: The highest mobility and lowest 2D electron density extracted from samples with various SiGe cap layers. The critical density gets lower in the sample with thicker SiGe cap thickness due to weaker potential fluctuations.

nel is less severe than the case with a thinner SiGe cap layer (or a shallower 2DEG), allowing a 2DEG to conduct at relatively low density regime.

5.6.2 Treatments on Oxide/Semiconductor Interface

The quality of the interface between oxide and silicon becomes crucial to electron transport properties of our undoped 2DEG samples because the most dominant mobility-limiting mechanisms, remote scattering, is caused by the density of interface charged impurities (Eq. 5.2). The interface between silicon and thermally grown SiO_2 is well known for its ultra-low interface charge densities. However, the deposition temperature for a high quality thermally grown SiO_2 can be very high (>1000 °C). Ge and Si may inter-diffuse across the Si/SiGe interface when the process temperature

is higher than 850 °C [51]. This inter-diffusion could deteriorate the abruptness of strained silicon quantum well and degrade the 2DEG qualities, through alloy scattering, for example. We thus used atomic layer deposition (ALD) to deposition aluminum oxide (ALO) at 300° for our gate insulators. Aluminum oxide deposited by ALD has been proven to have a good interface quality with bare bulk silicon [79, 80, 81, 82]. Great conformity and its low deposition temperature (<300°C) make aluminum oxide deposited by ALD a popular insulator on a Si/SiGe 2DEG.

In the literature [83, 84], the common operation temperature of thermal ALD for aluminum oxide (In contrast to plasma-enhanced ALD) varies from 150 °C to 300 °C. The ALD system in our university cleanroom is the Cambridge NanoTech Savannah 100, and its maximum deposition temperature is 300 °C. To examine the deposition temperature effects on the interface quality, and then the 2DEG quality, three temperatures (300 °C, 225 °C and 150 °C) were chosen for a 90-nm aluminum oxide deposited on three separate samples grown in the same growth run (Same SiGe cap thickness). After Hall-bar-shaped metal gate was evaporated on these three devices, Hall measurements were then conducted and mobility curves were plotted in Fig. 5.18 for comparison.

Here we repeat that 300 °C is our standard deposition temperature for most of the 2DEG samples shown in this thesis. The data from the sample with 225 °C ALO (red) showed pretty high electron mobility, but no obvious improvement in both mobility and critical density were observed. In fact, its mobility is even lower than the reference sample (black). Furthermore, a gate leakage even interrupted the measurement on the sample with 150 °C ALO, implying the worse quality of ALO by low temperature deposition in our ALD equipment.

Another common measure to improve interface quality is annealing. Four devices were made on the same sample and processed together until the completion of ALO deposition at 300 °C. Three of these devices were then separately annealed at 450

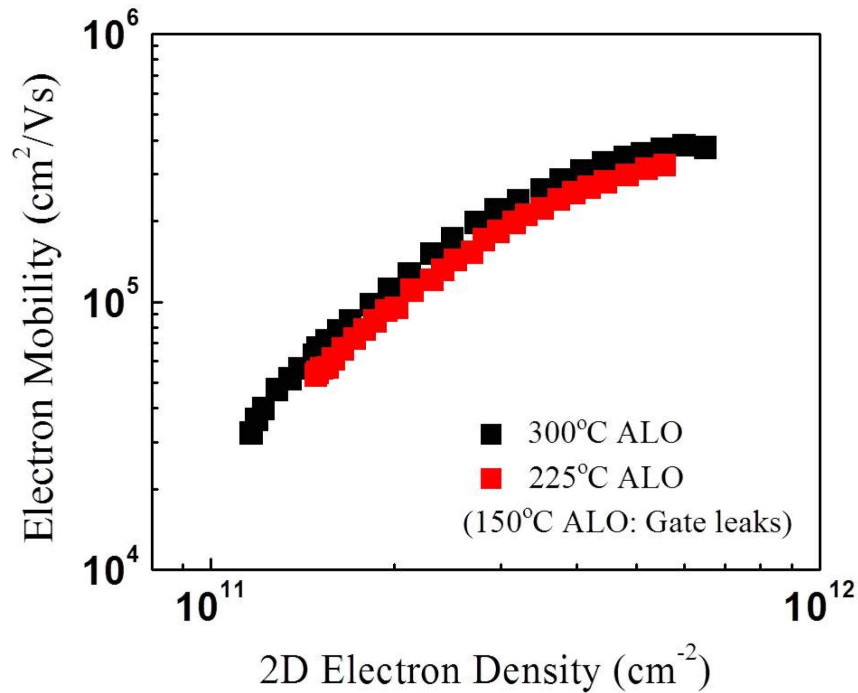

Figure 5.18: Mobility curves measured from samples with an aluminum oxide deposited at three different temperatures: 150 °C, 225 °C and 300 °C

°C, 600 °C and 750 °C in a forming gas environment in RTA AG for 50-100 seconds. However, the following Hall measurements conveyed an inconclusive result (Fig. 5.19). Although annealing at 750 °C (blue) and 450 °C (pink) slightly lifted up respective mobility curves, annealing at 600 °C (green) somehow degraded its 2DEG quality where its mobility is much lower than the reference data (black). Moreover, a huge shift (a volt to couple of volts) in threshold voltages of annealed samples from that of the reference sample may infer the post-ALD annealing induces charge trapping (positive or negative) at the interface (Fig. 5.20). We note that both the minimum density and the threshold voltage do not correlate with high mobility. Thus our fundamental understanding of the interface quality effect on transport properties is not clear.

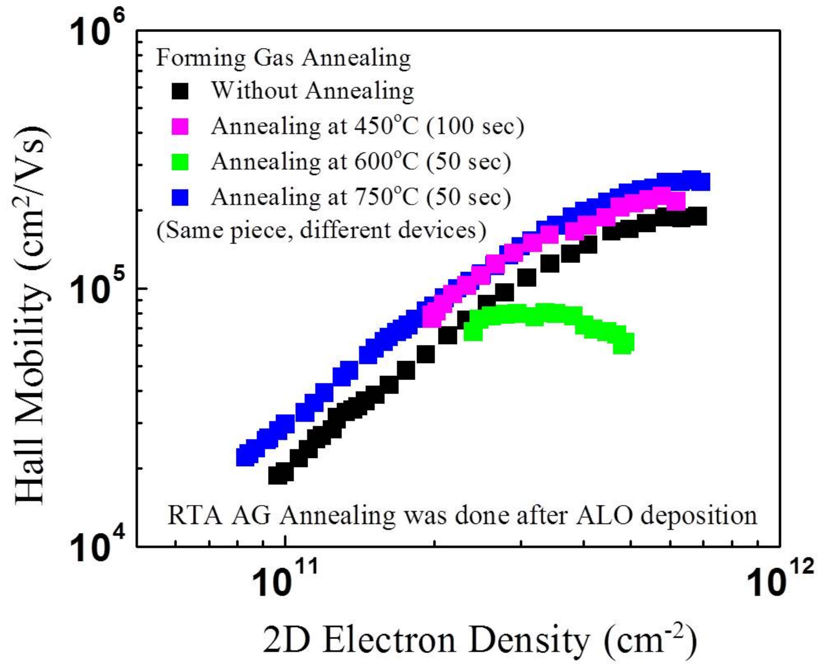

Figure 5.19: Mobility curves from samples annealed at different temperatures (450 °C, 600 °C and 750 °C) after ALO deposition.

5.6.3 Remote Scattering from the Regrowth Interface

The above discussions were mainly focused on the influence of remote scattering from the oxide/silicon interface, but we ignored the bottom interface (regrowth interface) where our growth started. We mentioned in Ch. 2 that both our doped or undoped strained silicon 2DEGs were all grown on top of commercial relaxed SiGe buffers from Amberwave System Inc.. A considerable amount of charged impurities or defects may exist at this regrowth interface. Hence, the remote scattering from this interface may also be taken into account while we try to determine the hidden mobility-limiting factors. Because the work relevant to remote scattering from the regrowth interface depends on a newly-discovered surface screening effect, more details about the bottom interfaces will be discussed later in Ch. 7.

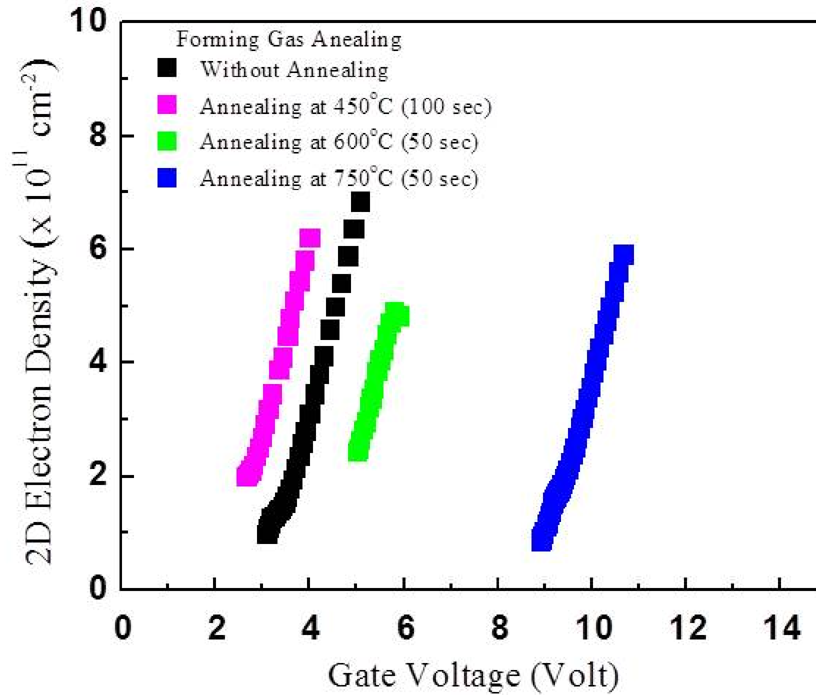

Figure 5.20: The shifts in threshold voltages imply that charges are trapped at the interface after annealing.

5.7 Effects of Growth Temperature

5.7.1 Effects of Growth Temperature

The growth temperature for the SiGe cap layer is usually constrained to lower than 550 °C to suppress the surface segregation of phosphorus atoms from the electron supply layer in a typical doped 2DEG [40]. Despite no intentionally doped layer, growth temperature for an undoped 2DEG is still kept as low as possible to avoid undesired strain relaxation in the strained silicon layers. So as shown in Ch. 2, the standard growth temperatures for our undoped 2DEGs are 575 °C for SiGe and 625 °C for Si. Nevertheless, it is interesting to see how much the growth temperature affects the stability of the strained silicon layer and of the Si/SiGe interfaces, and then how these variables subsequently affect the transport properties of 2DEGs.

Here we show a set of Hall measurement data from samples with different growth temperatures for their strained silicon cap and strained silicon quantum well (channel) in Fig. 5.21. For this batch of samples, the thickness of each layer was grown as consistent as possible to avoid any perturbation on mobility curves due to distinct layer structures: 3-4 nm for strained silicon cap, 65-80 nm for SiGe cap, 9-12 nm for strained silicon quantum well and 145-160 nm for SiGe buffer layer. The growth temperature for all relaxed SiGe layers was fixed at 575 °C, while the growth temperatures for strained silicon varied. The actual growth temperatures were labeled in the parentheses with the temperature for the silicon cap ($T_{Si,Cap}$) first, and that for the silicon quantum well or silicon channel ($T_{Si,QW}$) second. The results in Fig. 5.21 are quite inconclusive at first glance, but a sure thing is that a growth temperature for strained silicon layers lower than 625 °C is a necessity to achieve a good mobility curve (highest mobility >200,000 cm^2/Vs). Furthermore, we will show that the change in growth temperatures for strained silicon layers actually did influence both Si/SiGe interface roughness, interlayer mixing (at the top of the strained Si channel) and the density of threading dislocations.

5.7.2 Surface Roughness versus Interface Roughness

Not much literature has focused on Si/SiGe interface roughness scattering in both doped and undoped 2DEGs [85, 86]. The difficulty in the measurement of actual Si and SiGe interface roughness in-situ is one of reasons that has prevented relevant research. Another important reasons for the lack of data in literature is that there is no effective measure to vary the interface roughness in different 2DEGs without significant modification of layer structures. Ismail et al. [28] observed a drop in mobility for a sample with a strained silicon layer which is much thinner than the critical thickness. They attributed that drop in mobility to the roughness between Si and SiGe, but no further experimental data supported this argument. However, by

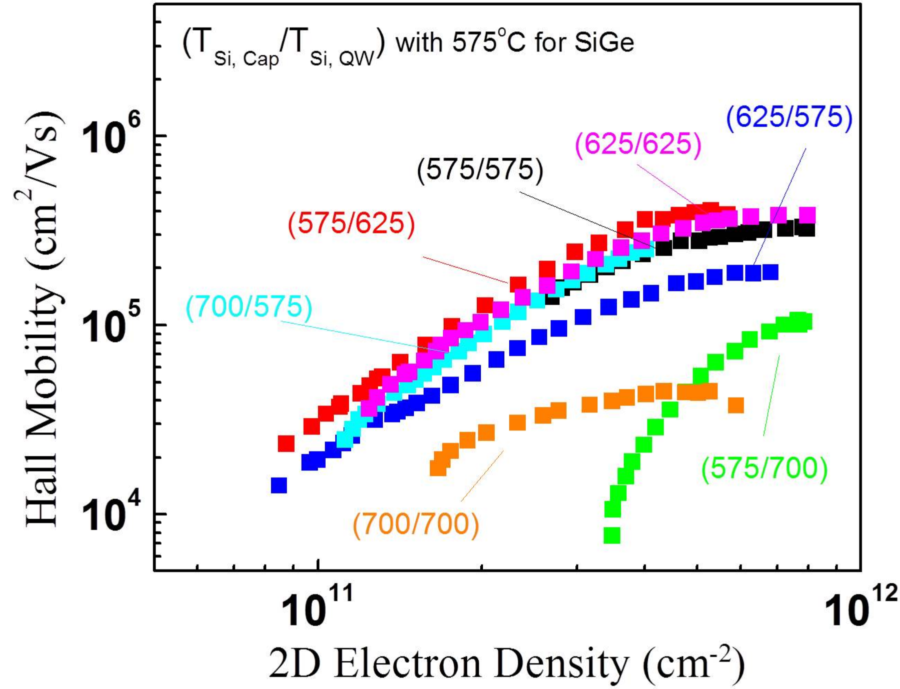

Figure 5.21: Mobility curves from samples whose strained silicon layers were grown at different temperatures.

means of changing growth temperature, it could become possible to vary the interface roughness without changing the layer structure too much, which may enable us to analyze the effect from interface roughness scattering solely without other scattering mechanisms mingling in.

Since we don′t have in-situ tools in our growth reactor for the roughness measurement, we measured the surface roughness on as-grown 2DEG samples whose strained silicon layers were grown at different temperatures. An AFM result was shown in Fig. 5.22 as an example, and its RMS surface roughness calculated by software, NanoScope Analysis, is 0.229 nm (left figure in Fig. 5.22). A reference sample was also grown in the same temperatures for both the strained silicon and the SiGe buffer layer as the sample shown in Fig. 5.22, but the growth was stopped at the strained silicon channel to expose its surface for roughness measurement. An even

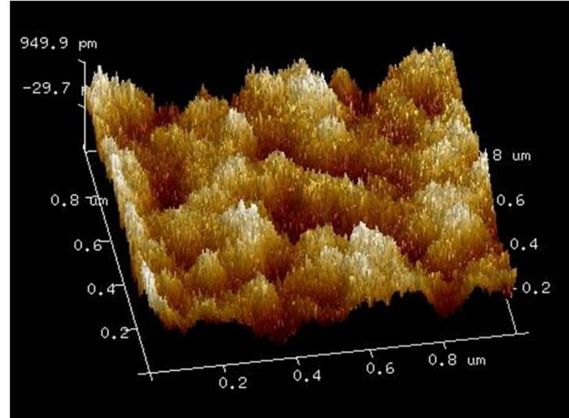

Figure 5.22: An AFM image and its calculated RMS roughness on a complete undoped silicon 2DEG.

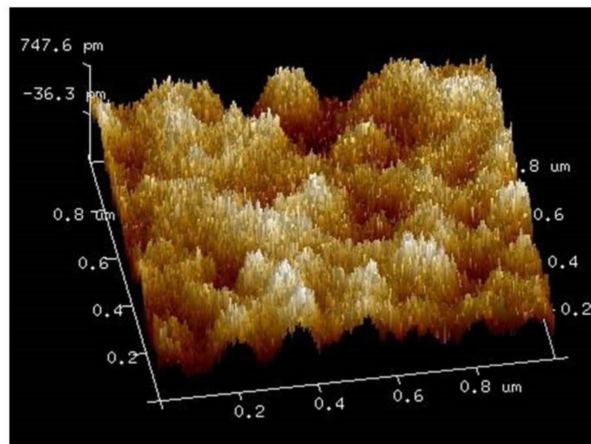

Figure 5.23: An AFM image and its calculated RMS roughness from a reference sample whose layer structure only consists of the relaxed SiGe buffer and the strained silicon QW (channel).

smoother surface with RMS roughness ~ 0.180 nm was obtained from this reference sample (Fig. 5.23), which ensures us that the surface roughness we measured from a complete undoped 2DEG could be viewed as the worst case for its interface roughness under each temperature condition.

5.7.3 Effects of Si/SiGe Interface Roughness

We labeled the RMS roughness adjacent to the mobility curves from individual samples with unique growth temperatures (Fig. 5.24). The sample with both strained silicon layers grown at 700 °C (orange), around 100 °C higher than the standard growth temperature, has the roughest surface at an RMS of 0.543 nm. Its low mobility in the high density regime could be a hint that interface roughness scattering limits its mobility based on Eq. 5.3. In contrast with it, another sample with both strained silicon layers grown at 575 °C, the lowest temperature we tried here, shows an extremely smooth surface with roughness ~ 0.111 nm and high mobility in the high density regime. However, for the rest of the samples, the surface roughness data does not show a strong correlation with the growth temperatures. Nevertheless, an implication from this set of data is still useful: if high mobility is desired, the growth temperature should be at 625 °C or less.

The different growth temperatures for strained silicon layers lead to the variation of interface roughness in 2DEGs. Compared with growth temperatures, it is more interesting to see if there is any effect of interface roughness on both electron mobility and critical density. The highest mobility and lowest 2D density were then extracted from these samples and plotted with measured roughness from this sample set (Fig. 5.25). The lowest 2D density has no obvious correlation with the roughness, while the highest mobility has a subtle inverse proportion to the surface roughness data, as indicated by the red solid line. This observation basically agrees with the theoretical prediction as discussed in Sec. 5.2.3 and Sec. 5.4.1: Interface roughness scattering influences electron mobility more at high density regime and has negligible effect at low density regime.

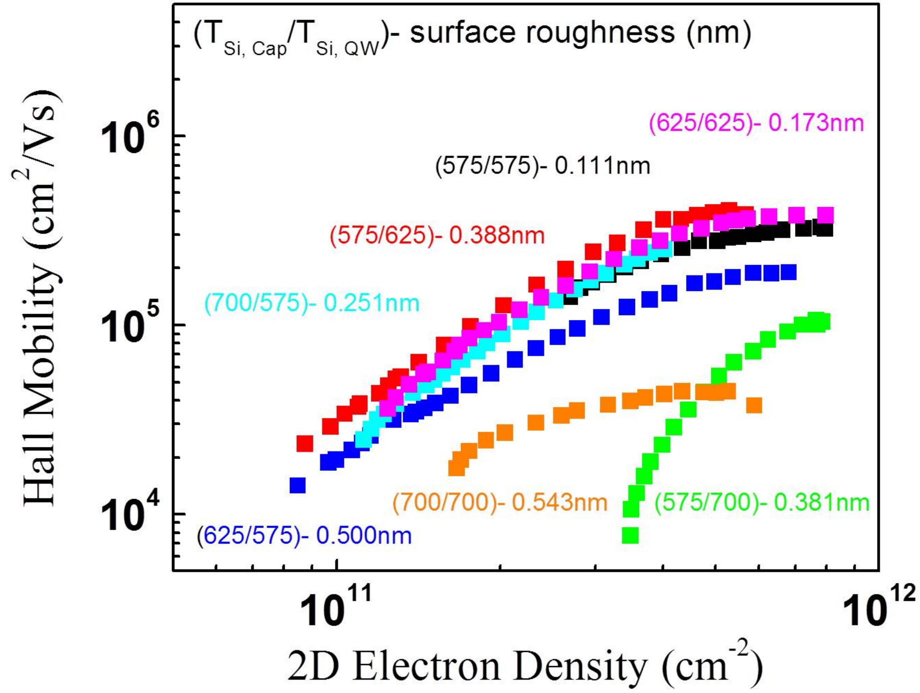

Figure 5.24: Mobility curves labeled by individual growth temperature and its RMS surface roughness.

5.7.4 Effects of Si/SiGe Interlayer Mixing

The SiGe cap layer after the Si channel was grown at a lower temperature (575 °C) than the silicon channel and the silicon cap. Thus the interlayer mixing, which may result in alloy scattering, could only occur during the silicon cap growth. We observed the sample with the silicon channel grown at 700 °C and the silicon cap grown at 575 °C has a poor transport property (green symbols in Fig. 5.24). However, the sample with the silicon channel grown at 575 °C and the silicon cap grown at 700 °C has a good mobility curve (blue symbols) just like other samples with cap layers grown at lower temperatures. Therefore, we can rule out the interlayer mixing and possible alloy scattering in our undoped 2DEGs.

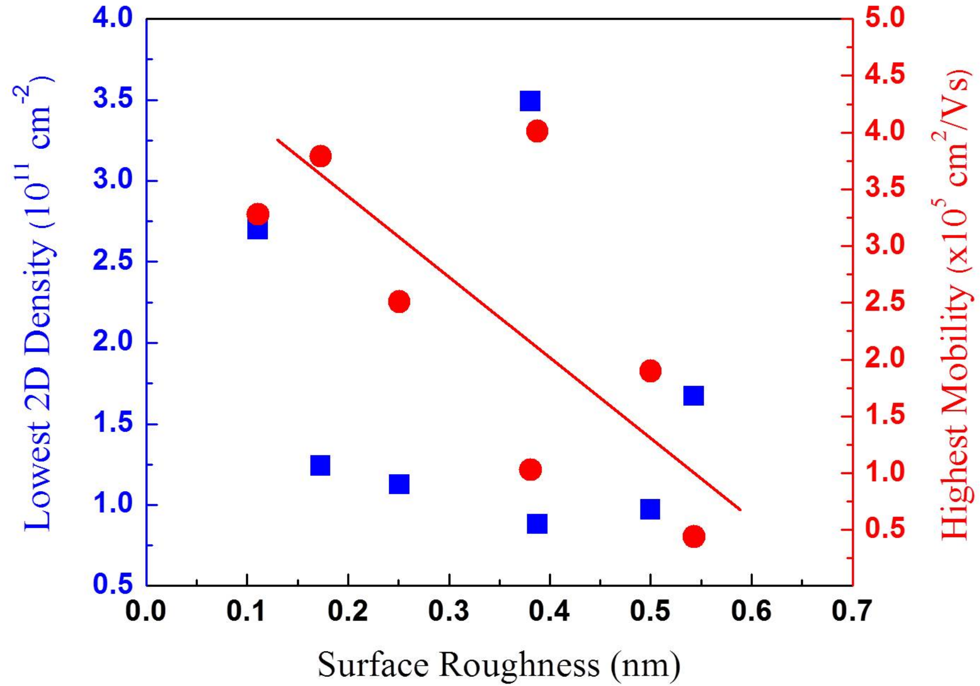

Figure 5.25: Extracted highest mobility and lowest 2D density versus surface roughness.

5.8 Effects of Threading Dislocations

Another possible mobility-limiting mechanism hidden in a Si 2DEG is scattering from threading dislocations. Unlike GaAs/AlGaAs material system, Si and SiGe have severer lattice mismatch (4%), which results in inherently inevitable defects existing in a Si/SiGe heterostructure. For example, a threading dislocation could occur at 60° to the growth surface in a relaxed SiGe layer during the epitaxy, and slide along the interface between the relaxed SiGe and the strained silicon layer on the top of it to relieve accumulated strain (misfit dislocation) [73, 87, 88]. Therefore, the density of threading dislocation and the length of misfit dislocation across the strained silicon channel may bring in an adverse effect on the electron transport properties of silicon 2DEGs.

5.8.1 Defect Etching

Preferential etching is a common technique used to reveal defects in a silicon-based material system. The difference in etching rate between defects and other areas leads to etch pits that could be observed at defect locations. By counting the number of black etch pits in a microscopic image, an etch pit density could be estimated, which is usually referred to the density of threading dislocations in a Si/SiGe heterostructure.

Chromium-ion-containing etching solutions, such as Secco [89] and Schimmel [90] are the most popular etching solutions used for defect revelations. Secco consists of $K_2Cr_2O_7$ and HF, while Schimmel is a mixture of CrO_3 and HF, both diluted in DI water. The chromium-ion-containing acid is responsible for oxidizing surface silicon or SiGe, and HF etches the resulting oxides immediately. The etching rate depends on the concentration of etching solutions. For instance, more diluted solutions have slower etching rate through silicon or SiGe layers, making it easier to control the desired etch depth. To observe threading dislocations produced in the layers grown in our system, the target etching depth could not be thicker than the total thickness of layers on top of regrowth interface, which is typical ~ 250 nm. However, both Secco and Schimmel were designed to etch bulk silicon, not thin epitaxial layers. In spite of being diluted by DI water, the slowest etching rate that is controllable is still as fast as 1 μm per minute. A modified Schimmel solution [91] was proposed to aim at the defect delineation in thin SiGe epitaxial layers whose thickness ranges from tens to hundreds of nanometers. This modified etching solution consists of 55 %vol CrO_3 (0.4M) and 45 %vol HF (49%), and the solution is cooled down to + 2 °C (Ice bath). The proposed etching rate depends on the Ge fraction, but basically falls in the range of 5-15 nm/sec. The etching rate for the sample with 30% Ge fraction proposed by this paper [91], 8 nm/sec, was also verified in our lab. This etching rate is slow enough for us to control our etching depth within 250 nm easily.

We dipped our 2DEG samples grown with different temperatures into modified Schimmel solutions for 25 seconds. The total thickness etched away is about 200 nm, and the etching stopped in the middle of the grown SiGe buffer layers as desired. Etched samples were then examined under Nomarski microscope (differential interference contrast) and images were taken for the following etch pits counting. The density of etch pits observed by eye could vary a lot. For example, the image shown in Fig. 5.26a was from the sample whose surface silicon and buried silicon channel were grown at 575 °C and 700 °C respectively. The dot-like threading dislocations are randomly distributed all over the image with line-shaped misfit dislocations. On the contrary, the image shown in Fig. 5.26b from the sample, whose silicon layers were grown at 625 °C, shows much fewer etch pits, and no line-shaped misfit dislocations were spotted.

5.8.2 Effects of Threading Dislocations on Transport Properties

The etch pit density (EPD) for each sample was statistically counted from several randomly chosen 200 μm^2 windows and plotted with its corresponding growth temperature with an error bar (Fig. 5.27). Note that we only counted etch pits for the estimation of threading dislocation density. The misfit dislocations observed in Fig. 5.26a were not included in the discussion. Samples that were involved in 700 °C growth, no matter whether for the surface silicon or for the buried silicon quantum well, clearly showed 4-5 times higher EPDs (7-10$\times 10^4$ cm^{-2}) than samples grown at lower temperature (2$\times 10^4$ cm^{-2}). This strongly implies that high temperature growth induces more threading dislocation defects propagating upwards through the whole grown layers.

An interesting question may arise when these relatively high densities of threading dislocations in some samples were observed: Do those threading dislocations affect

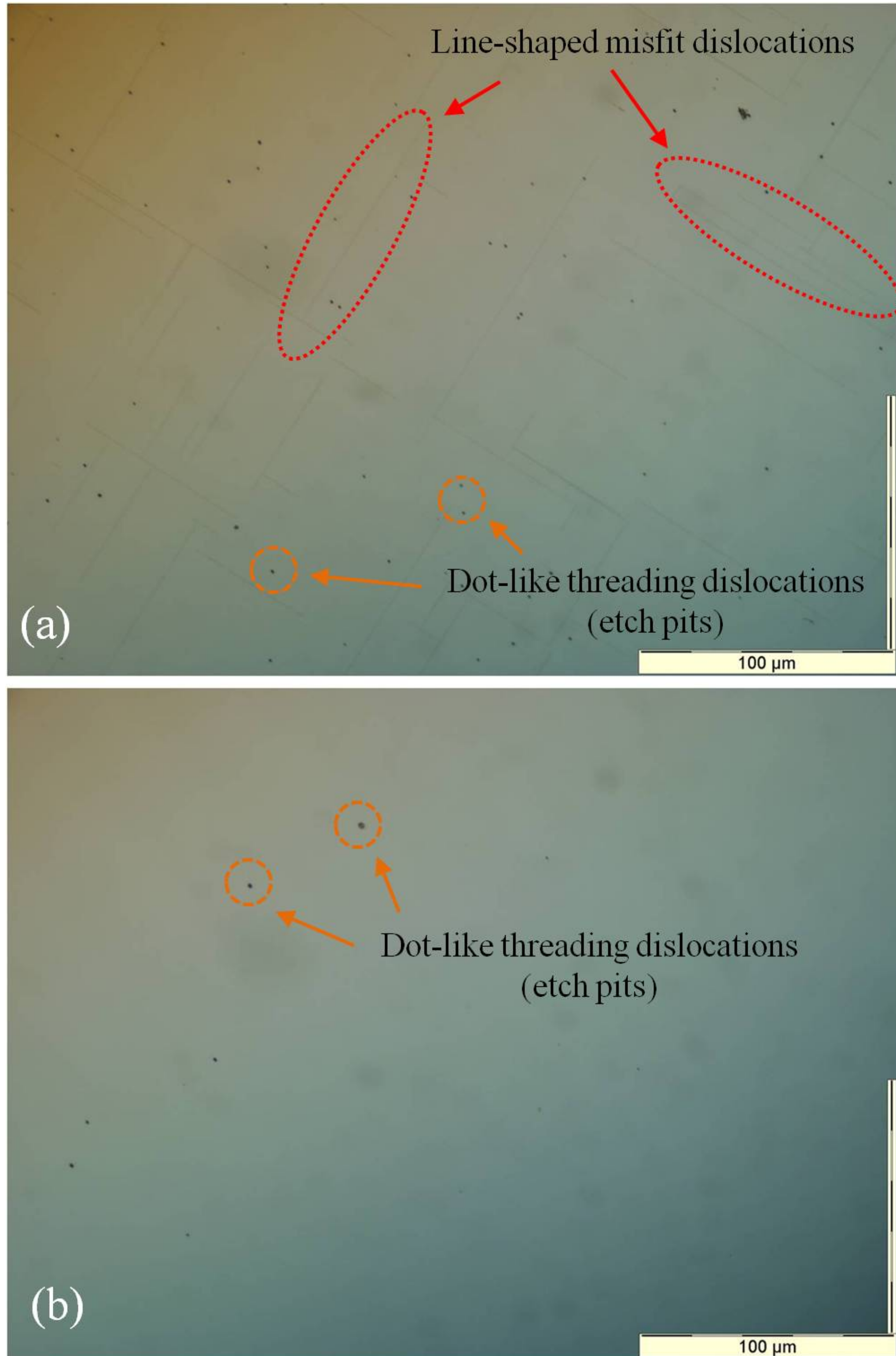

Figure 5.26: Images acquired by Normaski Microscopy after samples were dipped into modified Schimmel solutions.(a) Plenty of dot-like threading dislocations are distributed all over the sample whose $T_{Si,Cap}$ and $T_{Si,QW}$ were 575 °C and 700 °C respectively.(b) Much fewer etch pits are seen in the sample whose silicon layers were both grown at 625 °C.

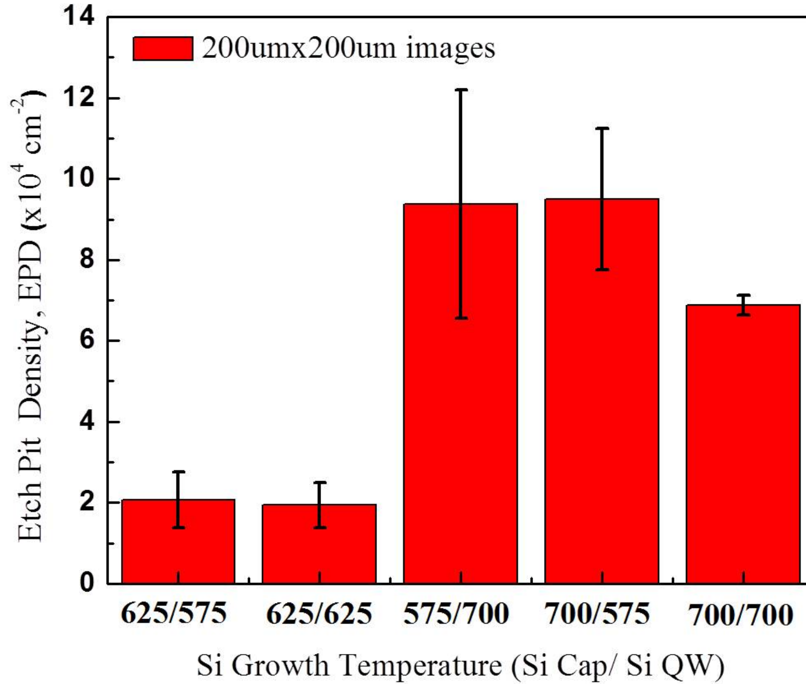

Figure 5.27: The EPD measured from images by Normaski microscopy versus silicon growth temperature.

transport property of an undoped 2DEG? To answer it, the highest mobility and the critical density for each sample were extracted again, and plotted versus its corresponding EPD in Fig. 5.28. Surprisingly, the highest mobility is basically independent of the EPD, even if some EPDs are almost 4 times higher than others. To seek possible explanations, we need to go back to review our SiGe relaxed graded buffers. As we mentioned in Ch. 2, thanks to the invention of SiGe graded buffer, the density of threading dislocation has been greatly improved. The state-of-the-art SiGe buffer layer with a CMP treatment has a much lower threading dislocations density (1-2×10^4 cm^{-2}) than old Si/SiGe heterostructures (~10^6 cm^{-2}). Based on this, the EPD observed in our samples were actually pretty low in terms of the order of magnitudes, regardless of growth temperature. Besides, the mobilities we have been talking about were measured in the regime where the electron density is 10^{10}-10^{12} cm^{-2}. Compared

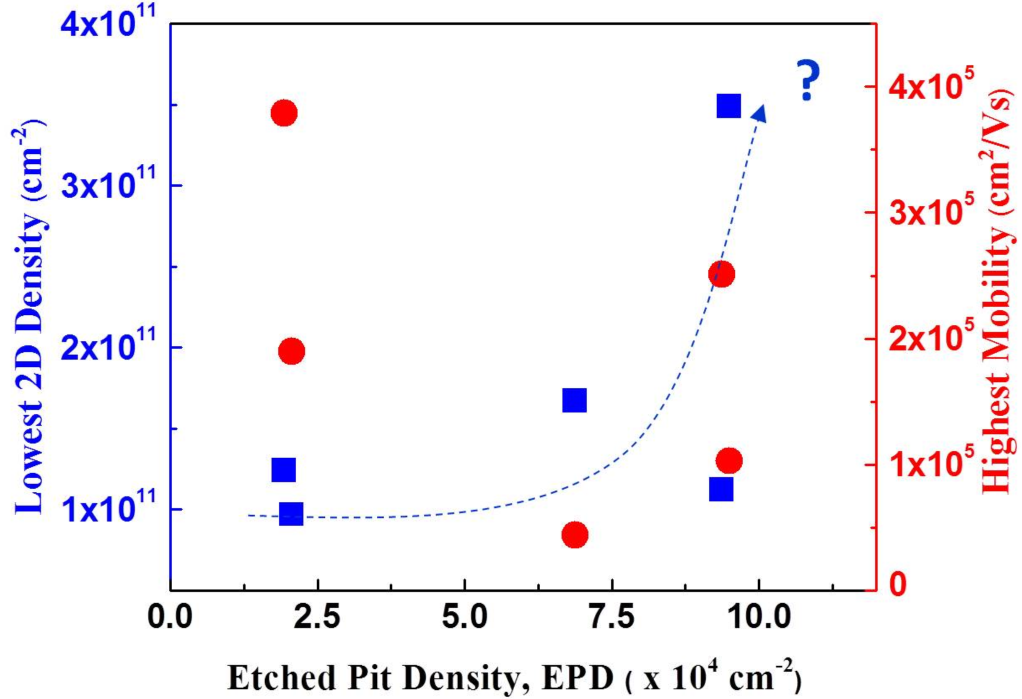

Figure 5.28: The highest mobility and lowest 2D density versus etch pit density from five different samples.

with the low number of EPD, mobile electrons with such high density shouldn′t be affected by threading dislocations. Nevertheless, a suspicious correlation between EPD and critical density was highlighted by a blue dotted curve: A higher critical density was observed in the sample with higher EPD. This subtle correlation could be the results of severe potential fluctuations induced by threading dislocations, where charged impurities tend to gather. However, insufficient data points do not allow us to believe this correlation is convincing yet. More experiments are necessary to support this argument.

5.8.3 Effects of Hall Bar Size

The density of threading dislocation could be too low to affect electron mobility significantly at the electron density in the range of 10^{10}-10^{12} cm^{-2}. However, the effect from misfit dislocations or other invisible imperfections in SiGe alloys has not been explored yet. A rough estimation from the image shown in Fig. 5.26a gives us an idea that each misfit dislocation are about 50-150 μm long, and distances between parallel misfits are around 20-100 μm. Imaging a case that a long line-shaped misfit dislocation is located coincidentally across the middle of a Hall bar device. This misfit dislocation may hinder electrons from moving in the channel, and thus severely deteriorate the transport property. To decrease the opportunity that a misfit cuts a Hall bar device, scaling down the size of a Hall bar device may be a good choice.

The geometry of a standard Hall bar used in this study was described in Fig. 5.5. The distance between two R_{xx} probes is 300 μm (Thus denoted as 300-μm Hall bar), and the width of the main conduction path is 100 μm (Fig. 5.29a). If compared with the dimension of misfit dislocations revealed by wet etching, it is inevitable that some misfit dislocations must overlap with our Hall bar device. In order to alleviate any scattering from the misfit dislocation (or other invisible crystal imperfection in SiGe alloys), much smaller Hall bar devices were also fabricated with a standard Hall bar device in the sample from the same growth run. The geometry of small Hall bar devices is illustrated in Fig. 5.29b. The distance between two R_{xx} probes is now reduced to 10 μm (denoted as 10-μm Hall bar), which is 30 times narrower than that in the standard one. The widths of the R_{xx} probes and main conduction path are narrowed 3.33 times and 10 times compared to before, down to 3 μm and 10 μm respectively. The total areas enclosed by two outer R_{xx} probes of the 10-μm Hall bar is only about 220 times smaller than that of the 300-μm Hall bar.

Since dislocations are randomly distributed all over the samples, more 10-μm Hall bar devices give us a higher chance to hit the sweet spot. The Hall measurement

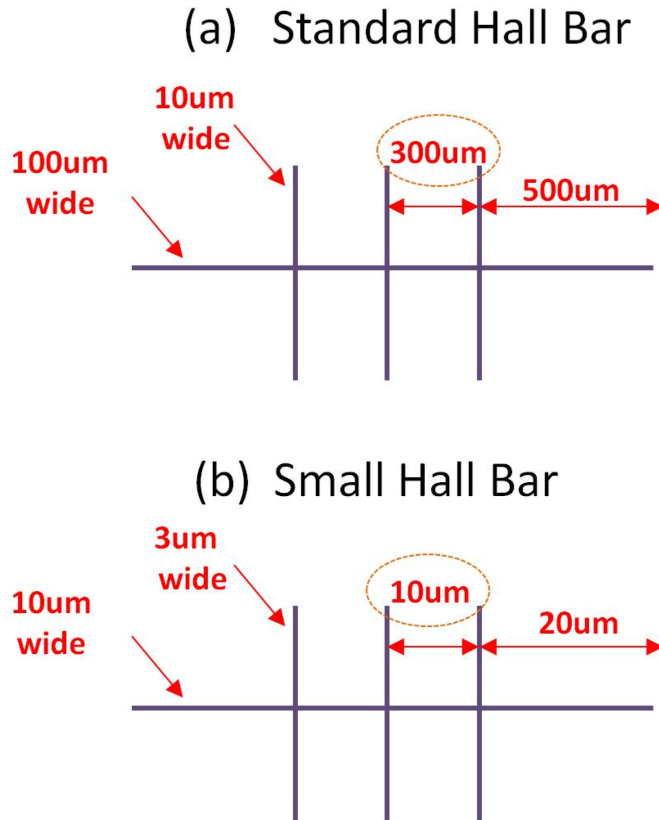

Figure 5.29: The geometries of (a) a standard Hall bar with a 300-μm spacing between R_{xx} probes (denoted as a 300-μm Hall bar) and (b) a small Hall bar with a 10-μm spacing between R_{xx} probes (denoted as a 10-μm Hall bar).

data from two small Hall bar devices (green and blue) were shown in Fig. 5.30 with the data from a standard Hall bar (red) for comparison. Unfortunately, we didn′t see any improvement in mobility curve from the miniaturization of Hall bar devices. Instead, the transport properties were degraded. The possible reason for the mobility degradation might be the non-uniformly distributed remote scattering sites at the interface. When the Hall bar device is large, the effect from the non-uniform potential fluctuation could be averaged out. However, once we shrink the size of the Hall bar, the small but dense gatherings of remote scattering sites which are coincidentally formed on top of the Hall bar may severely disturb the electron conduction through the device. Here we note that small Hall bar devices were made on several different

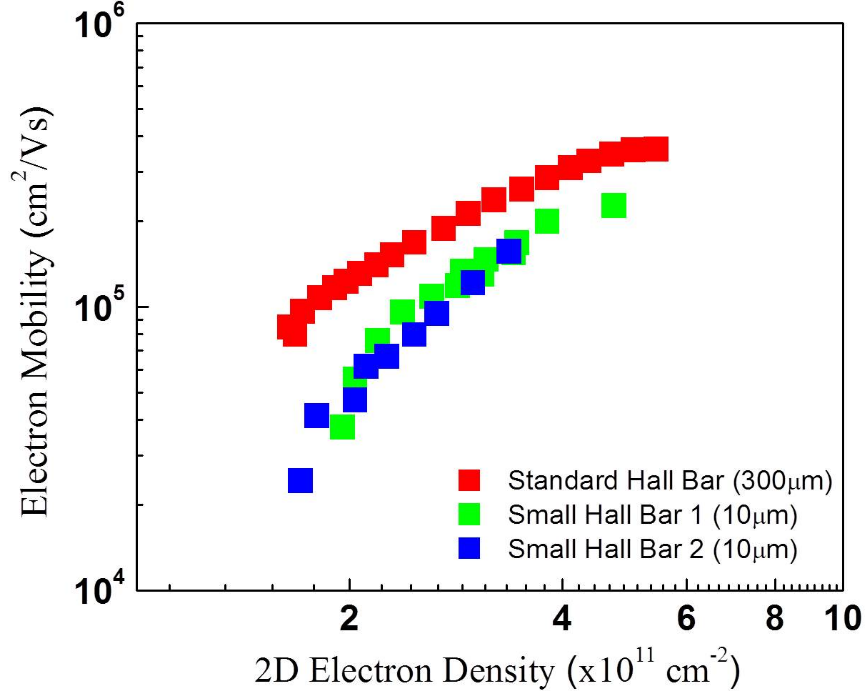

Figure 5.30: The comparison between mobility measured from a standard Hall bar and two small Hall bars fabricated in the sample from the same growth run.

samples repeatedly, but none of them showed the signs of improvement in transport properties.

5.9 Summary

Different kinds of scattering mechanisms possibly limiting electron mobility of an enhancement-mode strained silicon 2DEG have been individually discussed in this chapter. We first greatly alleviated background scattering by means of an significant reduction in background phosphorus concentration enabled by a brand new gas panel of our CVD system. A 1000 times lower phosphorus background concentration ($<10^{14}$ cm^{-3}) showed background scattering is no longer significant. Next, the remote scattering is considered as the dominant mobility-limiting factor for 2DEG samples

with relatively thin SiGe caps (<80 nm). An improvement in transport property of a 2DEG with a thicker SiGe cap has reassured its importance in both mobility and critical density. However, a saturation in mobility curve observed in samples with SiGe caps thicker than 80 nm implies other hidden mobility-limiting factors in our system. Furthermore, the relationship between minimum density, mobility and positive threshold voltages shifts (trapped electrons) is not clear. In addition, interface roughness scattering along with threading dislocation scattering have been systematically examined with a variation in growth temperatures of strained silicon layers. Unfortunately, none of them explained the mobility saturation. They didn′t show a direct and clear influence on either mobility or critical density. Other possible mobility-limiting factors could still exist in our 2DEG system and more experiments are necessary to discover them [92].

Chapter 6

Tunable Screening Effect in Undoped 2DEGs

6.1 Introduction

6.1.1 Motivation

Efforts to enhance electron mobility in an undoped 2DEG were discussed from various aspects in Ch. 5. We also mentioned the possible causes that limit the critical density, the 2D electron density at which the metal-insulator transition occurs. Among various mobility-limiting mechanisms, the scattering from remote charged impurities located at the oxide/silicon interface (remote scattering) is viewed as the most likely mechanism dominating in our system. The density of the remote charged impurities is also predicted to affect the critical 2D electron density in the MIT model mentioned in Sec. 5.4. Intuitive thinking concludes that a thick SiGe cap layer to separate the 2DEG away from the interface can lead to high electron mobility (μ) and low critical 2D electron density (n_{2D}). Many experimental results also strongly agree this argument [68, 76].

However, to pattern an undoped 2DEG into a QD, a thin SiGe cap layer is preferred to enable patterned top gates to precisely define the lateral extension of the 2DEG, even though a thin cap degrades the 2DEG transport properties. In this chapter, we present an improvement in the 2DEG properties (higher mobility and lower critical n_{2D}) in samples with thin SiGe cap layers (<40 nm) by introducing a tunable shielding electron layer near the surface. We believe that, at a critical electrical field, the tunneling of electrons from the buried silicon QW to the surface triggers the formation of a barely mobile electron layer near the silicon surface. This surface electron layer effectively screens the remote charge scattering sites, and thus dramatically improves both mobility and critical n_{2D}. As part of this work, we introduce the concept of equilibrium versus non-equilibrium in 2DEG densities as well. This work is summarized in [93].

6.1.2 Device Fabrication

The enhancement-mode strained silicon 2DEGs have a similar structure and process flow to that described in Ch. 5. The undoped Si/SiGe heterostructures in this study were grown by rapid thermal chemical vapor deposition (RTCVD) on top of relaxed $Si_{0.72}Ge_{0.28}$ virtual substrates. After growing another $Si_{0.72}Ge_{0.28}$ relaxed buffer layer (90 to 165 nm) on the top of this starting virtual substrate, an 11-nm strained silicon quantum well (denoted as the buried QW in this chapter for clarity) was then grown to hold the 2DEG. Subsequently, a thin undoped $Si_{0.72}Ge_{0.28}$ cap layer (14, 20, or 40 nm) was grown, followed by a 4-nm strained silicon cap layer (denoted as the surface QW) growth (5-nm for the 14-nm cap sample). The actual layer thicknesses may differ by $\pm$ 20%. To contact the buried 2DEG, phosphorus was first implanted in contact regions, followed by annealing at 600 °C. A 90-nm aluminum oxide layer was then deposited by atomic layer deposition as a gate insulator. A chrome/gold stack

was finally evaporated on samples to form both a Hall-bar-shaped gate and metal contacts on the implanted regions.

6.2 Four-Stage Behavior of 2D Electron Density

6.2.1 Observation of a Density Collapse

The Hall measurements with the same setup as before were performed at liquid helium temperature (4.2 K). Four clear stages of the Hall electron density ($n_{2D,Hall}$) were observed in all samples as the gate voltage was ramped up. Fig. 6.1 shows data for the 14-nm SiGe cap sample as a characteristic example. When the gate voltage is above zero but below a threshold voltage (V_T), which is ~2.9 V, the n_{2D} which is ideally induced in the buried QW is low, leading to insulating behavior (referred to as stage I) due to disorder and potential fluctuations, primarily from remote charged impurities at the oxide/silicon interface [60, 61, 77, 94]. Once the gate voltage supports an electron density above the critical density for the metal-insulator transition (MIT) [95], 3.5×10^{11} cm^{-2} in this sample, electrons start to flow from the contacts into the buried QW to form a 2DEG (stage II). The experimental capacitance extracted from the linear dependence of the Hall electron density on gate voltages from 2.9 to 3.5 V in stage II is close to (~90%) the expected value based on a parallel-plate capacitor model between the 2DEG and the gate. (By $n_{2D,Hall}$ and μ_{Hall} in this chapter, we mean those extracted from the measurements assuming a single transport layer, in this case the buried silicon quantum well.)

With further increase in the positive gate bias, a sharp collapse of $n_{2D,Hall}$ was clearly observed in all samples when $n_{2D,Hall}$ reached ~6.0×10^{11} cm^{-2}, dropping to 2.2×10^{11} cm^{-2}, much lower than the density originally required to initiate conduction. This new range is referred as stage III. With a 3-4 V further increase of gate voltage, $n_{2D,Hall}$ then increased only marginally ($<0.3\times10^{11}$ cm^{-2}), while a simple

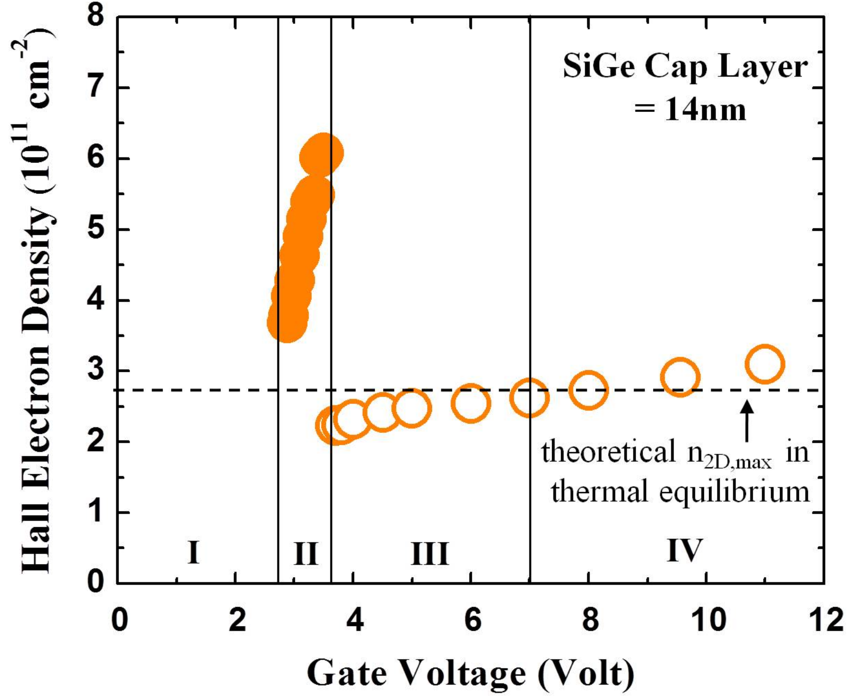

Figure 6.1: The four-stage behavior in Hall electron density observed in all three samples (Data here are from the sample with a 14-nm SiGe cap layer). The dashed line shows the theoretical maximum n_{2D} from the self-consistent Schrodinger-Poisson (SCSP) simulation.

$C{\cdot}\Delta V_G$ calculation would predict an increase of $n_{2D,Hall}$ of ~10^{12} cm^{-2}. In addition to the reduction in minimum n_{2D} in the sharp transition from stage II to stage III, the electron mobility is also dramatically enhanced (Fig. 6.6). Explaining these effects is the focus of this chapter; we hypothesize the effects are due to the formation of a tunable shielding electron layer at the semiconductor surface which screens the buried 2DEG from the scattering from remote charged impurities at the oxide/silicon interface. Here we note that all data from Hall measurements shown in Ch. 5 are in stage II before the density collapses for clarification.

6.2.2 Non-Equilibrium in Stage II

Since the buried QW (11 nm) is thicker than the surface QW (4-5 nm) in our structures, at flatband the ground state (E_0) of surface silicon lies higher than the one in the buried QW. Therefore, as the gate voltage increases, E_0 of the buried QW drops to the Fermi level (E_F), defined by the contacts, before that for the surface layer, leading to the population of a buried 2DEG (Fig. 6.2a). As the gate voltage increases to induce higher density of mobile electrons in the buried QW, eventually E_0 of the surface QW will fall below E_F, so that electrons in the surface QW would be expected. With this assumption of thermal equilibrium with the contacts (both densities represented by a single Fermi level), once the surface electron layer forms (blue solid line in Fig. 6.3), a further increase in the gate voltage will lead to an increase only in the surface electron density ($n_{\text{surface, Eq}}$) and the electron density in the buried QW ($n_{\text{buried, Eq}}$) will remain fixed to first order (red solid line), because surface electrons will screen out the electrical field from the gate. However, the close proximity of many scattering charges at the oxide/silicon interface leads to a high critical density for the MIT of the surface layer. Thus when $n_{\text{surface, Eq}}$ would be expected to be at a low value, it is impossible for electrons to flow laterally from the contacts into the surface QW. Furthermore, the low vertical electric field prevents electrons from tunneling from the buried QW to the surface layer. Thus a surface layer cannot form, and the surface layer is not in thermal equilibrium with the contacts, with its ground state E_0 substantially below the contact Fermi level (Fig. 6.2b) [48]. Therefore, as the gate voltage is raised, more electrons continue to accumulate in the buried QW, with the system continuing to exhibit stage II behavior (dotted lines in Fig. 6.3) in a non-equilibrium condition. The situation is in some sense analogous to deep depletion in a MOS capacitor. In that case, also an inversion layer should be expected based on equilibrium principles, but there is no mechanism to create one.

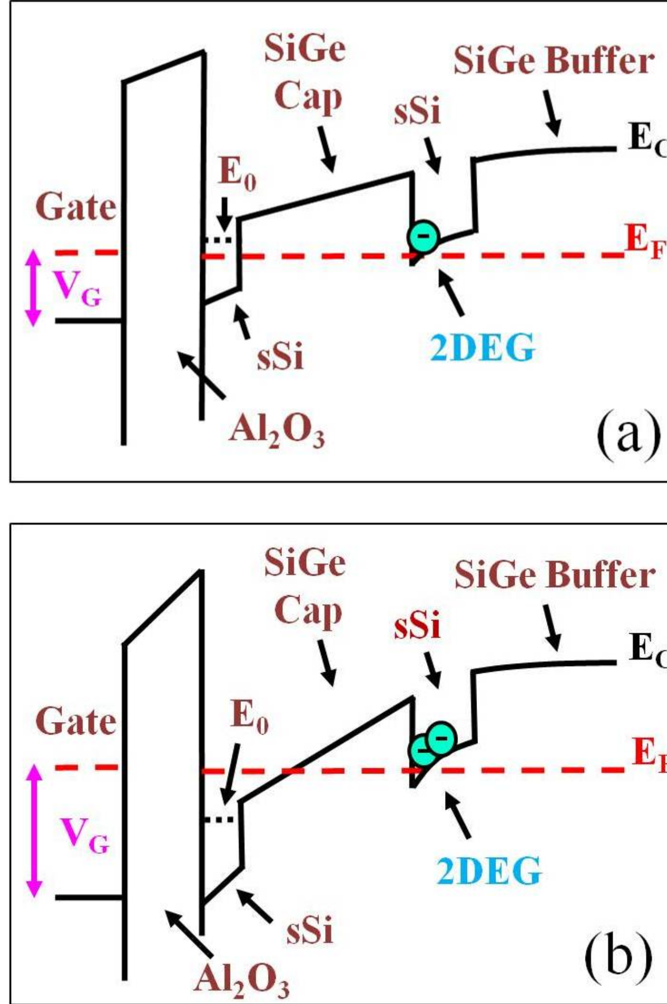

Figure 6.2: (a)With a small gate bias, electrons accumulate in the buried QW first. (b) Even with a large gate bias, no electrons populate the surface QW due to a high critical density for metal-insulator transition (MIT) in that layer.

6.2.3 Switching from Stage II to Stage III

We propose the sharp collapse in $n_{2D,Hall}$ with a further increase in gate voltage is triggered by electron tunneling, which initiates a positive feedback process (Fig. 6.4a and b). At an electron density of 6×10^{11} cm^{-2} in all samples, corresponding to a critical electric field of 10^5 V/cm if spurious charges are ignored, electrons begin to significantly tunnel through the thin SiGe cap layer into the surface. The surface density then reaches a point where some slow conduction laterally from the contacts

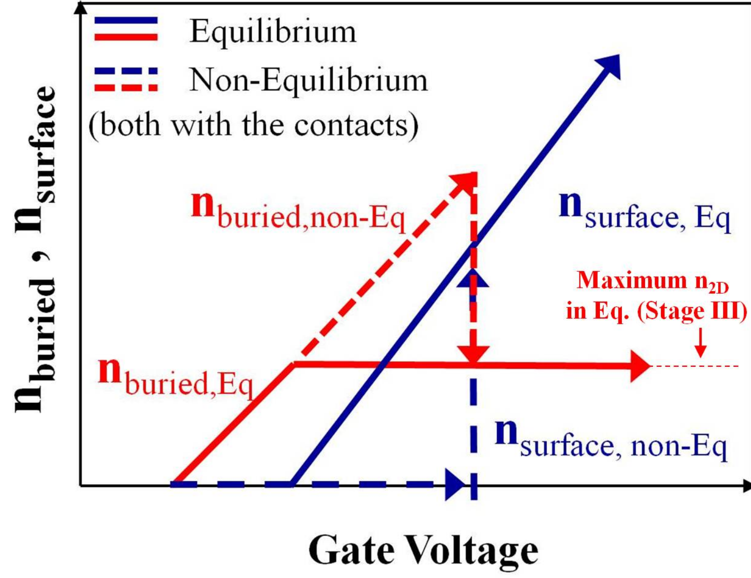

Figure 6.3: The comparison of buried electron density (n_{buried}, red) and surface electron density ($n_{surface}$, blue) with increasing gate voltages in both thermal equilibrium with the contacts between two 2DEGs and with the surface channel not in equilibrium. A sudden collapse in n_{buried} as the gate voltage increases and the corresponding increase in $n_{surface}$ bring the system back to thermal equilibrium.

into the surface layer occurs (Fig. 6.4c). This initial increase in density feeds back to cause a further increase in conductivity and thus more lateral flow, leading to the formation of a surface electron layer at its expected equilibrium density (Fig. 6.4d). As the surface layer forms at a fixed gate voltage, electrons must also flow out of the buried QW to obey Gausss law (Fig. 6.5). The simultaneous increase in $n_{surface,non\text{-}Eq}$ (blue dashed line in Fig. 6.3) and decrease in $n_{buried,non\text{-}Eq}$ (red dashed line in Fig. 6.3) brings the whole system back to thermal equilibrium (stage III).

Note that the time scale for the density collapse, namely the time scale for electrons to flow into the surface layer, could be on the order of five minutes - this is the approximate time between Hall measurements at each gate voltage. Beyond this point, in equilibrium, with more gate voltage we expect an increase mostly in the surface density. Furthermore, if the surface mobility (and thus conductivity) were several orders of magnitude below that of the buried layer, which we believe to initially

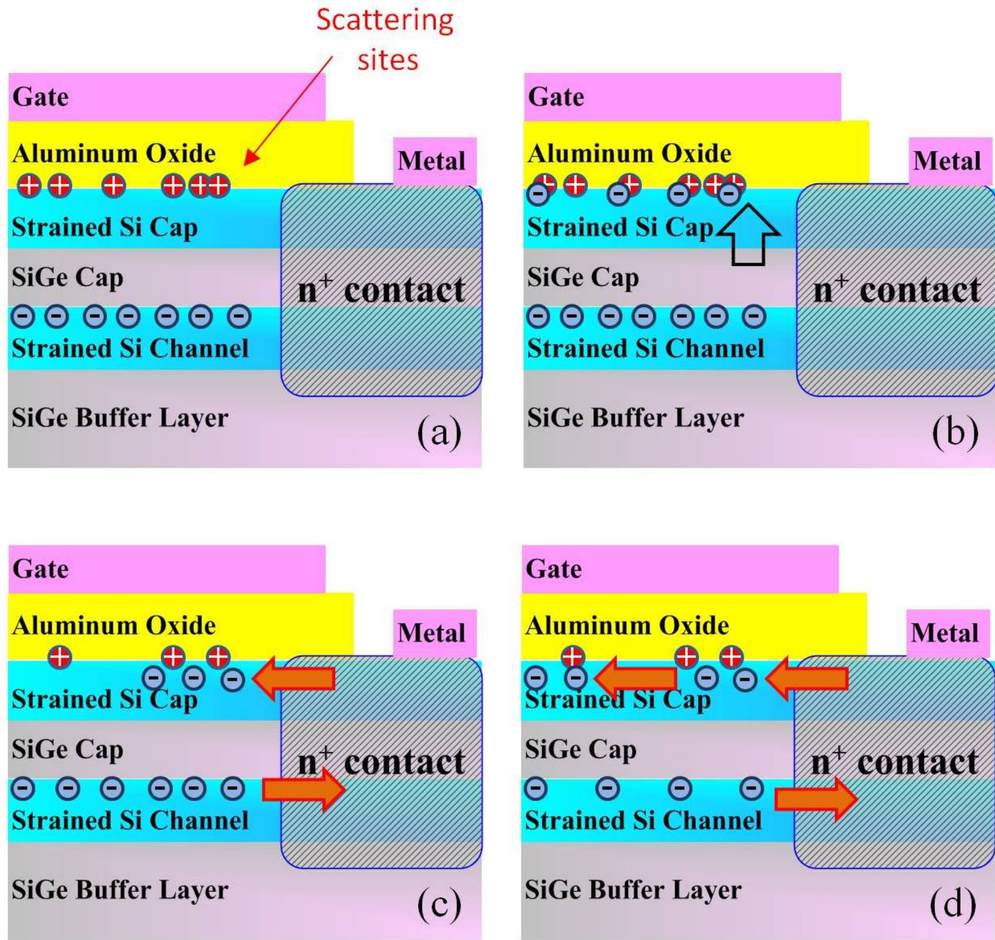

Figure 6.4: (a) no electrons are induced in the surface due to a high critical density of MIT for the surface QW. (b) At a higher gate voltage, electron tunneling from the buried QW towards the surface raises the density above the metal insulator transition point, leading to a current flowing from the contacts into the surface layer (c). (d) By Gauss′s law, the buried electron density must be reduced as the surface density increases at a fixed gate voltage. The system is then switched from non-equilibrium to thermal equilibrium.

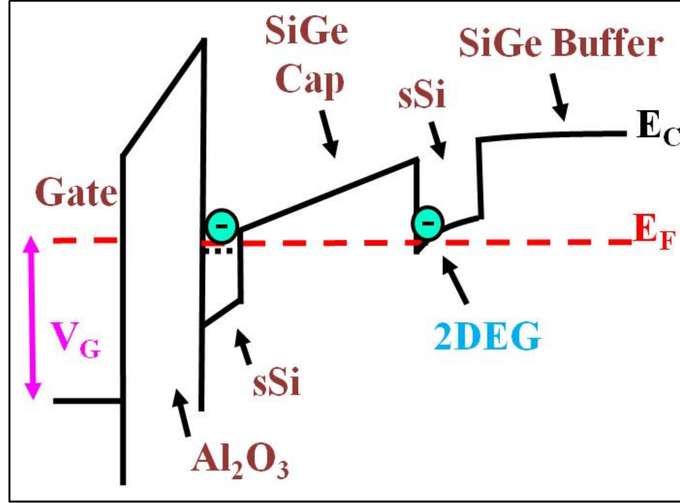

Figure 6.5: Electrons exist at both the surface and the buried QW, with the same Fermi level in both layers. Now the system is in thermal equilibrium.

be the case, a single-layer interpretation of the Hall measurements ($n_{2D,Hall}$ and μ_{Hall}) would continue to represent the properties of the buried layer.

6.2.4 Support by a Simulation

To build confidence in our model, a self-consistent Schrodinger-Poisson (SCSP) simulation [96] was utilized to calculate the theoretical maximum n_{2D} in the buried quantum well in thermal equilibrium, which is the constant value that the red solid line in Fig. 6.3 represents at high gate voltage. For samples with 14-nm, 20-nm and 40-nm SiGe caps, these values are 2.7×10^{11} cm^{-2}, 2.9×10^{11} cm^{-2}, and 1.9×10^{11} cm^{-2} respectively. The $n_{2D,Hall}$ values (representing the buried layer) measured near the end of stage II (~6.0×10^{11} cm^{-2}) were much higher than these values, implying the surface layer was indeed not in equilibrium at the end of stage II when the collapse occurs. Furthermore, note the experimental values just after the stage II/stage III (equilibrium/non-equilibrium) transition were 2.5×10^{11} cm^{-2}, 2.4×10^{11} cm^{-2} and 1.7×10^{11} cm^{-2} for these three samples, respectively, all in reasonable agreement with the predictions (Fig. 6.6). Both results support our model that the stage II/III col-

lapse is a switch of the surface layer from non-equilibrium to equilibrium. More details about SCSP simulation in undoped 2DEGs will be discussed in Sec. 7.2.

6.3 Tunable Screening Effect in Thin-Cap 2DEGs

6.3.1 Improved Transport Property

We now discuss the transport properties, and show the dependence of the Hall mobility on the Hall electron density (Fig. 6.6). For each sample two sets of points are shown: closed symbols before the transition and open symbols after it. With no surface layer in stage II, the mobility of each sample increases with density due to the usual self-screening. Because the mobility at a given density increased (and the minimum density decreased) as the separation between the semiconductor/insulator interface and the buried 2DEG increased, it seems clear that the main scattering sites are at the surface (or inside the insulator) [67]. When the system switches back to thermal equilibrium, the new intermediate electron layer near the surface separates the buried 2DEG and the scattering sites, resulting in a strong screening effect on both the minimum n_{2D} and electron mobility of the buried layer. In all samples, after the transition, the samples now conduct well at densities only 60-70% of their previous minimum densities (Fig. 6.7a). Note the small range of Hall electron densities in stage III despite an increase of gate voltage of several volts; this is because new charges go mostly into the surface layer and not the buried layer as expected from Fig. 6.3.

Beyond the density reduction, the screening effect enhances the electron mobility of the buried layer as well (Fig. 6.6). In stage II, the highest electron mobility obtained from samples with 14-nm, 20-nm and 40-nm SiGe caps are 47,000 cm^2/Vs, 153,000 cm^2/Vs and 381,000 cm^2/Vs at high densities (~6.0×10^{11} cm^{-2}), respectively, with the 20-nm cap sample requiring a density of ~5.0×10^{11} cm^{-2} to reach a mobility of

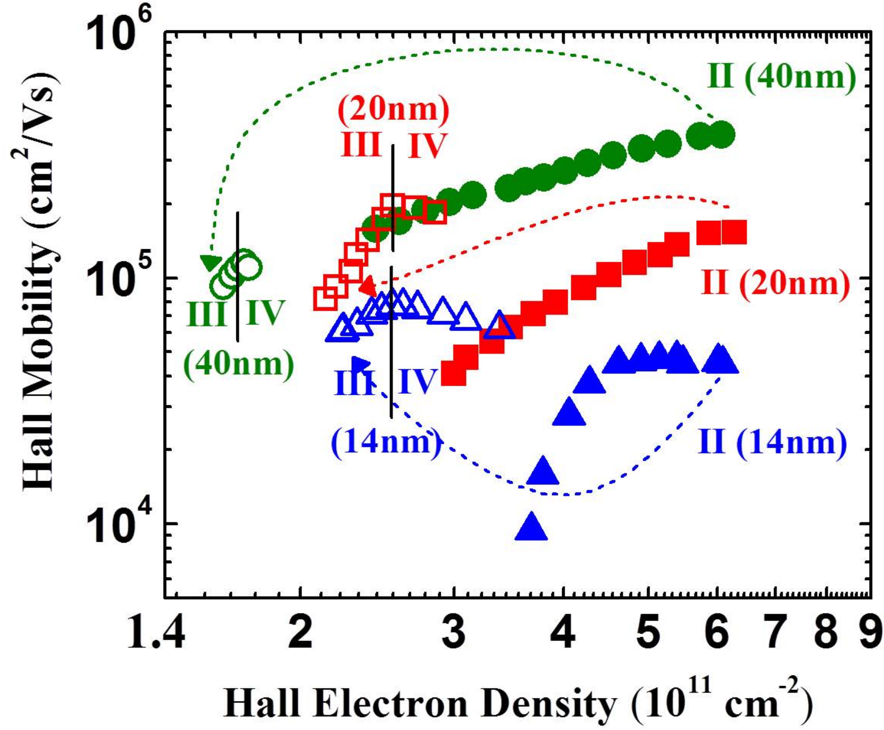

Figure 6.6: The dependence of Hall mobility on Hall electron density measured at 4.2 K for all three samples with different stages labeled. The gate voltage steps for data points at stage II and stage III/IV are 0.03-0.15 V/ 0.1-2 V, respectively for all three samples. The measurement sequence is indicated by dashed lines (from stage II to stage III).

100,000 cm^2/Vs. After the transition both the 14-nm and 20-nm cap samples achieve a mobility at or near 100,000 cm^2/Vs at a density of only ~2.3×10^{11} cm^{-2}, and the 40-nm cap sample achieves this benchmark at a density of only ~1.6×10^{11} cm^{-2}. The 20-nm cap sample reaches 196,000 cm^2/Vs at only ~2.6×10^{11} cm^{-2}. These densities are well below the metal-insulator transition level for each of the three samples before the transition.

6.3.2 Effect of Surface Electron Density

To emphasize the importance of the surface electron layer on the mobility enhancement in stage III, the relation between $n_{surface}$ and Hall mobility for all three samples